UC Merced
UC Merced Electronic Theses and Dissertations

Title
Tribological Phenomena at the Atomic Scale Interface: 2D materials and beyond

Permalink
https://escholarship.org/uc/item/9tn9h15w

Author
Ye, Zhijiang

Publication Date
2016

Copyright Information
This work is made available under the terms of a Creative Commons Attribution-NonCommercial-ShareAlike License, availalbe at
https://creativecommons.org/licenses/by-nc-sa/4.0/

Peer reviewed|Thesis/dissertation

eScholarship.org
Powered by the California Digital Library
University of California

UNIVERSITY OF CALIFORNIA, MERCED

TRIBOLOGICAL PHENOMENA AT THE ATOMIC SCALE INTERFACE: 2D MATERIALS AND BEYOND

by

Zhijiang Ye

A thesis submitted in partial satisfaction of the
requirements for the degree of
Doctor of Philosophy

in

Mechanical Engineering

Committee in charge:
Professor Ashlie Martini, Advisor
Professor Jian-Qiao Sun
Professor Min Hwan Lee
Professor Erin R. Johnson

©2016 Zhijiang Ye

©2016 Zhijiang Ye
All rights are reserved.

The thesis of Zhijiang Ye is approved:

Ashlie Martini, Advisor	Date
Jian-Qiao Sun	Date
Min Hwan Lee	Date
Erin R. Johnson	Date

University of California, Merced

©2016 Zhijiang Ye

To my wife and son.

CURRICULUM VITAE

EDUCATION

- B.S. in Aerospace Power Engineering, Beijing University of Aeronautics and Astronautics (Beijing, China), 2008.
- M.S. in Mechanical Engineering, Beijing University of Aeronautics and Astronautics (Minneapolis, MN, U.S.), 2011.

HONORS AND AWARDS

- UC Merced 2015-2016 Graduate Deans Dissertation Fellowship
- 2015 Chinese Government Award for Outstanding Self-Financed Student Abroad
- 2015 Bobcat Fellowship Award, University of California, Merced
- UC Merced 2014-2015 School of Engineering Dean's Travel Award
- 2014 STLE Northern California Research Scholarship
- 2013 Mechanical Engineering Graduate Fellowship Award, University of California, Merced
- Student Poster Award, 2014 Society of Tribologists and Lubrication Engineers Annual Meeting and Exhibition
- Young Tribologist Award, Society of Tribologists and Lubrication Engineers, 2013
- 3rd place in art zone contest of 2013 AVS 60th International Symposium and Exhibition
- 2013 MEAM Travel Fellowship Award, University of California, Merced
- Platinum Award, 2012 Society of Tribologists and Lubrication Engineers 68th Annual Meeting and Exhibition

- Spring 2012 Graduate Division General Fellowship, University of California, Merced
- 1st place in poster competition, 2011 ASME/STLE International Joint Tribology Conference

PUBLICATIONS

1. **Zhijiang Ye**, Philip Egberts, Ganghee Han, A. T. Charlie Johnson, Robert W. Carpick, and Ashlie Martini, Environmental effect of load dependent friction hysteresis on graphene, *ACS Nano*, Under review (2016).
2. **Zhijiang Ye**, Ashlie Martini, Patricia A. Thiel, Heather H. Lovelady, Keith McLaughlin, and David A. Rabson, Atomistic simulation of frictional anisotropy on quasicrystal approximant surfaces, *Physical Review B*, Under review (2016)
3. Xin-Z. Liu*, **Zhijiang Ye***, Philip Egberts, Yalin Dong, Robert W. Carpick, and Ashlie Martini, Dynamics of atomic stick-slip friction examined with atomic force microscopy and atomistic simulations at overlapping speeds, *Physical Review Letters*, **114**, 146102 (2015) ***Co-first anthor**
4. **Zhijiang Ye** and Ashlie Martini, Atomic Friction at Exposed and Buried Graphite Step Edges: Experiments and Simulations, *Applied Physics Letters*, **106**, 231603 (2015)
5. **Zhijiang Ye**, Otero-de-la-Roza, Erin R. Johnson and Ashlie Martini, Oscillatory Motion in Layered Materials: Graphene, Boron Nitride, and Molybdenum Disulfide, *Nanotechnology*, **26**, 165701 (2015)
6. Heather L. Adams, Michael Garvey, Uma Ramasamy, **Zhijiang Ye**, Ashlie Martini, Wilfred T Tysoe, Shear-induced mechanochemistry: pushing molecules around, The *Journal of Physical Chemistry C*, **119**, 7115-7123 (2015)
7. **Zhijiang Ye** and Ashlie Martini, Atomistic simulation of the load dependence of nanoscale friction on suspended and supported graphene, *Langmuir*, **30**, 14707 (2014)
8. **Zhijiang Ye**, Alberto Otero-de-la-Roza, Erin R. Johnson and Ashlie Martini, The role of roughness-induced damping in the oscillatory motion of bilayer graphene, *Nanotechnology*, **25**, 425703 (2014)
9. Jairo A. Diaz, **Zhijiang Ye**, Xiawa Wu, Ashlie Martini, Jeffrey P. Youngblood and Robert J. Moon, Thermal Conductivity of Self-organized and Shear-oriented Cellulose Nanocrystal Films, *Biomacromolecules*, **15**, 4096-4101 (2014)

10. **Zhijiang Ye**, Hyeong Moon, Min Hwan Lee and Ashlie Martini, Size and load dependence of nanoscale electric contact resistance, *Tribology International*, **71**, 109-113 (2014)
11. Xiaoli Hu, Chris Tourek, **Zhijiang Ye**, Sriram Sundararajan and Ashlie Martini, Structural and Chemical Evolution of the Near-Apex Region of an Atomic Force Microscope Tip Subject to Sliding, *Tribology Letters*, **53**, 181-187 (2014)
12. **Zhijiang Ye**, Alberto Otero-de-la-Roza, Erin R. Johnson and Ashlie Martini, Effect of tip shape on atomic-friction at graphite step edges, *Applied Physics Letters*, **103**, 081601 (2013)
13. Philip Egberts, **Zhijiang Ye**, Xin Liu, Yalin Dong, Ashlie Martini, and Robert W. Carpick, Environmental dependence of atomic-scale friction at graphite surface steps, *Physical Review B*, **88**, 035409 (2013)
14. **Zhijiang Ye**, Chun Tang, Yalin Dong and Ashlie martini, Variation of Friction with Number of Graphene Layers, *Tribology and Lubrication Technology*, **69**, 19-21, (2013)
15. Mathieu Luisier, Timothy Boykin, textbfZhijiang Ye, Ashlie Martini, Gerhard Klimeck, Neerav Kharche, Xueping Jiang and Saroj Nayak, Investigation of ripple-limited low-field mobility in large-scale graphene nanoribbons, *Applied Physics Letters*, 102, 253506 (2013)
16. **Zhijiang Ye**, Chun Tang, Yalin Dong and Ashlie Martini, Role of Wrinkle Height in Friction Variation with Number of Graphene Layers, *Journal of Applied Physics*, **112**, 116102 (2012)
17. Yalin Dong, Xin Z. Liu, Philip Egberts, **Zhijiang Ye**, Robert W. Carpick and Ashlie Martini, Correlation Between Probe Shape and Atomic Friction Peaks at Graphite Step Edges, *Tribology letters*, **50**, 49-57 (2012)
18. Dongjin Lee*, **Zhijiang Ye***, S. A. Campbell and T. Cui, Suspended and Highly Aligned Carbon Nanotube Thin Film Structures Using Microfluidic Template, *Sensor and Actuators A*, **188**, 434-441 (2012) ***Co-first author**
19. **Zhijiang Ye**, D. Lee, S. A. Campbell and T. Cui, Thermally Enhanced single-walled carbon nanotube microfluidic alignment, *Microelectronic Engineering*, **88**, 2919-2923 (2011)
20. Min-Woo Jang, Chia-Ling Chen, Walter E Partlo, Shruti R Patil, Dongjin Lee, **Zhijiang Ye**, David Lilja, T. A. Taton, Tianhong Cui and Stephen A. Campbell, A Pure Single-Walled Carbon Nanotube Thin Film Based 3-Terminal MEMS Switch, *Applied Physics Letters* **98**, 073502 (2011)

TABLE OF CONTENTS

CURRICULUM VITAE . . . . **ii**
LIST OF FIGURES . . . . **ix**
LIST OF TABLES . . . . **xix**
ABSTRACT . . . . **xx**

Chapter

1 INTRODUCTION **1**

1.1 2D Materials and Beyond 1
1.2 Tribological Properties 4

1.2.1 Background and Motivation 4
1.2.2 Atomic Friction 4

1.3 Thermal and Electrical Properties 7

1.3.1 Background and Motivation 7
1.3.2 Thermal and Electrical Properties at The Nanoscale 7

1.4 Molecular Dynamics Simulation 9

1.4.1 Overview of Molecular Dynamics Simulation 9
1.4.2 Applications of Molecular Dynamics Simulation 9

1.5 Thesis Outline 9

2 NANOTRIBOLOGY ON “PERFECT” SURFACES **10**

2.1 Effect of Graphene Layers on Atomic Friction 10

2.1.1 Introduction 10

2.1.2 Methods 11
2.1.3 Results and Discussion 12
2.1.4 Conclusion 15

2.2 Negative Friction Coefficient on Suspended Graphene 17

2.2.1 Introduction 17
2.2.2 Methods 17
2.2.3 Results and Discussion 19
2.2.4 Conclusion 23

2.3 Oscillatory Motion of Bilayer Graphene 26

2.3.1 Introduction 26
2.3.2 Methods 26
2.3.3 Results and Discussion 27
2.3.4 Conclusion 32

2.4 Oscillatory Motion in 2D Materials 35

2.4.1 Introduction 35
2.4.2 Methods 35
2.4.3 Results and Discussion 37
2.4.4 Conclusion 46

2.5 Frictional Anisotropy on Quasicrystal Approximant Surfaces 47

2.5.1 Introduction 47
2.5.2 Methods 48
2.5.3 Results 49
2.5.4 Discussion 56

2.6 Load Dependent Friction Hysteresis on Graphene 60

2.6.1 Introduction 60
2.6.2 Methods 61
2.6.3 Results 62
2.6.4 Discussion 66
2.6.5 Conclusion 72

3 NANOTRIBOLOGY ON IMPERFECT SURFACES 74

3.1 Effect of Tip Shape on Atomic Friction at Graphene Step Edge . . . 74

3.1.1 Introduction 74
3.1.2 Methods 75
3.1.3 Results and Discussion 75
3.1.4 Conclusion 79

3.2 Atomic Friction at Exposed and Buried Graphene Step Edges 80

3.2.1 Introduction 80
3.2.2 Methods 80
3.2.3 Results and Discussion 82
3.2.4 Conclusion 89

4 NANOTRIBOLOGY UNDER EXTREME CONDITIONS 90

4.1 Effect of Environment on Atomic Friction at Graphene Step Edge . . 90

4.1.1 Introduction 90
4.1.2 Methods 91
4.1.3 Results and Discussion 92
4.1.4 Conclusion 94

4.2 Speed Dependence of Atomic Friction on Gold Substrate 96

4.2.1 Introduction 96
4.2.2 Methods 97
4.2.3 Results and Discussion 97
4.2.4 Conclusion 104

4.3 Temperature Dependence of Atomic Friction on 2D Materials 105

4.3.1 Introduction 105
4.3.2 Methods 105
4.3.3 Results and Discussion 107
4.3.4 Conclusion 108

5 ELECTRICAL AND THERMAL TRANSPORT AT NANOSCALE INTERFACE 110

5.1 Nanoscale Electric Contact Between an AFM Tip and Graphene Substrate 110

5.1.1 Introduction 110
5.1.2 Methods 111
5.1.3 Results and Discussion 112
5.1.4 Conclusion 117

5.2 Thermal Conductivity of Cellulose Crystal at Nanoscale Interface . . 118

5.2.1 Introduction 118
5.2.2 Methods 119
5.2.3 Results and Discussion 120
5.2.4 Conclusion 122

6 FUTURE WORK AND SUMMARY 124

6.1 Future Work 124

6.1.1 Effect of Step Edges on Tip-Substrate Contact Under Electrical Field 124
6.1.2 Size and Layer Dependence of Thermal Conductivity on Graphene 125
6.1.3 Temperature Dependence of Atomic Friction with Closely Matched Experiments and Simulations 126

6.2 Concluding Remarks 127

BIBLIOGRAPHY 128

LIST OF FIGURES

1.1 Classification of materials; figure from [1]. 2

1.2 (a) MD image of graphene, (b) AFM lateral force image of graphene from Dr. R.W. Carpick's group, (c) MD image of $\alpha - BN$, (d) TEM image of graphene from [2], (e) MD image of MoS_2, (f) TEM image of graphene from [2] 3

1.3 AFM measurement of (a) lateral force map and (b) stick-slip friction on graphite ; data from Dr. R.W Carpick's group. 6

2.1 Snapshot of the model system where a hemispherical diamond tip is connected to a harmonic spring which pulls it over graphene layers. 11

2.2 Effect of number of graphene layers on friction for 42 nm long sheets. 12

2.3 The effect of graphene length on frictional layer-dependence. 13

2.4 Local profiles of the graphene layers during the scanning process. . 14

2.5 Height of the wrinkle in front of the tip varying with number of graphene sheets and their length. 15

2.6 Binding energy of multi-layer graphene decrease monotonically with sheet length. 16

2.7 (a) Snapshot of an MD simulation of a hemispherical diamond tip sliding on graphene. Close up views of the local deformation on (b) suspended and (c) supported graphene. 18

2.8 Load dependence of (a) friction, (b) contact area, and (c) wrinkle height on supported and suspended graphene. These cases correspond to simulations with a 2.5 nm tip radius and 10×10 nm graphene. 20

2.9 Cross-section images of (a) supported and (b) suspended graphene during sliding at different loads. The sliding direction is left to right. Simulations performed with a 2.5 nm tip radius and 10×10 nm graphene 22

2.10 Load dependence of friction (a) on suspended graphene with Tersoff and AIREBO potentials (2.5 nm radius tip, 100×100 nm graphene), purple triangles represent experimentally-measured friction between an ultrananocrystalline diamond (UNCD) tip and suspended graphene [3], (b) on supported and suspended graphene with side lengths 10 and 100 nm (2.5 nm tip), (c) on suspended graphene with a 2.5 and 30 nm radius tip (100×100 nm graphene), and (d) on suspended graphene with original and 25% weaker interaction strength (30 nm radius tip, 100×100 nm graphene). 24

2.11 Variation in the potential energy with offset position, illustrating the V-shaped profile that drives the system towards its low-energy overlapped configuration as well as local variation due to the atomic structure of the graphene. The lower insets are snapshots of the MD (left) and DFT (right) models. The side length L and offset L_0 are defined in the upper inset. All DFT calculations in this study were performed by Dr. Erin R. Johnson's group. 28

2.12 (a) Increase of maximum (initial) flake velocity with mismatch ratio predicted by the analytical model and by MD simulations of perfectly flat graphene having three different sizes. Variation of lateral force with offset position for 100 Å square graphene with an initial offset of 70 Å predicted by (b) an MD simulation of rough graphene (R_q=0.2 Å) and (c) the corresponding analytical model (c=0.01 eV×ps/Å^2). 30

2.13 Decaying oscillatory motion of laterally-offset graphene. Low damping: (a) MD simulation with R_q=0.2 Å and (b) analytical model with c=0.01 eV×ps/Å^2, both for 100 Å square graphene with an initial offset of 30 Å. Moderate damping: (c) MD simulation with R_q=0.44 Å and (d) analytical model with c=0.04 eV×ps/Å^2, both for 100 Å square graphene with an initial offset of 30 Å. High damping: (e) experimental measurements from Ref. [4] and (f) the analytical model with c=0.25 eV×ps/Å^2, both for 3 μm square graphene with initial offset 70 Å. 31

2.14 Decay rate increasing with roughness from MD (lower x-axis) and with the magnitude of friction c from the analytical model (upper x-axis); the dashed line represents a linear fit to both data sets. The lower shaded region identifies the range of roughnesses and corresponding decay rates accessible to an MD simulation while the upper shaded region represents the range of c values and corresponding decay rates for which the model predictions are comparable to the experimental data in Figure 2.13(e). 33

2.15 Models of bilayer (a) graphene, (c) BN, and (e) MoS$_2$ layers. The structures of these materials are shown in greater detail in the right-hand panels (b, d, and f). 36

2.16 DFT potential energy surfaces for relative layer sliding in bilayer (a) graphene, (c) BN, and (e) MoS$_2$, in meV per unit cell. The atom labels on the color maps represent the bottom layer and the origin of the plot corresponds to the energy minimum. A comparison between the DFT and MD inter-layer interaction energy per unit area in the (111)-direction (i.e. the longer diagonal of the left panels) is also shown for (b) graphene, (d) BN, and (f) MoS$_2$. All DFT calculations in this study were performed by Dr. Erin R. Johnson's group. . . . 38

2.17 MD-predicted oscillatory and self-retraction motion of laterally-offset (a) graphene, (b) BN, and (c) MoS$_2$ with variable energy barriers controlled by changing the LJ parameter ε. For MoS$_2$ with $\varepsilon = 0.5\varepsilon_0$, the displaced layer does not retract to the initial, maximally-overlapping position. (d) Decay rate as a function of energy barrier for graphene and BN; the data is fit to an exponential function $y(x) = ae^{bx}$ with prefactor $a = 2.522 \times 10^{-4}$ and $b = 0.2766$. 40

2.18 MD-predicted oscillatory and self-retraction motion of laterally-offset (a) graphene and (b) MoS_2 with variable energy barriers controlled by changing the LJ parameter σ. For graphene with $0.5\sigma_0$, the displaced layer does not retract to the initial, maximally-overlapping position. 41

2.19 Decay rate as a function of roughness from MD simulations for graphene and BN with the original and artificially-increased LJ interaction strength. 43

2.20 Oscillation behavior of graphene (left) and BN (right) predicted by the reduced-order model with different interaction strengths and roughnesses. 45

2.21 MD models of a hemispherical tip (upper image) and a thiol-passivated TiN tip (lower image and inset) sliding on d-AlCoNi substrate. Spheres represent atom positions where colors correspond to different elements: yellow - Ti, black - N, dark green - C, light blue - S, pink - H, red - Co, green - Ni, blue - Al. 50

2.22 Average friction force increasing with load for a hemispherical aluminum tip sliding on an H1 approximant substrate. Friction magnitude is reasonable, but the frictional anisotropy is opposite to that observed in previous experiments. Wear was observed at even moderate loads precluding characterization of friction above ~ 6 nN. 51

2.23 Average friction force increasing with load for a thiol-passivated TiN tip sliding on the H1 approximant substrate. No surface wear is observed, and both the magnitude and the anisotropy of the friction are roughly consistent with experiment. 52

2.24 Sample run from Fig. 2.23 for the quasiperiodic direction at 80 nN load. The time series is noisy, but the pseudoperiod of $\sim$ 82–98 ps enables us to estimate error bars of smaller than 1.5 nN to the average negative lateral force of 18.7 nN. (The first 400 ps are excluded in computing the average.) 53

2.25 The trajectories of the last carbon atom in the thiol chains when the tip slid in the (a) z-direction (periodic) and (b) x-direction (quasiperiodic). The z-periodicity is 4.03Å, while the periodicity of the approximant in the quasiperiodic x direction is 12.22Å. The gray-scale maps show the vertical heights of the quasicystal surface in Angstroms. 55

2.26 Relative distribution of lateral position of carbon atoms during the second half of the simulation dragging in the quasiperiodic direction (*i.e.*, the position axis is along the *periodic* direction.) Only atoms with absolute height less than 38 Å, about 2.6 Å above the nominal surface height, are counted. Split peaks centered at 6.3 Å, 19.9 Å, and 31.6 Å are consistent with carbons localized near furrow edges, where the furrows are spaced 12.22 Å apart. 57

2.27 Adhesive energies (left) and maximum adhesive forces during lift-off (right) after runs at 80 nN load of durations between 100 ps and 800 ps. The graphs show greater adhesion for runs in the periodic direction, consistent with entrainment of thiol chains in furrows. . 58

2.28 Snapshots of the MD simulations of an amorphous SiO_2 AFM tip apex sliding on a multilayer graphene surface with (right) and without (left) water molecules in the interface. 62

2.29 An AFM measurement of load-dependent friction hysteresis on graphene. Black squares show the friction measured while the load was increased to a pre-determined value (loading) and red circles show the friction measured while the load was decreased from the pre-determined set point until the tip was pulled out of contact with the sample. Error bars represent the standard deviation in the mean value of friction calculated. AFM experiments in this study were performed by Dr. Philip Egberts 63

2.30 Load-dependent friction from simulations run in vacuum (loading and unloading represented by black squares and purple circles, respectively) and humid air. Blue triangles (solid and hollow for loading and unloading, respectively) are the friction for the standard water-graphene interaction strength (hydrophobic, 112° contact angle) and red diamonds (solid and hollow for loading and unloading, respectively) correspond to friction from simulations with the artificially strengthened interactions (hydrophilic, 40° contact angle). 65

2.31 Radial distribution function of the O-O pairs in the water in the contact calculated during loading and unloading. Inset is a close up of the first RDF peak indicating there is some irreversible reorganization between loading and unloading, but the magnitude of this hysteresis (difference between RDF peak height during loading and unloading) is not dependant on contact angle. 68

2.32 Number of water molecules in the contact (a measure of contact area) with the substrate during loading and unloading process. Blue triangles (solid and hollow for loading and unloading, respectively) correspond to the standard water-graphene interaction strength (hydrophobic graphene, 112° contact angle) and red diamonds (solid and hollow for loading and unloading, respectively) correspond to the artificially strengthened interactions (hydrophilic graphene, 40° contact angle). Dashed lines represent the contact area of the water on the graphene without the tip present. 70

2.33 Snapshots of the tip/water sliding (from right to left) along the surface at 0 nN during loading (left) and unloading (right). Only the oxygen atoms at the perimeter of the water droplet are shown in the snapshot from the MD simulation to simplify the image. The contact angles have been determined using the linear fits (thick dashed lines) of the outer edges of the water ball and are denoted θ_{front} and θ_{back} for each case. 71

3.1 Illustration of the MD simulation of a 5.6 nm diameter AFM tip sliding over graphite with a step edge. 76

3.2 Lateral force for (a) sharp, (b) 25% truncated and (c) 50% truncated tips scanning across the graphite step edge. The tip diameter is 5.6 nm and the normal load is 0 nN in these three plots. (d) Variation of specific features of the lateral force traces with amount of tip truncation. 77

3.3 (a) The vertical positions of tips of different bluntness scanning forward across the step edge. Potential energy of the (a) sharp, (b) 25% truncated and (b) 50% truncated tips scanning forward across the step edge. 78

3.4 Illustration of the molecular dynamics simulation of a 2.8 nm radius AFM tip sliding over exposed (top figure) and buried (bottom figure) step edges on graphite. 81

3.5 AFM measurements of step edges on HOPG obtained using a sharp tip: (a) topography and (b) lateral force, where the exposed and buried steps can be identified by the different contrast. 82

3.6 Line profiles of the lateral force at exposed and buried steps obtained using a sharp tip from (a) AFM and (b) MD simulations. Results are displayed such that the tip moves down the step during forward scans (black lines) and up the step during backward scans (red lines). 83

3.7 AFM measurements of step edges on HOPG obtained using a blunt tip: (a) topography and (b) lateral force, where the exposed and buried steps can be identified by the different contrast. 84

3.8 Line profiles of the lateral force at exposed and buried steps obtained using a blunt tip from (a) AFM and (b) MD simulations. Results are displayed such that the tip moves down the step during forward scans (black lines) and up the step during backward scans (red lines). 85

3.9 (a) The trajectories of the sharp and blunt model tips as they move over exposed and buried steps. These trajectories are the convolution of the topography of the surfaces and the tip shape, illustrated in the insets. (b) The peak friction force at the step as a function of the angle of the trajectory relative to the horizontal. The dashed line is a fit to equation $F = \tan\theta F_a$. 86

3.10 (a) The potential energy of the tip as it moves down the step where the energy barrier is identified as the difference between the maximum energy and the energy on a terrace. (b) The friction peak at the step as a function of the energy barrier. (c) The energy barrier as a function of the maximum separation distance where the dashed line is a power law fit to the data. 88

4.1 MD simulation results of step friction on graphite. Friction line profile acquired under (A) vacuum conditions (normal force = 0 nN) and (B) dry nitrogen conditions, having two layers of water (normal force = 0 nN). The load dependence of friction measured (C) in vacuum and (D) with water. Illustrations of the 2 nm radius tip sliding over the graphite substrate (E) in vacuum and (F) with water. (A), (B), (E) and (F) are from simulations conducted at 300 K. The load dependence results in (C) and (D) were acquired at 10 K. 93

4.2 Friction force vs. scanning speed for Tip 1 (black squares) and 2 (red circles). The solid line (Tip 1) and dashed line (Tip 2) are fits of the PTT model to the data, which yield, for Tip 1: F_c= 1.5±0.2 nN, β = (4.8±2.0)×10^5 $N^{3/2}$/J, and f_0 = 108±42 kHz; and for Tip 2: F_c = 0.9±0.2 nN, β = (2.5±0.3)10^5 $N^{3/2}$/J, and f_0 = 700±200 kHz. The normal applied force is 0.0±0.2 nN in both data sets. Error bars represent the standard deviation in the calculated mean friction force. Right insets are pre-mortem TEM images of the tips used for data acquisition. Top inset shows a friction loop acquired with Tip 1 at ∼5.8 μm/s; atomic stick-slip pattern can be clearly resolved corresponding to scanning along the [110] direction. Arrows indicate the scan direction. AFM experiments in this study were performed by Dr. Robert W. Carpick's group. 99

4.3 Friction force as a function of scanning speed from MD at 300 K (cyan diamonds) and 0.5 K (purple triangles), and PRD (blue circles) at 300 K. Dashed lines indicate fits of the PRD data to the PTT model using a value of F_c from the simulations at 0.5 K of 2.56±0.02 nN, yielding β = (2.9±0.2)×10^5 $N^{3/2}$/J, and f_0 = 120±30 GHz. Left inset: model of the SiO_2 tip and the Au(111) substrate. Top right inset: a friction loop showing clear atomic stick-slip along the [100] direction. Arrows indicate the scan direction. Experiments in this study were performed by Dr. Robert W. Carpick's group. . . 100

4.4 MD (cyan and red solid diamonds), PRD (blue solid circles), and experimental results from Tip 1 (black squares) plotted together. MD predictions are reported for 1 nm (cyan diamonds) and 2.2 nm (red diamonds) contact radii; the relationship between F_c and contact size is also used to extrapolate the PRD data (blue hollow circles) 101

4.5 Snapshot of an MD simulation of a hemispherical diamond tip sliding on (a) graphene (b) BN and (c) $\mathrm{MoS_2}$. 106

4.6 Friction trace on (a) graphene (b) BN and (c) $\mathrm{MoS_2}$ surface. (d) Mean friction of three different materials. 107

4.7 Temperature dependence of friction on on (a) graphene (b) BN and (c) $\mathrm{MoS_2}$ surfaces.(d) Potential energy surfaces on different materials. 108

5.1 Snapshot from a molecular dynamics simulation of the apex of a 32 nm radius AFM tip placed on a seven layer graphite substrate. . . . 111

5.2 Contact resistance as a function of load measured by conducting AFM with (a) 32 nm and (b) 77 nm tips on graphite. Credit to Dr. M.H.Lee's group 113

5.3 Illustration of the real (black spheres) and apparent (color contour) contact areas for the (a) 32 nm and (b) 77 nm tips from an MD simulation of contact with a 200 nN load. The colors in the contour plot reflect local distances between the tip and substrate; legend units are nm. 115

5.4 (a)Variation of real and apparent contact area with load and tip radius calculated from MD simulation. (b)Contact resistivity calculated from the experimentally measured resistance and the simulation-predicted real A_r (hollow symbols) and apparent A_a (solid symbols) contact areas for the 32 nm (squares) and 77 nm (triangles) radius tips. 116

5.5 Atomistic illustration of a monoclinic single cellulose Iβ nanocrystal employed in MD simulations; spheres represent atoms with black carbon, blue oxygen, and yellow hydrogen. 119

5.6 Configurations studied for interfacial thermal resistance: (a) chain, (b) transverse perpendicular, and (c) transverse parallel; The interface regions highlighted in red. 120

LIST OF TABLES

2.1 LJ parameters used in the MD simulations for all atomic pairs. . . 37

2.2 Reduced-order model coefficients A and B for graphene and BN with physical (first row) and artificially-increased ($2\times\varepsilon_0$, second row) interaction strengths. 44

2.3 Frictional forces under 80 nN load with estimated uncertainties. Runs with rigid substrates eliminate lattice-vibration effects. For each type of substrate (non-rigid and rigid), the first row gives the frictional forces along the periodic and quasiperiodic directions. Friction and error bars in nN are estimated from equal-duration bins given by the pseudo-period, with the error bar the standard deviation of the mean of the independent bins. The row labeled "worst" for each substrate type replaces the pseudo-period and error bar derived from an alternative binning procedure in which the bins are either as given previously, 20% larger or smaller, or twice or half as large, *whichever yields the largest error bar*. For both substrates, the periodic friction is larger than the quasiperiodic by at least seven standard deviations of the mean. 54

2.4 Contact angles in front of and in back of the tip during loading and unloading for each equilibrium contact angle. θ_0 is the equilibrium contact angle and $\theta_L - \theta_U$ is the contact angle hysteresis, the difference between the loading and unloading angles. 72

5.1 Summary of anisotropic thermal conductivity of aligned CNCs. . . 122

ABSTRACT

Tribology is the science and engineering of friction, adhesion, wear and lubrication of sliding/interacting interfaces. It is truly interdisciplinary, as tribological properties (friction, wear, etc.) are directly related to the mechanical properties, thermal transport, electrical properties, and chemical reactions at interfaces. Generally, nanotribological studies, or examination of tribological phenomena at the nanometer length-scale, are important for two reasons: first, for fundamental understanding of interfacial phenomena on a small scale; and second, for the enhanced performance of nanoscale mechanical components as well as the development of next generation devices.

Lubricants are an important component of tribology for their ability to reduce friction and wear to save energy while increasing a machine's useful life. Solid lubricants, such as 2D materials (graphene, molybdenum disulfide, boron nitride) and soft metals/metal alloys, are especially useful for lubricating machine components that operate under extreme conditions (such as very high temperatures, very high applied pressures and very fast/slow sliding speeds). Under these conditions, most liquid/oil-based lubricants fail due to decomposition or oxidization at very high temperatures, or have reduced performance at very high pressure and very low sliding speeds. In this thesis, we use molecular dynamics simulations and atomic force microscope experiments to investigate tribological properties of solid lubricants under various conditions and additionally address some of the atomic scale mechanisms that contribute to thermal and electrical phenomena at the interface. Specifically, we discuss (1) tribological behavior on flat surfaces, (2) tribological behavior on surfaces with defects, (3) tribological behavior under extreme conditions, and (4) thermal and electrical transport at nanoscale interfaces. Our study provides insight to the molecular origins of interfacial phenomena and their application to next generation devices.

Chapter 1

INTRODUCTION

1.1 2D Materials and Beyond

Developments in nanoscale manufacturing and production technology have brought new classes of materials to the world. In nature, most materials are three-dimensional (3D) with their structures arranged in all directions in space. However, scientists have successfully fabricated two-dimensional (2D), one-dimensional (1D) and zero-dimensional (0D) materials in recent decades; see illustration in Fig. 1.1 [1]. These new classes of materials have novel properties that common 3D materials do not share. For example, it was observed that, for 0D materials (nanoparticles), the melting temperature is significantly lower [5], the catalytic activity is much higher [6], and the electrical and thermal conductivity are smaller than their bulk counterparts. Also, for 1D materials (nanotubes and nanorods), it was reported that the mechanical properties as well as electrical and thermal conductivity of most 1D materials are smaller than bulk materials. However, carbon nanotudes are a special case that have the third highest tensile strength of all the materials and very high thermal and electrical conductivity [7]. For 2D materials (layered materials), very unique properties have been revealed which will be discussed in detail in the following paragraphs.

Generally, 2D materials have high specific surface area, which is significant for sensing, catalysis and energy storage applications [8]. In addition, 2D materials, such as graphene, hexagonal boron nitride ($\alpha - BN$), and molybdenum disulfide (MoS_2), exhibit their own unique properties. Graphene is a one atom thick, honeycomb lattice made of carbon atoms as shown in Fig. 1.2 (a) and (b). The term graphene, which describes a single layer of graphite, was introduced by Mouras, et al. in 1987 [9]. However, graphene was only a concept until it was first obtained experimentally using scotch tap in 2004 [10]. Graphene has an extremely high Young's modulus, excellent thermal and electrical properties, extremely low friction and high resistivity to corrosion [11]. In addition to these beneficial properties, the simple manufacturing procedure, low cost and wide availability of this material make it promising for many potential applications in a wide range of fields such as, transistors, nanoswitch, nanomoters, bio-sensors, touch screens, surface coating for wear and corrosion detection, and solar cells [12]. Lastly, the low interlayer interaction strength of multilayer graphene (graphite) leads to low friction behavior that makes

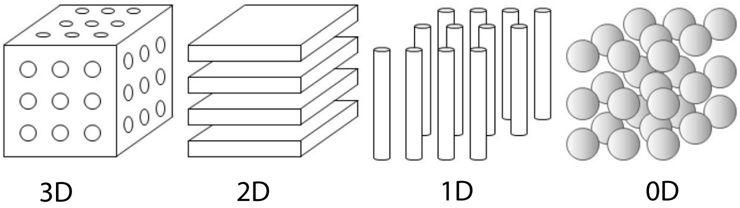

Figure 1.1: Classification of materials; figure from [1].

it good for many tribological applications (which will be discussed in detail later). $\alpha - BN$ is another 2D material with structure similar to graphite, as illustrated in Fig. 1.2 (c) and (d). It is made up of hexagonal rings in which every boron atom is connected to three nitrogen atoms and vice versa. Due to the low interaction strength between $\alpha - BN$ layers and excellent thermal and chemical stability, it has been used for tribological application at both low and high temperatures (up to 1000 C) [13]. Currently, fine grained $\alpha - BN$ is used by nearly all leading cosmetic products because of its non-toxic chemical stability and lubrication properties for smoothness [14]. MoS_2 is a 2D material with a different structure from graphene or $\alpha - BN$; the structure is illustrated in Fig. 1.2 (e) and (f). It has a highly anisotropic crystal layer structure, which consists of a layer of Mo atoms arranged in an hexagonal array. Each atom of Mo is surrounded at equal distance by six S atoms placed at the corners of a triangular prism. The doped MoS_2 is good catalysts [15]. The weak interlayer interaction allows foreign ions or molecules to be trapped between the layers. Thus, MoS_2 could be used in high energy density batteries [16] and hydrogen storage [17]. In addition, its weak interlayer interaction also results in low friction coefficients during sliding which enables MoS_2 to perform well in many tribological applications [18].

To summarize, 2D materials, such as graphene, $\alpha - BN$ and MoS_2, can be used for a variety of device and machine applications due to their good frictional properties, and excellent electrical and thermal properties. The performance and efficiency of these devices/machines can be significantly improved by understanding and then tuning these properties. In the following sections, a detailed discussion of the tribological, thermal and electrical properties of 2D materials will be presented. In addition, a few selected 3D materials (metal and metal alloys) will also be investigated.

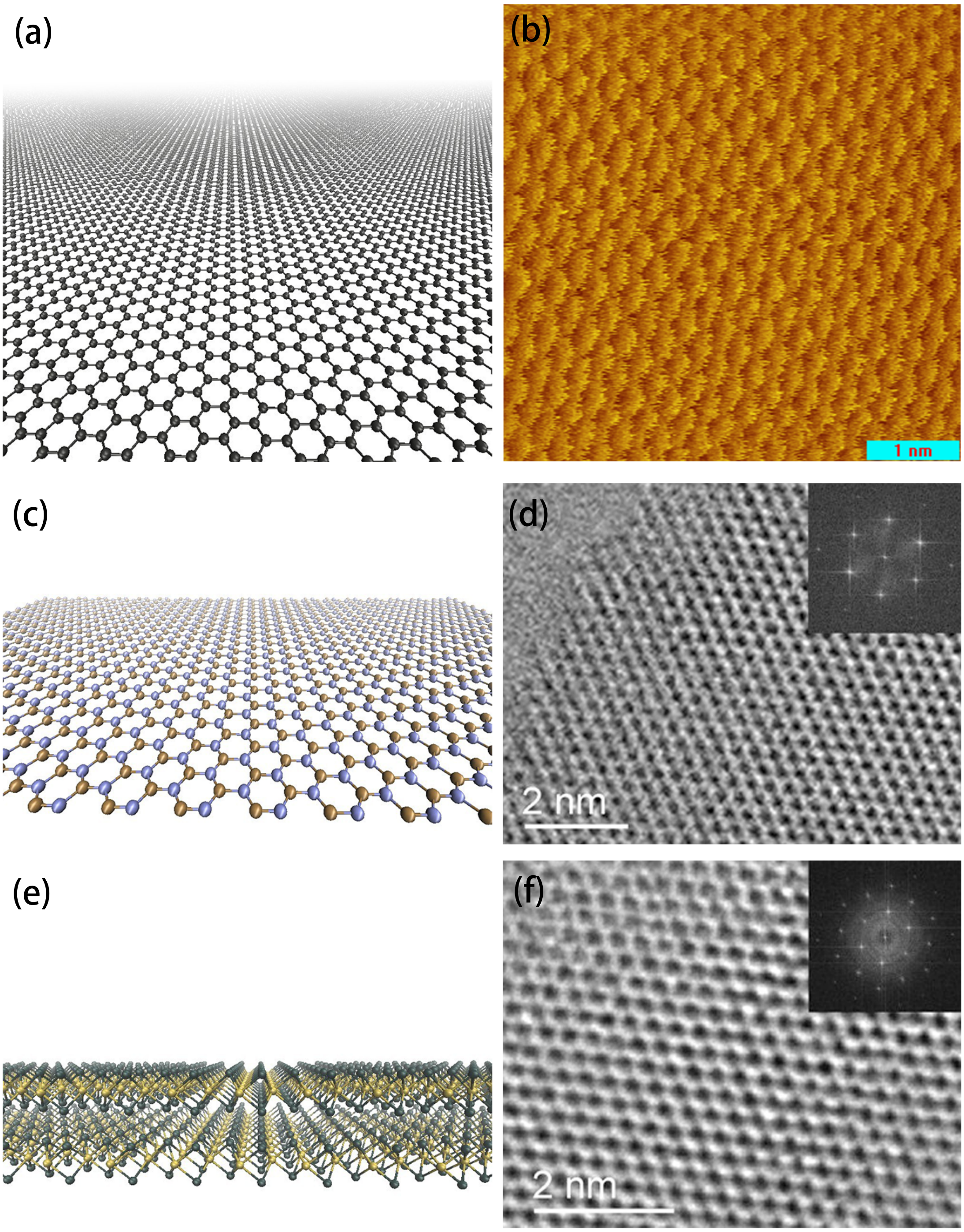

Figure 1.2: (a) MD image of graphene, (b) AFM lateral force image of graphene from Dr. R.W. Carpick's group, (c) MD image of $\alpha - BN$, (d) TEM image of graphene from [2], (e) MD image of MoS_2, (f) TEM image of graphene from [2]

1.2 Tribological Properties

1.2.1 Background and Motivation

Friction, the force resisting relative motion of any interacting surfaces, was studied by Leonardo Da Vinci (1452-1519) in the early 15th century [19]. Then in the 17th centruy, Guillaume Amontons (1663-1705) developed the first theory of macroscopic friction, known as Amontons' law: friction is directly proportional to applied load and independent of apparent contact area [19]. This simple empirical relation has been applied to a variety of sophisticated machines and devices for centuries. Friction, the major cause of dissipative energy loss, has been a challenge since mankind began using machines. Researchers reported that the friction accounted for 6% of the annual gross domestic product in the United States in 1966 [20]. In 1977, a strategy for energy conservation through tribology in the United States was presented by Pinkus and Wilcock [21]. Their report estimated that 11% of the energy consumption in the areas of road transportation, power generation, and industrial machinery and processes could easily be saved. These areas account for about 80% of the total energy consumption in the United States. More recently, it was reported that, in passenger cars, one-third of the fuel energy is used to overcome friction in the engine, transmission, tires, and brakes. Direct frictional losses, with braking friction excluded, are 28% of the fuel energy, and, worldwide, 208,000 million liters of fuel (gasoline and diesel) was used in 2009 to overcome friction in passenger cars [22]. This report also showed that by taking advantage of new technology for friction reduction in passenger cars, friction losses could be reduced by 18% in the short term (510 years) and by 61% in the long term (1525 years) [22]. This would equal a worldwide economic savings of 174,000 million euros and 576,000 million euros, respectively; fuel savings of 117,000 million and 385,000 million liters, respectively; and CO_2 emission reduction of 290 million and 960 million tonnes, respectively [22]. Therefore, reducing energy costs due to friction has become an important and urgent issue. Overall, these reports demonstrate the significant impact that friction can have on industry and global energy costs. Therefore, it is important to understand friction and how to control it.

1.2.2 Atomic Friction

Studying friction at the atomic scale can provide fundamental understanding of how friction occurs [23]. Atomic-scale friction has drawn significant attention and has been at the forefront of scientific interest in recent years. In general, atomic-scale friction study is important because it can lead to a fundamental understanding of friction mechanisms, and because it may enable the development of nano-scale moving components.

Atomic-scale friction can be measured and characterized experimentally using an atomic force microscope (AFM). The first measurement of atomic friction was performed by Mate, McClelland, Erlandsson and Chiang in 1987 [24]. They observed atomic level stick-slip behavior on graphite. An example of similar stick-slip behavior on graphite is shown in Fig. 1.3. The stick-slip pattern reflects the atomic lattice of the substrate.

As technology has developed at smaller scales, it has been discovered that, at the micro/nanoscale, friction varies with a large number of parameters that are not captured by Amontons' law, such as surface structure, environments, sliding velocity and temperature. For example, it was observed that surface structures, such as step edges [25–31], grain boundaries [23, 32, 33] and atom-scale surface roughness [23,34–36] can change atomic friction. Atomic friction was also reported to vary with scanning velocity [37–39] and temperature [38]. Therefore, it is important to study atomic friction in order to understand these trends and the mechanisms underlying friction in general.

2D materials, such as graphene/graphite, $\alpha - BN$ and MoS_2, are generally good lubricants due to their low interaction strength between layers. The weak interlayer interaction leads to low friction, which is the key feature for any lubricant. Graphite, $\alpha - BN$ and MoS_2 have been used as solid lubricants in many fields for decades [8, 13, 18]. Generally, graphite lubricants can be found in many gears in machines. $\alpha - BN$ lubricants have been used in many high temperature machines and cosmetic products. MoS_2 lubricants can be found in motorcycle engines, bicycle coaster brakes and mechanical joints [40].

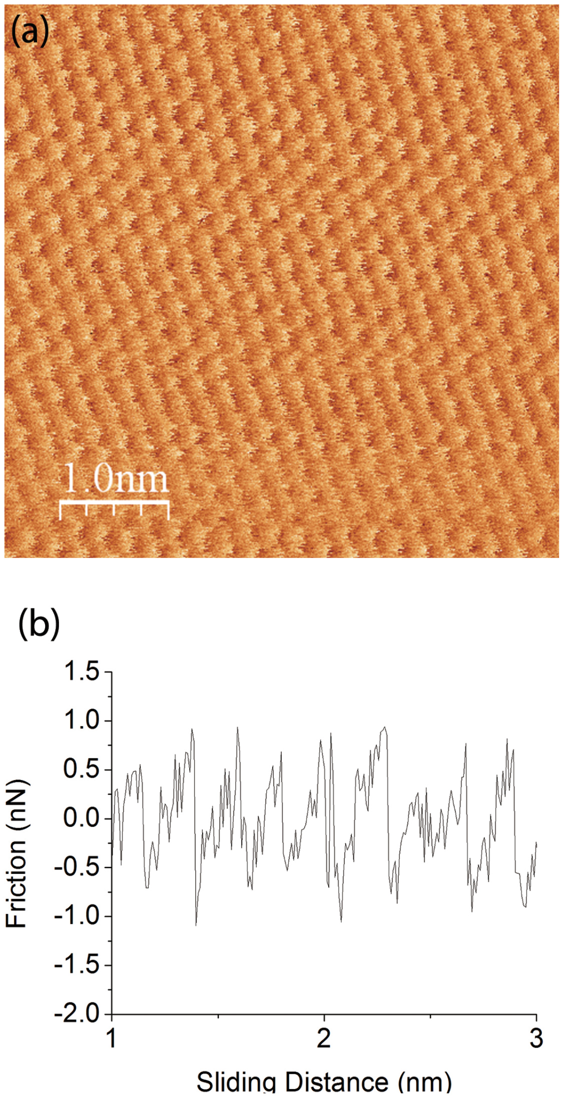

Figure 1.3: AFM measurement of (a) lateral force map and (b) stick-slip friction on graphite ; data from Dr. R.W Carpick's group.

1.3 Thermal and Electrical Properties

1.3.1 Background and Motivation

Tribology is truly interdisciplinary, as tribological phenomena are directly related to the mechanics, thermal science, electrical engineering, and chemistry at the interfaces. Thermal science is a field that deals with the study and application of thermal energy transfer (heat transfer). It involves the generation, use, conversion, and exchange of thermal energy and heat between physical systems. As such, thermal engineering is involved in almost every sector of the economy and everywhere of our daily lives. Therefore, understanding heat transfer mechanisms is important for development of thermal engineering. Generally, there are four modes of heat transfer: heat conduction, the transfer of thermal energy between physical contacted objects; heat convection, the transfer of heat from one place to another by the movement of fluids; radiation, the transfer of thermal energy to or from a body by means of the emission or absorption of electromagnetic radiation; advection, the transfer of thermal energy from one location to another as a side effect of physically moving an object containing that energy. Heat conduction is the most important mode for many thermal applications. In this proposal, we will focus on heat conduction. The heat conduction through a material depends on its thermal conductivity, which is usually described by Fourier heat conduction theory. Fourier's law states that the time rate of heat transfer through a material is proportional to the negative gradient in the temperature and to the area.

Electrical engineering is a field of engineering that generally deals with the study and application of electricity, electronics, and electromagnetism. Electrical charge was discovered by William Gilbert at the early 17th century [41]. The relationship between electric current and potential difference was introduced by Georg Ohm in 1827, which is known now as the famous Ohm's law. Ohm's law states that the current through a material between two points is directly proportional to the potential difference across the two points. However Ohm's law is not always obeyed. Any given material will break down under a strong-enough electric field, and certain materials are "non-ohmic" under weak fields. Therefore, studying the electrical properties (such as electrical conductivity and resistance) of materials is important not only for understanding the mechanisms but also for enhancing the performance and reducing the energy cost of electrical devices.

1.3.2 Thermal and Electrical Properties at The Nanoscale

As demand for high density, high speed electronic, electromechanical and thermal devices continues to increase, implementation of true nanoscale structures has become critical for next generation electronics and thermal engineering [42–44]. Thermal and electrical properties at the nanoscale have been at the forefront of scientific interest in recent years. In general, studying atomic-scale thermal and electrical properties is important because it can lead to a fundamental understanding of conduction mechanisms, and because it may enable the development of nano-scale electronics and thermal devices.

2D materials, such as graphene, $\alpha - BN$ and MoS_2, with very unique electrical and thermal properties, are suitable for many electrical and thermal applications, such as fuel cells, field effect transistors, battery, nanoswitches, nanomotors [8,12,45]. Recent studies revealed that, at the nanoscale, electrical and thermal behaviors of 2D material are different from those at the macroscale [5, 12].

For thermal properties, there are several inconsistent experimental reports about the thermal conductivity of 2D materials at the nanoscale which suggest additional research is needed. For graphene, several studies reported that the thermal conductivity of graphene increased as the temperature [46–49] while others showed the opposite trend [50–53]. Also, studies revealed that the thermal conductivity increased as the number of layers [47,54], while others observed the opposite [49,55,56]. In addition, it was reported that there was no size dependence of graphene thermal conductivity based on sample sizes from 2.9 to 9.7 um in diameter [51], while other studies showed two different trends: conductivity decreased [51, 57] or increased [53, 58] with graphene size. For MoS_2 and $\alpha - BN$, there are limited reports on the thermal properties at the nanoscale. Studies showed the thermal conductivity of MoS_2 was independent of number of layers [59, 60], while the temperature dependence of thermal conductivity of $\alpha - BN$ was reported by others [61]. Overall, the thermal conductivity of MoS_2 and $\alpha - BN$ at the nanoscale is not well understood.

For electrical properties of 2D materials at the nanoscale, there is debate about applying classic theory. For example, it was reported that the classic Ohm's law (relationship between current and voltage) was no longer valid when the system size was smaller than the mean free path of the materials [62, 63]. However, other studies have shown that Ohm's law still holds at the atomic scale [64]. In addition, studies showed that the electrical properties of 2D materials can be affected by many factors, such as pressures [65], temperature [65], doping [66], number of layers [67–69] and surface structure [65, 70, 70, 71]. In general, electrical behavior of 2D materials at the nanoscale is not well understood.

The above reports indicate that it is very important to study the electrical and thermal properties of 2D materials. Furthermore, understanding the mechanisms underlying those properties may enable the development of thermal and electrical applications and enhance the tribological performance.

1.4 Molecular Dynamics Simulation

1.4.1 Overview of Molecular Dynamics Simulation

The primary tool that will be used in this research is Molecular dynamics (MD), which is a computer simulation of physical movements of atoms and molecules based on Newtonian dynamics. It is used to describe how positions, velocities, and orientations of molecules change over time. The trajectories of atoms and molecules are determined by numerically solving the Newton's equations of motion for a system of interacting atoms, where forces between the atoms and potential energy are defined by empirical potential energy models. The method was originally introduced in the late 1950s [72]. Since, it has become one of the most powerful tools and has been applied in almost every field, including physics, chemical physics, materials science and biomechanics.

1.4.2 Applications of Molecular Dynamics Simulation

MD simulation has been widely used for many different tribological [23], thermal [73, 74] and electrical [75, 76] applications. It can supplement experimental measurements by providing a detailed atomistic picture and mechanistic interpretations of the observations, as well as predict results under conditions that cannot be measured experimentally. It has been used to predict friction, thermal conductivity, electrical field induced deformation on different materials and under different conditions [23, 73–76]. We will include detailed reviews of previous MD simulation studies on specific topics in the subsections of Chapters 2, 3, 4 and 5.

1.5 Thesis Outline

In this thesis, we aim at applying atomistic simulations and experimental measurements to understand the fundamental mechanisms underlying tribological, thermal and electrical phenomena at nanoscale interfaces. The research focuses on 2D materials that have been shown to have very unique properties including graphene, MoS_2 and $\alpha - BN$ and some selected soft metals and metal alloys. In Chapters 2, 3 and 4, we discuss novel results looking into friction, wear and lubrication properties and mechanisms of solid lubricants under various conditions and specifically address some of the atomic scale mechanisms that contribute to tribological phenomena under extreme conditions. Specifically, we will discuss (1) trioblogical behavior on flat surfaces, (2) tribological behavior on surfaces with defects, and (3) tribological behavior under extreme conditions. In Chapter 5, we investigate electrical and thermal transport properties at nanoscale interfaces. Finally, Chapter 6 concludes with summary remarks and an outlook on future research.

Chapter 2

NANOTRIBOLOGY ON “PERFECT” SURFACES

“Perfect” surfaces, i.e. defect-free and atomically flat single crystal surfaces, have the desirable properties of being well-defined, stable and ordered that are ideal for triobological studies. By selecting these materials, the interface materials can be reliably modeled using physically representative potentials, and reliably accessed experimentally. In this section, we addressed several open questions, discussed below, related to how atomic friction is affected by substrate layers, substrate conditions (suspended or supported), oscillatory motion, surface chemistry and load applied to the interface. The overall goal is to develop new, fundamental understanding of the interfacial friction on a well-defined atomically flat surfaces.

2.1 Effect of Graphene Layers on Atomic Friction

2.1.1 Introduction

Recent measurements have revealed a novel trend where the frictional resistance to sliding is smaller on bilayer graphene than on single layer graphene [77,78]. This trend was confirmed through another set of experiments that included graphene up to four layers and other layered materials [79,80]. The latter experimental measurements were explained by a puckering effect where a wrinkle in front of the AFM tip that resists sliding is more dominant with fewer layers.

Since the AFM studies cannot provide direct evidence as to what is happening in the interface buried between the probe and graphene, molecular dynamics simulations have been introduced to help explain the observed behaviors. In two cases the experimental trend was reproduced, i.e. friction decreased with the number of graphene layers [81,82], while in another case the opposite trend was observed [83]. However, none of them proved or disproved the puckering mechanism proposed based on the experimental measurements.

Here, we report physically-representative atomistic simulations of friction on variable-layered graphene that (a) reproduce the experimentally observed trends, (b) support the theory that wrinkles resist sliding, (c) show the behavior is affected by model sheet size, and (d) illustrate the connections between number of layers, sheet size and wrinkle height through flexural rigidity and binding energy.

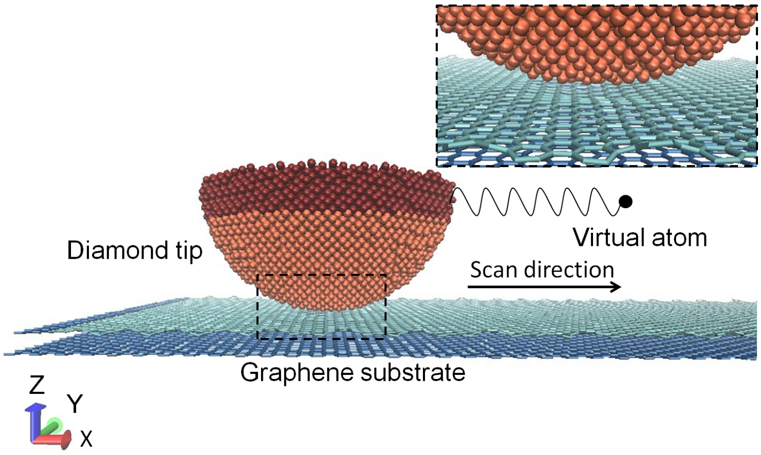

Figure 2.1: Snapshot of the model system where a hemispherical diamond tip is connected to a harmonic spring which pulls it over graphene layers.

2.1.2 Methods

The atomistic model, illustrated in Fig. 2.1, described the apex of an AFM tip scanning over graphene. The graphene sheets were initially 8 nm wide and their lengths were varied from 8 to 52 nm; all were in the zig-zag configuration relative to the sliding direction. The atoms in the bottommost layer of graphene were fixed to model a supporting substrate. Simulations were performed with one, two and three layers of graphene above the fixed layer (i.e. subsequent mention of number of layers does not include the fixed layer) with an initial interlayer distance of 0.335 nm. The atoms at one end (in the scan direction) of all the layers were fixed to prevent relative sliding. The model tip had a hemispherical geometry and consisted of carbon atoms in a diamond structure. The topmost layers of atoms in the tip were treated as a rigid body. A 0 nN external normal load was maintained on the rigid body and it was connected by a harmonic spring to the support that moved with a constant speed of 4 m/s in the x-direction. The spring had stiffness of 8 N/m in the x- and y-directions, but did not resist motion in the z-direction (normal to the graphene surface). A Langevin thermostat was applied to the free atoms in the system to maintain a temperature of 10K; all trends reported were also exhibited at 300K, but the lower temperature enabled more clear illustration of the subtle relationships between friction and structure. The boundaries were non-periodic in the $x-y$ plane, and the boundary in the z-direction was formed by the fixed bottom layer of graphene and the rigid body of atoms at the top of the tip. The inter-atomic interactions within the tip and substrate were described via the Adaptive Intermolecular Reactive Empirical Bond Order (AIREBO) potential [84], and the long range interactions were modeled using the Lennard-Jones (LJ) potential (energy minimum 0.016 eV, minimum energy distance 0.28 nm). The simulations were performed using LAMMPS simulation software.

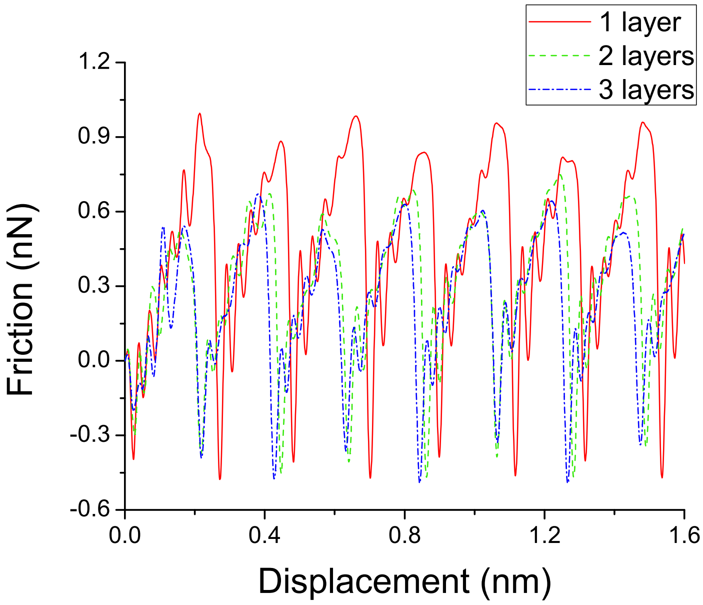

Figure 2.2: Effect of number of graphene layers on friction for 42 nm long sheets.

2.1.3 Results and Discussion

Fig. 2.2 presents a typical friction vs. scanning displacement result from our simulations. For this sheet size (42 nm long) we can clearly see that the peak friction (and also the average friction although not as clearly visible from the figure) decreases as the number of layers increases from 1 to 3. This trend is in agreement with experiment observations [79]. To verify the robustness of this behavior, we performed simulations on graphene with different sizes. The variation of peak friction with number of layers and sheet length is summarized in Fig. 2.3. The results show that, for longer graphene systems, friction decreased with number of layers, consistent with experiment. However, this trend is not observed when the graphene is 24 nm or shorter which suggests that graphene size affects the mechanisms underlying layer-dependent friction.

As mentioned previously, one theory used to explain layer-dependence is the formation of a wrinkle in front of the tip that resists friction, called puckering [79,80], whose effect decreases as the number of layers increases. To explore this possibility,

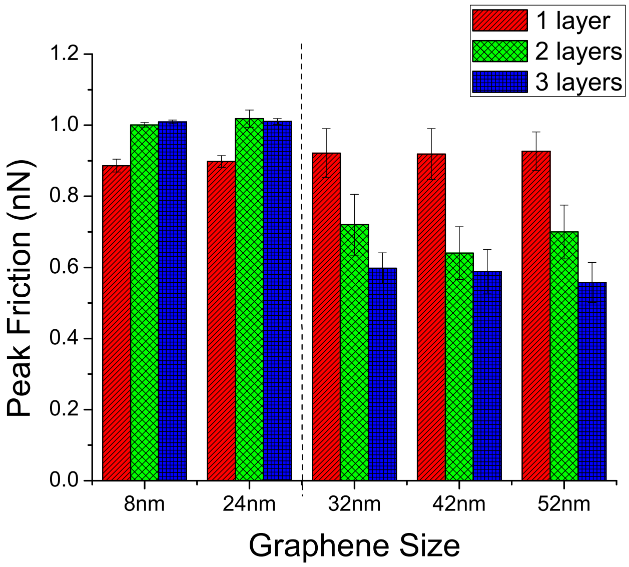

Figure 2.3: The effect of graphene length on frictional layer-dependence.

we tracked the x-direction profiles of the graphene layers near the contact region as they evolved during sliding. An illustration of these profiles is shown in Fig. 2.4. In this example, we can clearly see that the upper graphene layer conforms locally to the tip such that there is a wrinkle in front and back of the tip; a similar pattern can be observed in the second layer but with much smaller amplitude. It is reasonable to expect that these wrinkles might resist sliding and therefore increase friction. To determine if they can also explain the layer-dependence, we calculated the time-averaged height of the wrinkle in front of the tip for the various model sizes. The results, shown in Fig. 2.5, reveal that the size of the wrinkle decreases with increasing number of layers for long graphene sheets, but not for the shorter systems. This is exactly consistent with the friction trends observed in Fig. 2.3, i.e. friction decreases and wrinkle height increases with increasing layers only for graphene 32 nm or longer.

The results shown so far indicate that the dependence of friction on layers and size can be correlated to the formation of wrinkles. This leads to the question of why wrinkle formation is affected by the number of layers or sheet size. We propose a mechanism based on the ability of the sheets to resist wrinkle formation.

For longer graphene sheets, we suggest that the multiple graphene layers act together to resist wrinkle formation. In this case, the graphene can be considered to be an elastic body whose flexural rigidity is $D = \frac{Eh^3}{12(1-\nu^2)}$, where E is the Young's

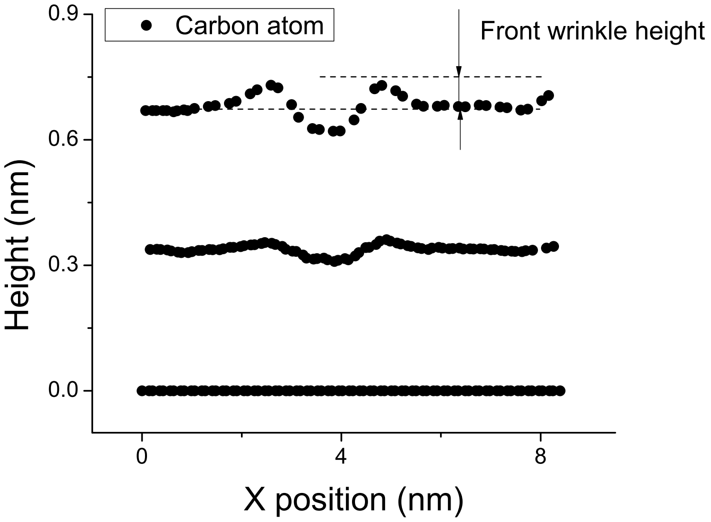

Figure 2.4: Local profiles of the graphene layers during the scanning process.

modulus, ν is Poisson's Ratio, and h is an effective thickness that can be correlated to the number of graphene layers. This expression tells us that, as its thickness increases, the flexural rigidity of the material will increase and it will be harder to bend. Although flexural rigidity is typically used to describe the resistance of a material to global bending, it was recently shown to also be related to local out-of-plane deformation; specifically, the square of the out-of-plane displacement was found to be inversely proportional to the flexural rigidity [85]. Since flexural rigidity increases with thickness and local deformation decreases with flexural rigidity, this analysis is consistent with our observation that the height of wrinkles decreases with the number of long graphene layers (refer to the results in Fig. 2.5 to the right of the dashed line).

This trend is not observed in the shorter graphene sheets. For these cases, we propose that the sheets do not behave as a single material, and the uppermost sheet does not have the support of those below it to resist the formation of wrinkles. This supposition is supported by the binding energy where, for this system, binding energy is defined as the difference between the per atom configurational energy of the multi-layer materials and that of the layers separated from one another: $E_B = (E_{total} - \sum_{i=1}^{n} E_i)/N$, where E_{total} is the energy for layered material, n is the number of layers, E_i is the energy of individual ith layer graphene and N is the number of atoms. Fig. 2.6 shows that binding energy decreases with sheet size for one, two and three layer systems; this is consistent with size effects reported in

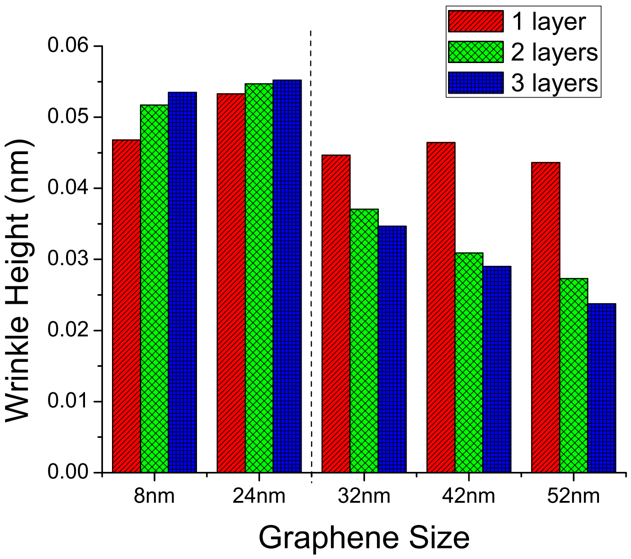

Figure 2.5: Height of the wrinkle in front of the tip varying with number of graphene sheets and their length.

previous studies [86, 87]. The effect in our research is that the structural stability, and therefore the ability of multiple layers to act together to resist near-contact wrinkles, increases with length. The concept of length-induced stability is further supported by a calculation of the average distance between graphene layers which decreased with increasing sheet length; the average distance decreased from 0.340 to 0.337 nm as length increased from 8 to 52 nm. Therefore, in smaller graphene systems, the uppermost layer is less tightly bound to the layer beneath and less able to resist wrinkle formation. This is consistent with our observation that increasing the number of short graphene layers does not result in smaller wrinkles (refer to the results in Fig. 2.5 to the left of the dashed line).

2.1.4 Conclusion

In conclusion, we have used molecular dynamics simulation to explore the mechanisms underlying experimentally observed frictional layer-dependence. Results support the previously-suggested puckering effect by showing that the height of the wrinkle that resists sliding is affected by the number of layers. Further, we show that this effect is dependent on the size of the system such that it is only observed with sufficiently long model sheets. This behavior is rationalized in terms

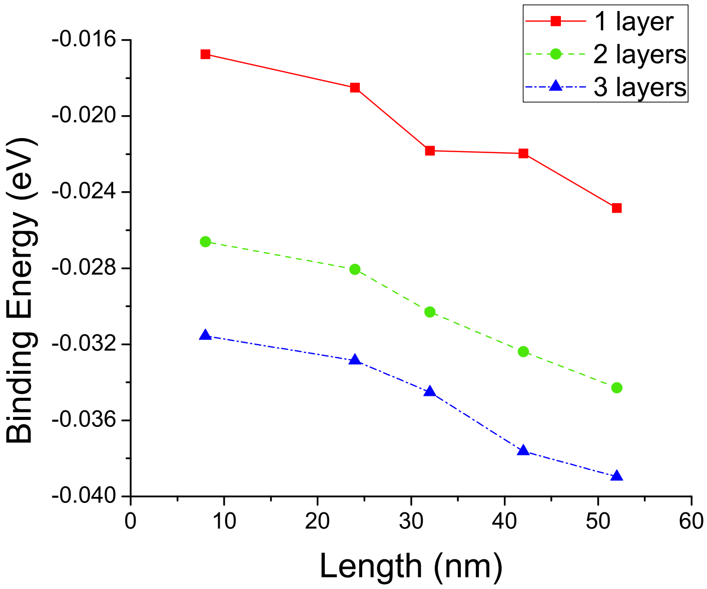

Figure 2.6: Binding energy of multi-layer graphene decrease monotonically with sheet length.

of the ability of multiple sheets to act as a single material as they resist wrinkle formation.

2.2 Negative Friction Coefficient on Suspended Graphene

2.2.1 Introduction

Load is one of the most important parameters in determining friction. The classic Amontons's Law predicts that friction should increase linearly with increasing load (positive load dependence), and this prediction has been observed for friction on a variety of materials, including metals [88,89], ceramics [90], semiconductors [91] and biomaterials [92] and both in ambient and vacuum conditions [77, 88, 91]. Further, the monotonic increase of friction with load has been observed across a range of length scales, from macro to nano, although nanoscale friction sometimes increases with load nonlinearly [93–100]. However, nanoscale friction on graphene, the two dimensional carbon-based material, has been found to exhibit very unique behavior [3, 101–103]. Specifically, on substrate supported graphene, friction increased with load as expected based on the classical theory [77, 91], while suspended monolayers of graphene (graphene deposited on a substrate with circular holes) exhibited a decrease in friction with increasing load (negative load dependence) [101]. In a later study, both positive and negative load dependence were observed on the same suspended graphene in different load regimes [3].

This unique friction behavior has been correlated to adhesion and the out-of-plane deformation of the graphene [3,102,103]. The connection between deformation and friction was supported by molecular dynamics simulations, but those simulations were unable to reproduce the first increasing, then decreasing frictional load dependence [102]. The concept of nanoscale friction on graphene being determined by deformation near the contact has been applied to explain other trends. For example, the local puckering, or formation of a wrinkle in front of the sliding probe was proposed to explain the dependence of friction on number of graphene layers [80]. The correlation between friction and graphene wrinkling was supported by direct atomic-scale evidence from molecular dynamics simulations [104]. Here we apply similar methods to study load dependence.

MD simulations are carried out to study the load dependence of atomic friction on suspended and supported graphene. For the first time, MD simulations of a nanoscale probe sliding on graphene predict the same trends as reported from previous experimental measurements [3, 101]. Friction trends are correlated to the wrinkle in front of the probe, where the height of the wrinkle varies with load in the same way as the friction. Finally, the effects of the empirical potential used to describe the graphene, graphene size, probe size, and graphene-probe interaction strength are investigated.

2.2.2 Methods

The atomistic model is illustrated in Figure 2.7. In this model, the apex of an AFM tip scanned over suspended and substrate-supported graphene with dimensions of 10×10 nm or 100×100 nm. For suspended graphene, the atoms in the center of

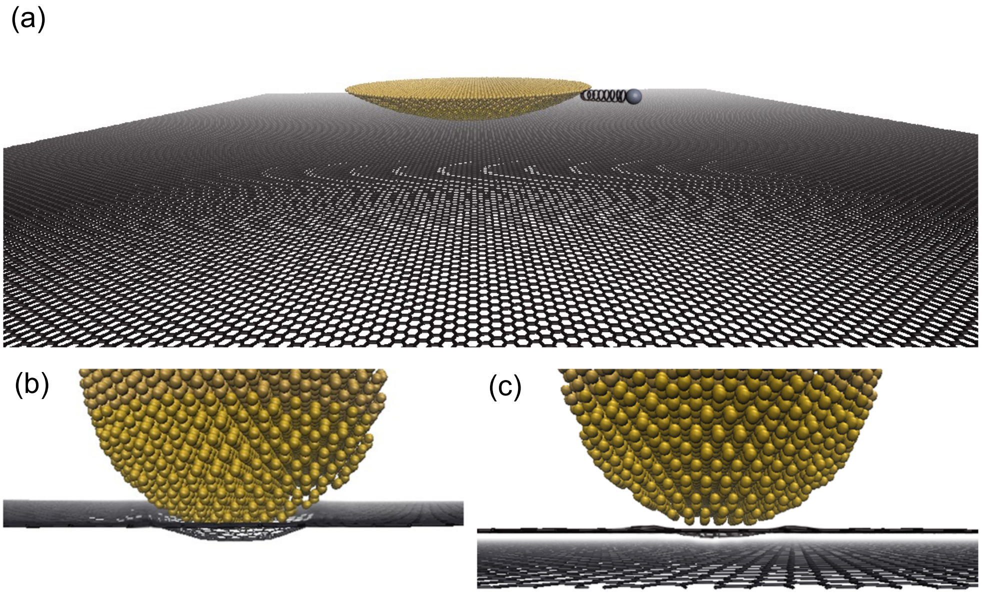

Figure 2.7: (a) Snapshot of an MD simulation of a hemispherical diamond tip sliding on graphene. Close up views of the local deformation on (b) suspended and (c) supported graphene.

a 4 nm or 45 nm radius circle were free and the positions of the rest of atoms were fixed. For supported graphene, the suspended graphene just described was placed immediately above another layer of graphene, where the positions of all atoms in the bottom (substrate) layer were fixed. The graphene interlayer spacing was 0.335 nm. A model probe, or tip, was constructed of diamond in a hemispherical geometry with either a 2.5 nm or 30 nm radius, and 2.5 nm height; the topmost atoms in the tip were treated as a rigid body. An external normal load (from -20 nN to 20 nN) was maintained on the rigid body at the top of the tip. Here, positive load means that the normal force acted towards the graphene and negative load means the normal force pulled the tip away from the graphene. The rigid body was connected by a harmonic spring to the support that moves at 1 m/s in the sliding direction. The spring had stiffness of 8 N/m in the horizontal directions, but did not resist motion in the vertical direction (normal to the graphene surface). A Langevin thermostat was applied to the free atoms in the system to maintain a temperature of 300K. The inter-atomic interactions within the tip and substrate were described via the AIREBO potential [84], and the long range interactions between tip and substrate were modeled using the LJ potential with parameters adopted from Ref. [84]. The simulations were performed using the LAMMPS simulation software [105].

2.2.3 Results and Discussion

Figure 2.8 (a) shows the load dependence of friction on suspended and supported graphene. The presence of the substrate clearly affected the frictional resistance. On supported graphene, friction increased with load, as is commonly observed [77, 91]. This monotonic increase of friction with load was reported for graphene on a variety of substrates and prepared using several different techniques including exfoliation [32], chemical vapor deposition on Cu [106], and thermal decomposition on SiC [77]. The magnitudes of the friction reported in these studies are different, likely reflecting a difference in the strength of the interaction between graphene and substrate. However, the monotonic increase of friction with load on supported graphene was observed in all cases. On suspended graphene, however, the friction first increased and then decreased as the load changed from -12.5 nN to 20 nN; the transition from positive to negative load dependence occurred around at -5 nN. This behavior is consistent with previous experimental observations of both positive and negative load dependence on suspended graphene [3], although our transition point was slightly different from that in the experiments.

Frictional load dependence is commonly associated with the effect of load on contact area [23, 96]. Therefore, we characterized the contact area at different loads, where contact area was calculated from the positions of contacting atoms [97,107], where tip contact atoms are identified as those within 0.3 nm of a substrate atom. The results, shown in Figure 2.8 (b), exhibit the expect trend of increasing contact area with increasing load, for both supported and suspended graphene. For

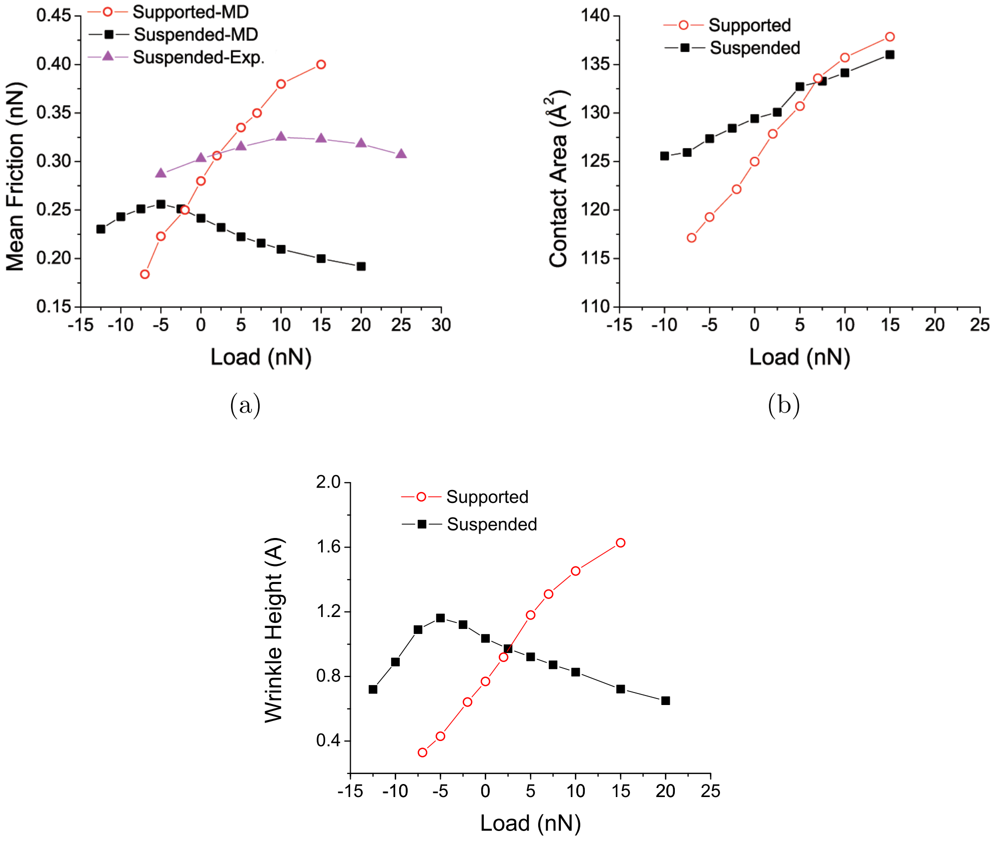

(a)

(b)

(c)

Figure 2.8: Load dependence of (a) friction, (b) contact area, and (c) wrinkle height on supported and suspended graphene. These cases correspond to simulations with a 2.5 nm tip radius and 10×10 nm graphene.

supported graphene, this trend is consistent with that of friction and thus the load dependence of friction can be correlated directly to area. However, for suspended graphene the area and friction trend differ. This suggests that another mechanism complements that of area to determine friction on suspended graphene.

It was shown in previous studies that graphene deforms in the out-of-plane direction to exhibit a puckered region in front of the tip, which was called a wrinkle [80,104]. The wrinkle was believed to provide additional resistance to sliding and the height of the wrinkle was correlated to the magnitude of the friction. Following this reasoning, we characterized the variation of wrinkle height with load. Wrinkle height was calculated as the time averaged difference between the local maximum vertical position of the graphene in front of the tip and the local minimum vertical position of the graphene in the center of the contact. The wrinkle heights at different loads, shown in Figure 2.8(b), exhibited trends similar to that of friction: on supported graphene, both wrinkle height and friction increased monotonically with load, while, on suspended graphene, both wrinkle height and friction increased and then decreased with increasing load.

These trends can be visualized by analyzing the cross-sectional images of the graphene shown in Figure 2.9. In the case of supported graphene, the wrinkle increased in height as the load increased. Also, the wrinkle in front of the tip was notably larger than that behind the tip, particularly at the largest load. The trend on the suspended graphene is less obvious because the wrinkle is small compared to the overall deflection of the graphene. However, if we assume that the graphene material immediately in front of the tip provides the largest resistance to sliding, and correspondingly quantify the wrinkle height as the difference between tip-front local maximum to tip-center local minimum. The validity of this assumption is supported by the fact that the wrinkle height calculated based on it is affected by load in the same way as the friction.

Previous MD simulations were not able to capture the experimentally observed load dependence on suspended graphene. Instead, the opposite trend was observed, where friction first decreased and then increased with load [102]. We found that the difference between the previous study and the one we report here may be due to the fact that the Tersoff bond-order potential was used in previous simulations to describe the graphene interatomic interactions whereas AIREBO was used in this study. Figure 2.10(a) shows the friction on suspended graphene predicted using the Tersoff and AIREBO potentials. We found that that only the simulations performed using AIREBO were able to accurately reproduce experimentally-measured trends. The difference could be correlated to the effect of the potential on surface conformation as shown in the inset of Figure 2.10(a). Specifically, the suspended graphene sheet exhibited much greater overall deformation with the Tersoff potential than with the AIREBO potential. These results suggest that AIREBO is a more reliable potential for friction studies on graphene.

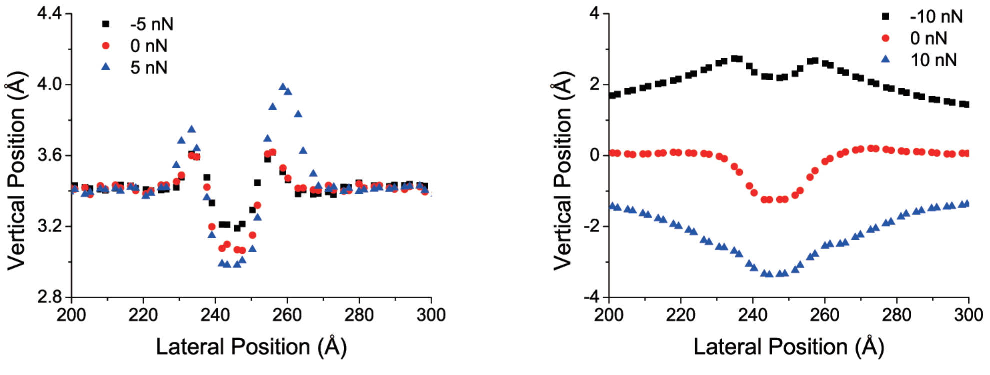

(a) (b)

Figure 2.9: Cross-section images of (a) supported and (b) suspended graphene during sliding at different loads. The sliding direction is left to right. Simulations performed with a 2.5 nm tip radius and 10×10 nm graphene

Figure 2.10(a) shows that our simulations were able to reproduce the experimentally-measured trend, albeit with the transition between increasing and decreasing friction occurring at a different load. This discrepancy may be attributed to the different size of tips in experiment and simulation (tip size effect discussed next) as well as differences in the tip material (UNCD vs. single crystal diamond) and shape (experimental tip not expected to be a perfect hemisphere). Another factor may be the simulation sliding speed, which is several orders of magnitude larger than that in the corresponding experiment (1 m/s vs. 10 nm/s). Unfortunately, classical MD cannot access these slower scanning speeds due to the necessarily small time step. However, we did perform another set of simulations on suspended graphene at 0.5 m/s and observed the same increasing-then-decreasing friction trend with the transition at the same load. Further, the fact that both experiments and simulations exhibit the same trending, despite their very different speeds, suggests that the mechanisms observed in simulations are indeed still applicable to the corresponding experiments.

We also examined other factors that could affect the load dependence of friction: graphene size, tip size and adhesive strength. Figure 2.10(b) shows the load dependence of atomic friction on large (100×100 nm) and small (10×10 nm) graphene. The friction was 14 and 21% (averaged over all loads) greater on the large suspended and supported graphene, respectively. This may be due to the fact that more graphene material was available to deform and contribute to a wrinkle. This hypothesis is supported by the observation that the average wrinkle height on the 100×100 nm graphene was, on average, 21 and 29% greater on suspended and supported graphene, respectively, than on the 10×10 nm graphene. This is qualitatively consistent with the difference in friction on the large and small graphene. Regardless, the same load dependence trends on suspended and supported graphene were observed on graphene of either size investigated here.

We also varied the radius of the model tip (2.5 or 30 nm). As shown in Figure 2.10(c), the increasing and then decreasing friction trend on suspended graphene was observed with either tip. However, the magnitude of the friction was much higher with the large tip. This can be attributed to the fact that the larger tip corresponds to greater contact area [96] and to the correspondingly larger wrinkle (on average five times larger wrinkle height with the larger tip). In addition, we observed that the transition point (transition between positive and negative load dependence) shifted to a smaller load as the tip size increased. This observation suggests that tip size may be one factor causing the transition point we observe in these simulations to differ from that measured experimentally [3].

Previous experiments demonstrated that adhesion is a key factor in determining the load dependence of friction [3, 101]. Here, we controlled the adhesion by varying the strength of the interaction between tip and substrate. Figure 2.10(d) shows the friction predicted on suspended graphene by the model with the original interaction [84] and with an interaction that is 25% weaker. Note that we could not measure friction for larger negative loads since the tip was actually pulled away from the substrate for anything more negative than -10 nN. We observed that the friction increased monotonically with load from -10 nN to 20 nN for the weak interaction strength. This contrasts with the first increasing, then decreasing friction trend exhibited by the simulation with the standard interaction. Again evaluating this in terms of a surface wrinkle, we found that the wrinkle generated with the weak interaction increased monotonically and that with the standard interaction increased and then decrease with increasing load. In general, the wrinkle height was ∼36% smaller in the system with the weaker interaction strength. Interaction strength is directly related to adhesion, which confirms that adhesion plays an important role in determining load dependence of friction.

2.2.4 Conclusion

In this work, MD simulations were used to study the load dependence of atomic friction on suspended and supported graphene. For the first time, MD simulation was able to predict the same trends as observed in previous experiments [3, 101]. On suspended graphene, both positive and negative load dependence of friction were observed, while friction continuously increased with load on substrate supported graphene. The fact that measured friction trends are also observed in atomistic simulations confirms that the underlying mechanisms are localized at the tip-substrate interface. Further, the simulations provide a means of characterizing the local conformation of the graphene, something that cannot at this point

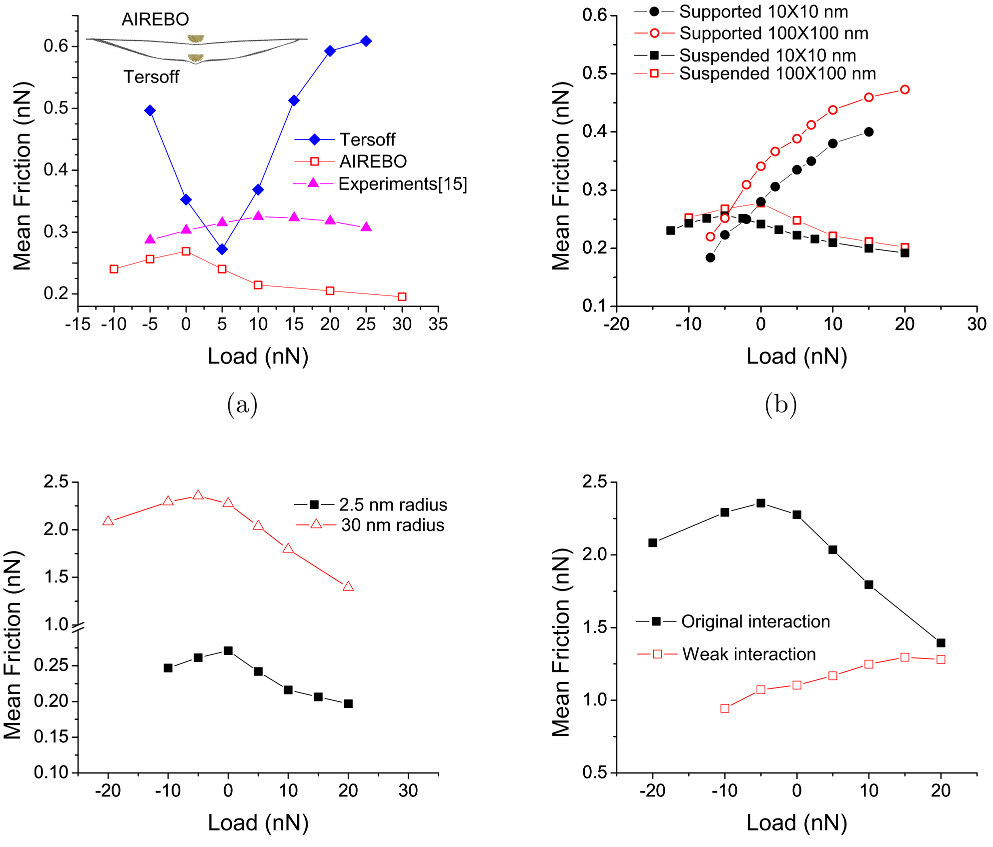

(a) (b)

(c) (d)

Figure 2.10: Load dependence of friction (a) on suspended graphene with Tersoff and AIREBO potentials (2.5 nm radius tip, 100×100 nm graphene), purple triangles represent experimentally-measured friction between an ultrananocrystalline diamond (UNCD) tip and suspended graphene [3], (b) on supported and suspended graphene with side lengths 10 and 100 nm (2.5 nm tip), (c) on suspended graphene with a 2.5 and 30 nm radius tip (100×100 nm graphene), and (d) on suspended graphene with original and 25% weaker interaction strength (30 nm radius tip, 100×100 nm graphene).

be measured directly in an experiment, and they allow us to explore the effect of parameters not easily controlled in an experiment such as tip size and adhesion. We also showed that the empirical potentials used to describe the graphene (Tersoff and AIREBO) had a significant impact on the results; in fact opposite trends were observed using the two different potentials, with AIREBO enabling predictions consistent with experiment. The effect of other factors, including tip size, graphene size and interface interaction strength, were also investigated to determine their effect on friction trends. The size of the graphene and tip affected the magnitude of the friction, but did not affect simulation-predicted load dependence trends. The interaction strength, however, had a more significant affect, where a weaker interaction both decreased the friction and changed the trend such that the negative load dependance was not reproduced. We correlated the observed friction trends with a wrinkle in the graphene that formed in front of the tip and provided additional resistance to sliding. Variations in the height of that wrinkle with load were consistent with the variation in friction, on both suspended and supported graphene. Overall, the MD simulations presented here provide insights into how and why frictional load dependence on 2D materials is affected by the presence of a substrate and other interface conditions.

2.3 Oscillatory Motion of Bilayer Graphene

2.3.1 Introduction

Graphene has many novel properties and characteristics that make it a promising material for a variety of applications. Recently, multilayer graphene was found to exhibit an exciting new behavior where the uppermost layer, after being laterally offset from those below it, retracts to its initial position [4, 108–110], sometimes after oscillating [111]. The physics behind this behavior can be understood easily in terms of energetics: the offset position is energetically unstable, so the upper layer moves towards the overlapping, low energy position [4, 110–114]. The dynamics of the motion are then determined by factors that affect the energy gradient, including commensurability [113, 114] and temperature [4]. Theoretical approaches that capture these effects can reproduce experimentally-observed trends [111, 114, 115], but have not, to this point, predicted self-retraction or oscillatory behavior that is quantitatively comparable to experimental measurements. One reason for this is that prior modeling studies have not included surface roughness and the corresponding effect on the rate at which oscillations are damped. Here, we directly address this issue, thereby enabling a more complete understanding of self-retraction motion.

In this work, MD simulations that explicitly capture graphene surface roughness are carried out. In addition, density functional theory (DFT) calculations are performed to verify that the energetics of the empirical model-based MD simulation are accurate. (All DFT calculations in this study were performed by Dr. Erin R. Johnson's group.) Finally, a reduced-order model is presented that captures both the energetics of the DFT and the roughness-dependent dynamic response of the MD. Model predictions are compared directly to previous experimental results and highlight the important role of roughness in determining motion patterns. Ultimately, since the roughness of graphene can be controlled to some extent by the substrate material and morphology, this work suggests a means of tuning self-retraction or oscillation motion of layered materials.

2.3.2 Methods

DFT calculations were performed by Dr. Erin R. Johnson's group. The details about model used in the DFT calculations can be found in our paper . [116].

The MD simulations consisted of two square graphene flakes (lower left inset of Figure 2.11) with side lengths between 5 and 20 nm where the top flake was initially offset relative to the bottom by a distance L in the armchair direction. The atoms at the two ends of the flakes in the offset direction were treated as rigid bodies. The root-mean-square (R_q) roughness was varied from 0 to 0.7 Å by changing the relative distance between the two ends of the graphene and then allowing the system to relax. The further the two ends of the graphene were compressed, the rougher the final configuration. Model roughnesses were comparable to the range of values measured experimentally for graphene on a boron nitride substrate (0.02-0.17

Å) [117]. The inter-atomic interactions within the graphene flakes were described via the AIREBO potential [84], and the long range interactions between them modeled using the Lennard-Jones potential (energy minimum 0.016 eV, zero-crossing distance 2.8 Å). The accuracy of the potential was validated by comparing the interlayer interaction energy obtained by energy minimization with the empirical potential to that calculated using DFT. A Langevin thermostat was applied to the free atoms in the system to maintain a temperature of 300K and simulations were performed using LAMMPS [105].

2.3.3 Results and Discussion

Despite the difference in size between the MD and DFT model graphene flakes, the energy per unit area predicted by MD and DFT can be overlayed and show good agreement, as seen in Figure 2.11. Both potentials have a characteristic V-shape, exhibiting greater stability at maximum overlap, where the dispersion energy is largest in magnitude [111, 115]. The linear dependence of the energy on the offset implies a constant interaction energy per overlapping area. The potential also has superimposed oscillations due to the periodicity of the graphene lattice [111, 115]. This allows us to introduce a simple one-dimensional model for the potential energy of interaction between two graphene flakes, where the equations of motion can be solved directly [4].

Consider a system of two identical graphene flakes, each with length L_0, width W_0 and area $A_0 = L_0 \times W_0$. The displacement between the centers-of-mass of the flakes (offset) is L and we define a dimensionless displacement or mismatch ratio as $x = L/L_0$. The potential has a characteristic V-shape, with a superimposed sinusoidal oscillation. This can be written as

$$E = k_1 A_0 |x| - k_2 A_0 (1 - |x|) \cos\left(\frac{2\pi L_0 x}{p}\right). \tag{2.1}$$

In this expression, k_1 is the energy density per contact area between the two flakes (discussed later), the period $p = 4.267$ Å is the distance between the centers of adjacent carbon-rings in the armchair direction, and $k_2 = 0.00015$ eV/Å^2 was calculated from the amplitude of the oscillatory energy profile that results from subtracting a V-shaped curve from the MD potential energy vs. mismatch ratio data. We have found that this parameter is roughly constant and independent of the size of the flakes.

We obtain k_1 by linear regression of the MD-predicted energy vs. mismatch x data, which gives 0.011697 eV/Å^2. The value of k_1 determined from the LC-wPBE-XDM calculations on the 5x4-cell double flake is 0.011826 eV/Å^2. k_1 also can be estimated from equivalent DFT-XDM calculations under periodic boundary conditions by displacing two infinite graphene slabs relative to each other and calculating the binding energy with respect to the isolated slabs. Using this method,

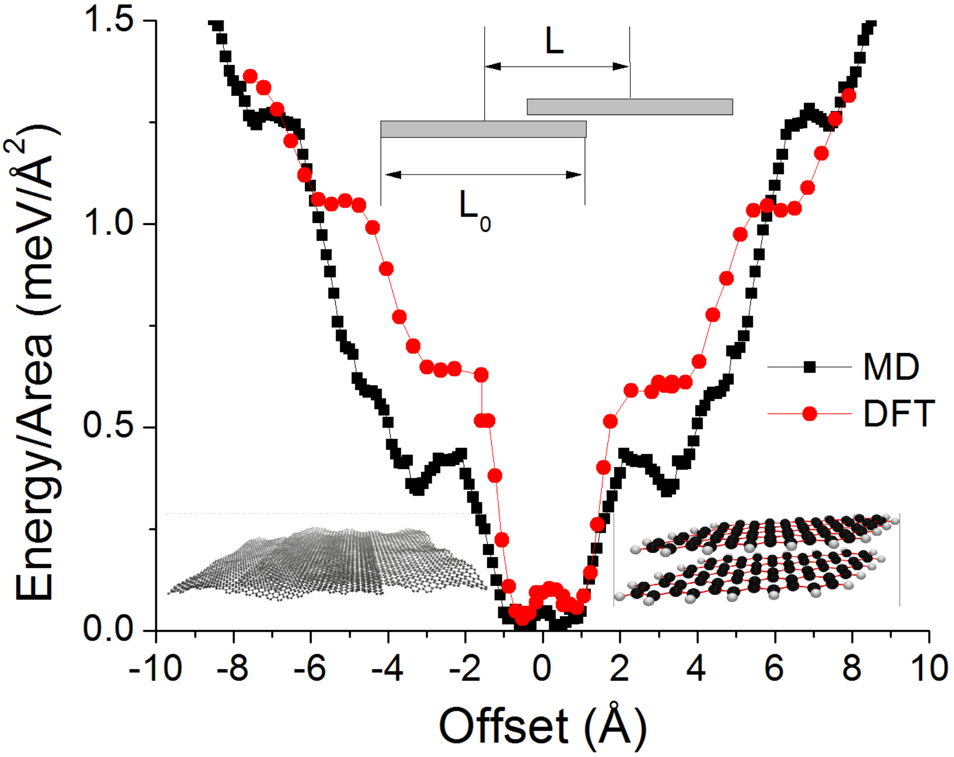

Figure 2.11: Variation in the potential energy with offset position, illustrating the V-shaped profile that drives the system towards its low-energy overlapped configuration as well as local variation due to the atomic structure of the graphene. The lower insets are snapshots of the MD (left) and DFT (right) models. The side length L and offset L_0 are defined in the upper inset. All DFT calculations in this study were performed by Dr. Erin R. Johnson's group.

k_1 was estimated to be 0.01886 eV/Å^2 at the energy minimum and 0.01545 eV/Å^2 at the maximum by dividing the binding energy by the unit-cell area. We note that all these values are similar to those obtained experimentally for the interlayer binding energy of highly-oriented pyrolitic graphite, 0.011875 eV/Å^2 [4].Hence, k_1 is a constant in a range that spans a 5x4-cell double flake (∼1nm range), our MD simulations (∼10nm), experiment (∼2μm), and infinite contact areas. Model predictions shown next are obtained using k_1=0.0118 eV/Å^2.

The force on the flake is then

$$F = -\frac{dE}{dx}\frac{1}{L_0} + cL_0\frac{dx}{dt} \tag{2.2}$$

where the first term is the conservative force coming from the potential energy and the second term is dissipative and captures the effect of friction. Similar to previous formulations, the friction force is proportional to the sliding velocity [4]. Its magnitude is determined by the variable coefficient c, which will be related to the surface roughness. The equation of motion to be solved is

$$F = m\ddot{x} \tag{2.3}$$

with $m = \sigma A_0$, A_0 being the area of the flake and $\sigma = 4.6508$ amu/Å^2 the mass density of graphene. This analytical model will be used to extrapolate the motion patterns of graphene predicted by the MD simulation to understand experimental observations.

As a first test of the model, we consider the dependence of the maximum velocity of the flake with the mismatch ratio, x, shown in Figure 2.12(a). At larger mismatch, the flake is farther from its equilibrium position, so the maximum velocity is greater. MD simulations of flakes of different sizes give nearly identical maximum velocities for a given mismatch ratio. Since the model potential energy is linearly proportional to offset ratio, $E \propto x$, the model predicts a square-root relation between maximum velocity and mismatch that is in good agreement with the MD results ($E = \frac{1}{2}mv^2 \propto x$). We also analyze the variation of lateral force with offset during one oscillation period predicted by MD simulation and the model in Figure 2.12(b) and (c), respectively. The MD simulation and model (with appropriately chosen friction) give qualitatively similar results, again demonstrating that the simple model includes the forces necessary to describe the oscillatory motion of bilayer graphene.

In the MD simulations, the rate at which oscillatory motion decays is determined by the roughness of the graphene flakes (R_q). The analytical model decay rate is determined by the magnitude of the parameter c, which is the multiplicative prefactor of the friction term. The effects of R_q or c on the trajectory of the graphene flake are illustrated in Figure 2.13, where these parameters are varied such that the oscillatory motion patterns transition from very low damping (a and b), to moderately damped (c and d), and finally to highly damped (f). The consistency of the

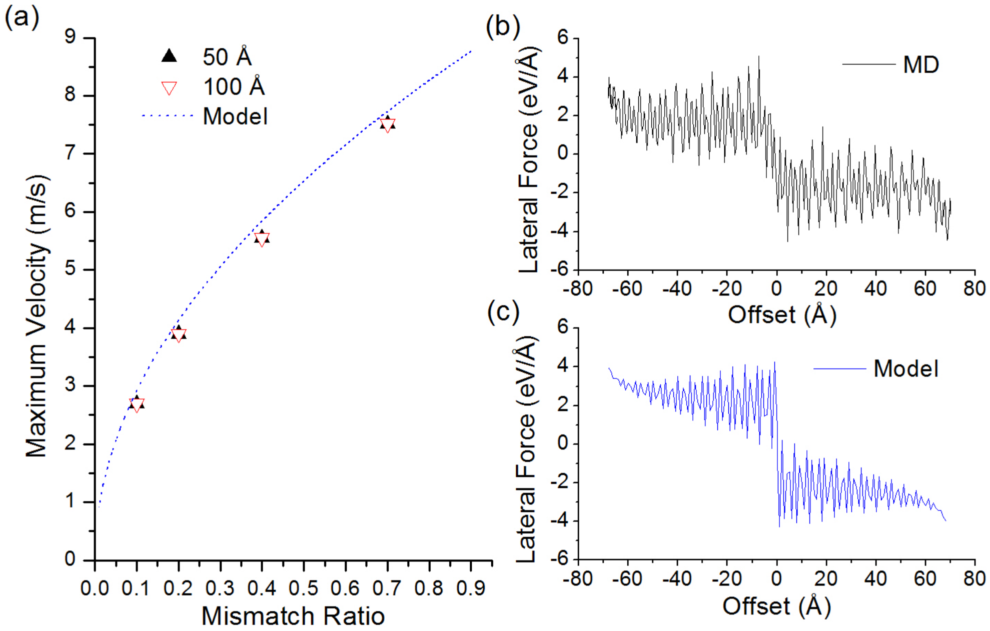

Figure 2.12: (a) Increase of maximum (initial) flake velocity with mismatch ratio predicted by the analytical model and by MD simulations of perfectly flat graphene having three different sizes. Variation of lateral force with offset position for 100 Å square graphene with an initial offset of 70 Å predicted by (b) an MD simulation of rough graphene (R_q=0.2 Å) and (c) the corresponding analytical model (c=0.01 eV×ps/Å^2).

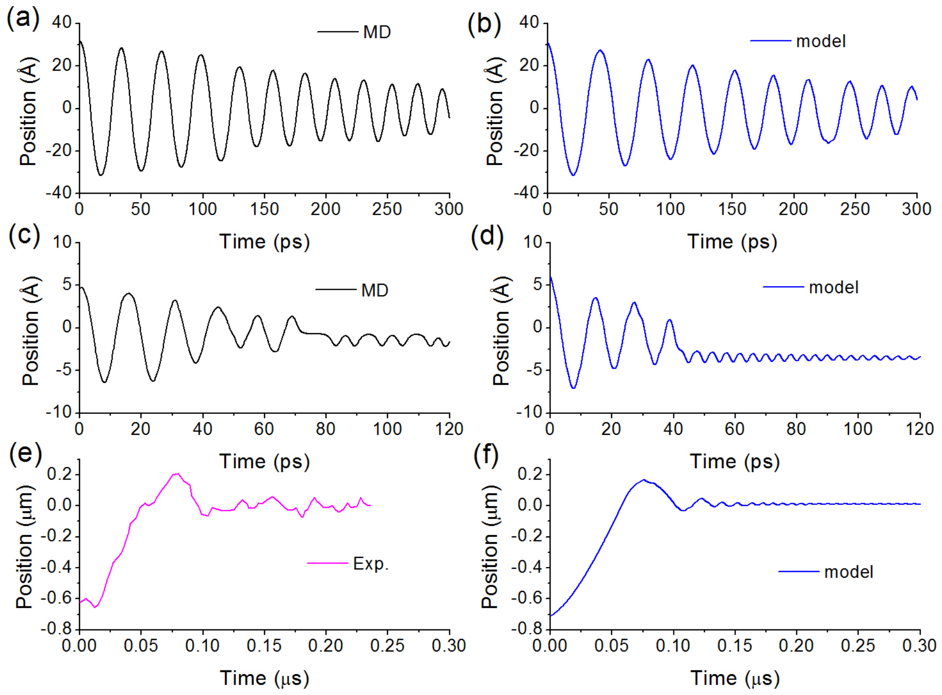

Figure 2.13: Decaying oscillatory motion of laterally-offset graphene. Low damping: (a) MD simulation with R_q=0.2 Å and (b) analytical model with c=0.01 eV×ps/Å^2, both for 100 Å square graphene with an initial offset of 30 Å. Moderate damping: (c) MD simulation with R_q=0.44 Å and (d) analytical model with c=0.04 eV×ps/Å^2, both for 100 Å square graphene with an initial offset of 30 Å. High damping: (e) experimental measurements from Ref. [4] and (f) the analytical model with c=0.25 eV×ps/Å^2, both for 3 μm square graphene with initial offset 70 Å.

MD simulation and analytical model predictions in (a) through (d) further validate the analytical approach we have presented. Consequently, we can now apply that model to make predictions about larger-scale systems that are not accessible at the atomic-scale of the MD simulation. This enables direct comparison of the model results to the previously-reported experimental data shown in Figure 2.13(e) [4]. In Figure 2.13(f), the magnitude of c is fit such that the motion predicted by the analytical model closely resembles that of the experiment.

Friction between sliding surfaces is well-known to be a function of the roughness of those surfaces. The MD simulations describe the oscillatory behavior of graphene with variable roughness, thereby providing a means of exploring the connection between roughness and damping. The magnitude of the maximum offset position decreases exponentially over time ($L_0 \exp(-\lambda t)$). The decay rate (λ in the preceding equation) can be calculated from results such as those in Figure 2.13(a). Figure 2.14 shows the variation of this decay rate with R_q. Although the range of roughnesses accessible to the simulation is rather small, the relationship between roughness and decay rate appears to be approximately linear.

In order to progress beyond the time and size scales accessible to MD, and directly compare with experiment, we turn to the analytical model. The decay rate predicted by the model also shows a linear dependence on the friction constant c, as shown in Figure 2.14. The experimental data in Figure 2.13(e) can be approximated by the model with constants ranging from c=0.19 to 0.25 eV×ps/Å^2. The resulting predictions correspond to decay rates from 0.015 to 0.023 ps^{-1}; this range is identified on Figure 2.14 as the shaded region. The size-scale limitations of MD preclude modeling surfaces with large roughness. However, linear extrapolation of the MD data to this range of decay rates reveals that they correspond to roughnesses between 2.75 and 4.2 Å, which is consistent with the roughness expected for graphene on a silicon dioxide substrate [118, 119].

Based on the linear relationships between decay rate and R_q and between decay rate at c, we infer there is a linear relationship between roughness and the friction constant. This leads to the expression c=0.068(eV×ps/Å) × R_q which provides a means of estimating the model friction constant for a given roughness. Therefore, for graphene of any roughness, the model presented here can be used to predict the corresponding oscillatory or self-retraction motion, bridging the gap between DFT, MD, and experiment.

2.3.4 Conclusion

In summary, we have presented a multiscale approach utilizing DFT calculations, MD simulation, and a reduced-order one-dimensional model to relate the experimental self-retraction behavior of graphene flakes to their surface roughness. Our DFT results provided accurate static energies, while the MD simulations predicted frictional sliding at the atomic level for variable roughness interfaces. The

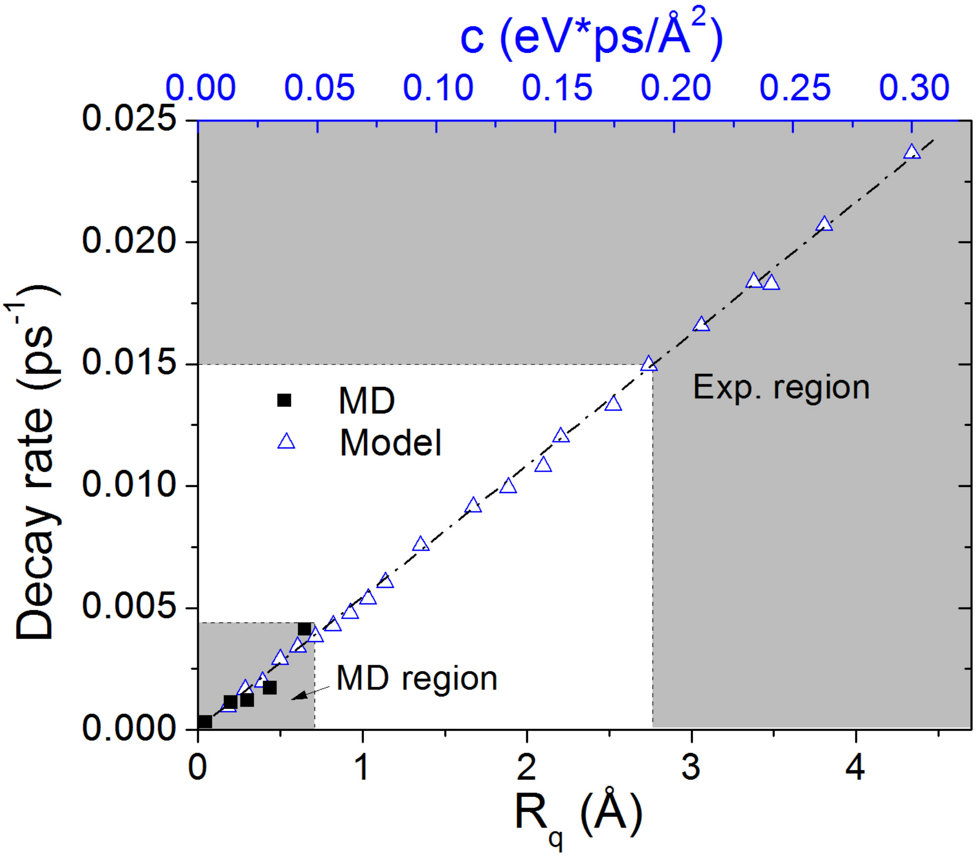

Figure 2.14: Decay rate increasing with roughness from MD (lower x-axis) and with the magnitude of friction c from the analytical model (upper x-axis); the dashed line represents a linear fit to both data sets. The lower shaded region identifies the range of roughnesses and corresponding decay rates accessible to an MD simulation while the upper shaded region represents the range of c values and corresponding decay rates for which the model predictions are comparable to the experimental data in Figure 2.13(e).

one-dimensional model was used to extrapolate MD results to the experimental time and size scales, quantitatively explaining the oscillatory motion of the graphene bilayer in terms of roughness. This work reveals atomic-scale mechanisms underlying the relationship between microscale motion and nanoscale roughness, and ultimately suggests a means of prescribing the oscillation or self-retraction of bilayer graphene by tuning its substrate-dependent roughness.

2.4 Oscillatory Motion in 2D Materials

2.4.1 Introduction

Two-dimensional materials, such as graphene, boron nitride (BN), and molybdenum disulfide (MoS_2), have been at the forefront of scientific interest in recent years. Such materials are promising for a variety of applications due to their unique physical, electrical, and chemical properties [120, 121]. An interesting behavior, recently observed in multilayer graphene, is self-retraction and oscillation [4, 109, 112]. These phenomena are observed when the topmost graphene layer is offset laterally relative to those below it; when the layer is released, it slides back, retracting towards its original, overlapping position.

The mechanisms underlying graphene oscillation and self-retraction have been investigated extensively, both experimentally [4, 109, 112] and computationally [110, 111, 113–116]. In general, this behavior is explained by the conversion of potential energy of the offset configuration to kinetic energy that drives the system towards its energetically-stable overlapping configuration. The dynamics of the motion have been found to be determined by factors that affect the potential energy gradient, including commensurability [113, 115] and temperature [4], and also by factors that affect energy dissipation (or damping) such as surface roughness [116].

All previous work on oscillation and self-retraction has focused on graphene. However, since these phenomena are enabled by the ordered crystallographic layers and the weak interactions between them, it could, in principle, be observable in any material with a similar layered structure. In this article, we explore this possibility by generalizing our previous study [116] to other layered materials, with particular emphasis on boron nitride and molybdenum disulfide. A multi-scale approach, combining MD simulations and DFT calulations is employed to investigate the oscillatory motion of laterally-offset bilayer graphene, BN, and MoS_2, with variable surface roughness. All DFT calculations in this study were performed by Dr. Erin R. Johnson's group. Additionally, simulations are performed with modified inter-layer interaction parameters to study the interplay between surface energetics, surface geometry, friction, and oscillation behavior. We find that, given a small number of parameters that can be obtained computationally, our reduced-order model can be used to predict experimental self-retraction and oscillation behavior for any layered material, as well as the effect changes in the interlayer contact (stress-induced corrugation, roughness, impurities, etc.) will have on these phenomena.

2.4.2 Methods

The MD simulations consisted of two square layers of graphene, BN, and MoS_2 with side length $L_0 = 10$ nm, illustrated in Figure 2.15 (a), (c) and (e). The top layer was initially offset relative to the bottom by a distance $L = 7$ nm. The atoms at the two ends of the layers in the offset direction were treated as rigid bodies. In order to examine the effect of roughness, the root-mean-square (R_q) roughness of

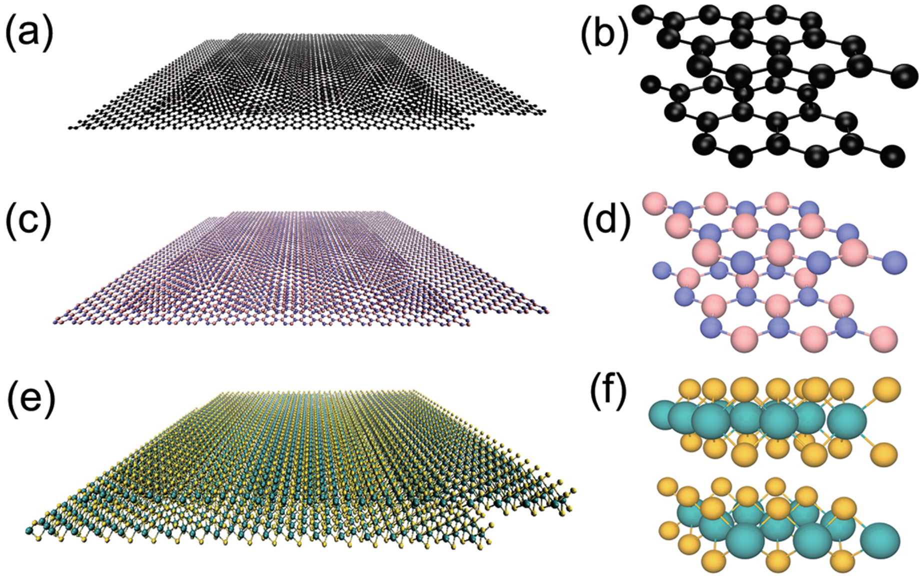

Figure 2.15: Models of bilayer (a) graphene, (c) BN, and (e) MoS_2 layers. The structures of these materials are shown in greater detail in the right-hand panels (b, d, and f).

Table 2.1: LJ parameters used in the MD simulations for all atomic pairs.

Atom Pair	ε_0 (meV)	σ (Å)	Ref.
C-C	2.84	3.40	[84]
B-B	4.116	3.45	[125]
N-N	6.281	3.365	[125]
B-N	5.085	3.41	[125]
Mo-Mo	0.585	4.20	[123, 124]
S-S	13.86	3.13	[123, 124]
Mo-S	2.8	3.66	[123, 124]

the graphene and BN was varied from 0 to 0.7 Å using the same compression method as in our previous paper [116]. All simulations were performed using the LAMMPS software [105], with a Langevin thermostat applied to maintain a temperature of 300K.

The inter-atomic interactions for graphene, BN and MoS_2 were described using the AIREBO potential [84], the Tersoff potential [122], and the Reactive Empirical Bond Order (REBO) potential [123], respectively. The long range interactions between layers were modeled using a LJ potential

$$V = 4\varepsilon\left[\left(\frac{\sigma}{r}\right)^{12} - \left(\frac{\sigma}{r}\right)^{6}\right] \tag{2.4}$$

where ε is the well depth and σ is the inter-atomic distance at which the potential energy crosses zero. The parameters in this model were obtained from references [84, 123–125] and are summarized in Table 2.1. The potential energy barrier for interlayer sliding depends on both ε and σ, but the equilibrium interlayer distance depends only on σ. Both should affect relative motion between layers. Therefore, additional simulations were performed with the LJ parameters scaled relative to their original values, i.e. $\varepsilon = m\varepsilon_0$, with $m = 0.5$, 1, 1.3, 1.6, 1.8, 2 and 2.2, and $\sigma = n\sigma_0$, with $n = 0.5$, 1 and 2.

DFT calculations were performed by Dr. Erin R. Johnson's group. The details about model used in the DFT calculations can be found in our paper [126].

2.4.3 Results and Discussion

Ideally Flat layers

Figure 2.16(a,c,e) shows the two-dimensional potential-energy surfaces for sliding calculated using DFT. The minimum-energy configuration of graphene has the carbon atoms staggered, while the minima for BN and MoS_2 correspond to a situation with maximum overlap of unlike atoms: B over N and S over Mo. The

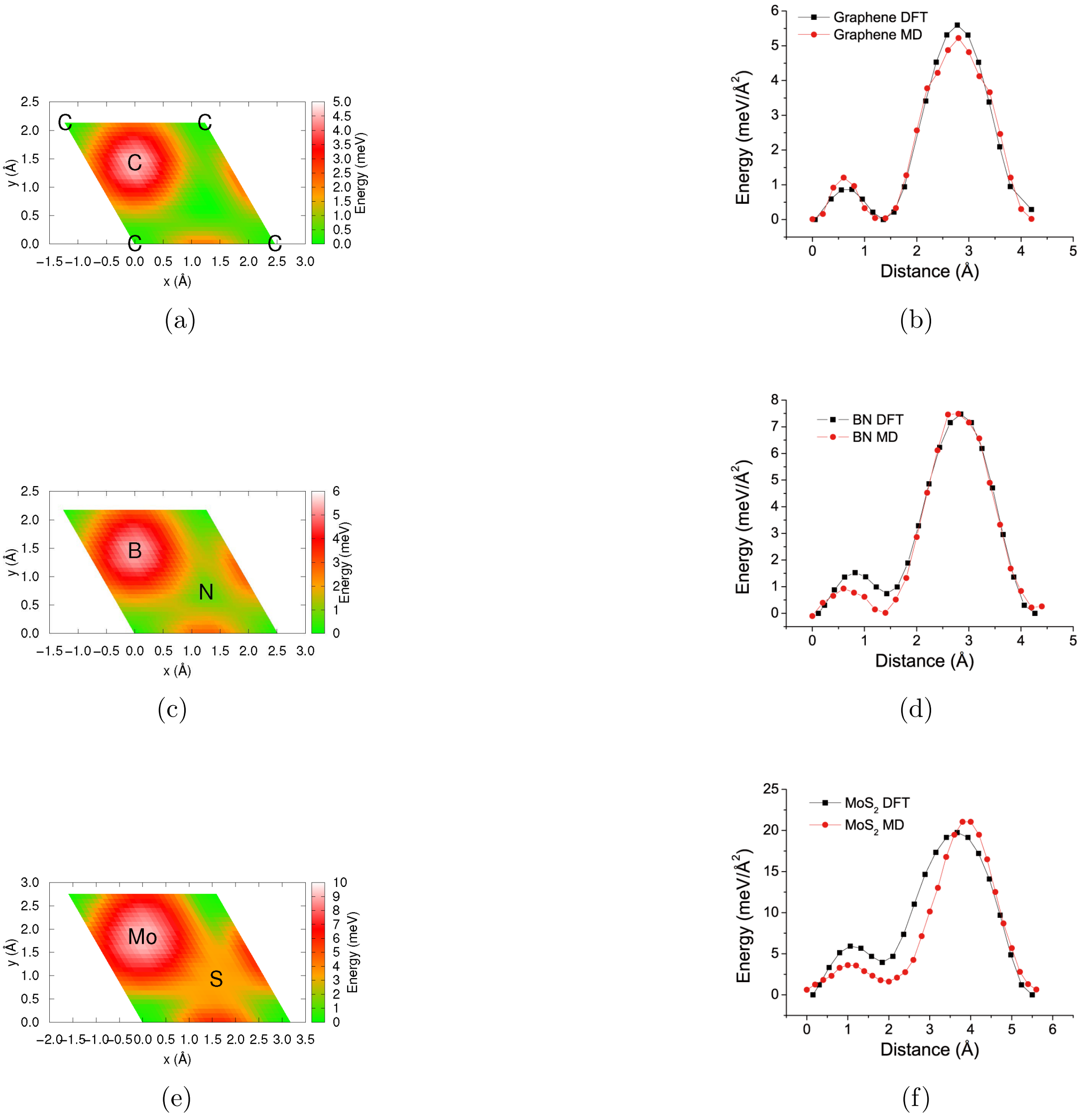

(a) (b)

(c) (d)

(e) (f)

Figure 2.16: DFT potential energy surfaces for relative layer sliding in bilayer (a) graphene, (c) BN, and (e) MoS$_2$, in meV per unit cell. The atom labels on the color maps represent the bottom layer and the origin of the plot corresponds to the energy minimum. A comparison between the DFT and MD inter-layer interaction energy per unit area in the (111)-direction (i.e. the longer diagonal of the left panels) is also shown for (b) graphene, (d) BN, and (f) MoS$_2$. All DFT calculations in this study were performed by Dr. Erin R. Johnson's group.

binding energies per atom are 24.78 (graphene), 27.68 (BN), and 39.46 (MoS_2) meV. The dispersion contributions to these are 31.98, 35.22, and 48.18 meV, respectively, indicating that dispersion interactions are dominant in inter-layer binding. The potential energy surface and the binding energy of BN are similar to graphene, which is no surprise given their similar structures and polarizabilities.

The energy per unit area along the long diagonal of the contour plots is shown in Figure 2.16(b,d,f). The maximum energy per area (energy barrier) of MoS_2 is more than three times greater than that of graphene or BN. This may be explained by the corrugated nature of the MoS_2 surface, which increases both the dispersion binding and the energy barriers, and also by the sulfur anions being more polarizable than the first-row atoms in graphene and BN. Also shown on these figures is the energy per area predicted by the empirical potentials used in the MD simulations. Comparison to the DFT reference data reveals that there is excellent agreement for all three materials, indicating that the MD simulations are able to capture the inter-layer energetics accurately.

Molecular dynamics simulations were first used to characterize the dynamic response of the laterally-offset materials for ideally flat layers (i.e. no externally-imposed surface roughness). Figure 2.17(a,b,c) shows the oscillatory and self-retraction motion of laterally-offset graphene, BN and MoS_2. The graphene and BN layers exhibit oscillatory motion while MoS_2 retracts to the maximally-overlapping position without oscillation. Since all three materials are ideally flat, and the commensurability and temperature conditions are the same, the observed difference in the MoS_2 dynamics is attributed to the large energy barrier (see Figure 2.16) arising from the corrugated nature of the surface. A higher energy barrier is associated with more resistance to sliding (greater friction), which can in turn be expected to damp the oscillations more quickly. This suggests that self-retraction and oscillation behavior is affected by the inherent resistance of the material to sliding (as measured by the static energy barriers), as well as external factors (e.g. temperature, roughness) as reported previously [4,116]. While maximizing dispersion binding provides a driving force for self-retraction for all layered materials, small sliding barriers are needed to observe oscillation.

To further analyze the effect of the potential energy barriers on the dynamics, we varied the inter-layer interaction strength by changing the depth of the potential well (ε) in the LJ potential for each material in the MD simulations. The results are shown in Figure 2.17. MoS_2 exhibits self-retraction, i.e. the motion is overdamped, for all potential well depths studied. However, for BN and graphene, increasing the interaction strength increases the rate at which the oscillation amplitude decreases over time. This effect is quantified in terms of the decay rate obtained by fitting the maximum position versus time data to an exponential expression. Figure 2.17d shows that the decay rate is faster for stronger interactions, depending exponentially on the barrier.

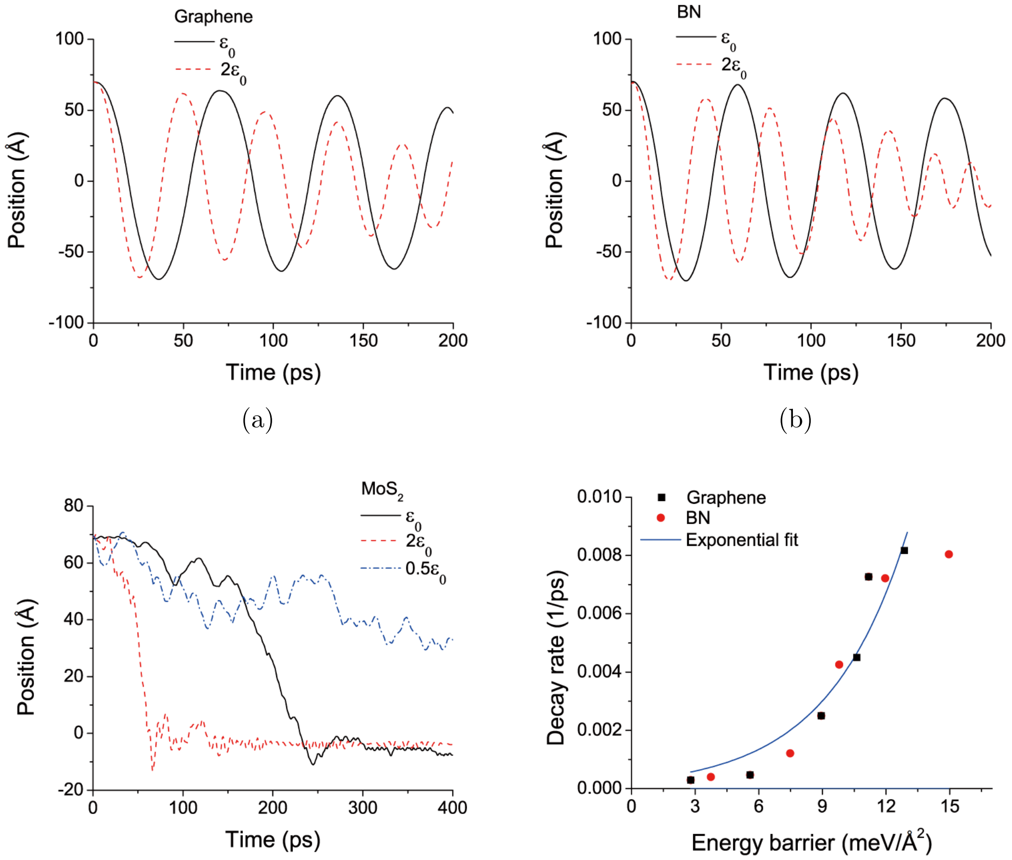

(a) (b) (c) (d)

Figure 2.17: MD-predicted oscillatory and self-retraction motion of laterally-offset (a) graphene, (b) BN, and (c) MoS_2 with variable energy barriers controlled by changing the LJ parameter ε. For MoS_2 with $\varepsilon = 0.5\varepsilon_0$, the displaced layer does not retract to the initial, maximally-overlapping position. (d) Decay rate as a function of energy barrier for graphene and BN; the data is fit to an exponential function $y(x) = ae^{bx}$ with prefactor $a = 2.522 \times 10^{-4}$ and $b = 0.2766$.

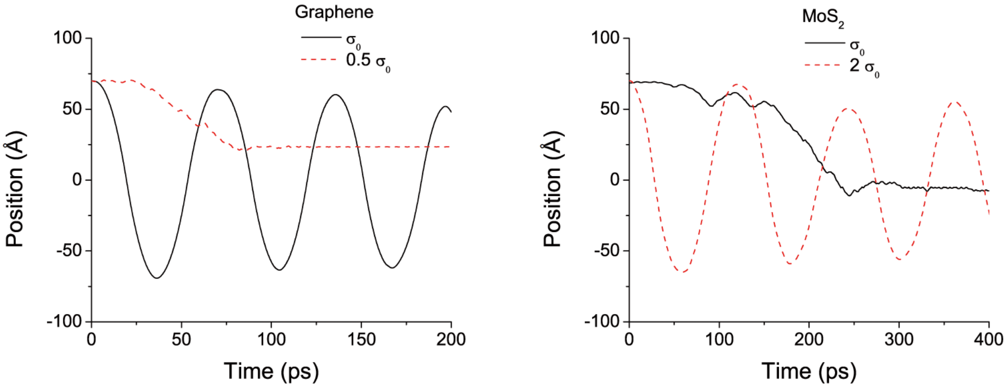

(a) (b)

Figure 2.18: MD-predicted oscillatory and self-retraction motion of laterally-offset (a) graphene and (b) MoS_2 with variable energy barriers controlled by changing the LJ parameter σ. For graphene with $0.5\sigma_0$, the displaced layer does not retract to the initial, maximally-overlapping position.

We also considered the dependence of the motion on the σ parameter. While modifying the LJ ε parameter changes only the energy barrier, modifying σ affects both the equilibrium inter-layer distance (i.e. the layer corrugation) and the energy barrier. Illustrative results for graphene and MoS_2 are shown in Figure 2.18. For MoS_2, doubling σ, which increases the interlayer distance, results in the onset of oscillatory motion. The minimum-energy separation between layers becomes larger relative to the intra-layer atomic distances, making the interlayer contact less corrugated. This facilitates sliding because both the energy barrier is smaller and the corrugated nature of the surface impedes the relative motion of the layers, similar to the effect of roughness-induced friction. For graphene, which shows oscillatory motion with the original LJ parameters, we decreased σ by half. As shown in Figure 2.18, instead of oscillating, the upper flake became trapped in a local minimum on the potential-energy surface, which is similar to the behavior seen for MoS_2 with $0.5\epsilon_0$ in Figure 2.17c. This occurs because, with decreased interlayer distance, the sliding barrier is so high that it cannot be surmounted and the upper layer cannot retract back to the minimum-energy position. Therefore, changing the potential-energy surface can qualitatively alter the self-retraction/oscillation behavior. In particular, a relatively flat (i.e. uncorrugated) surface with low energy barriers seems to be a necessary condition in order to observe oscillation.

Roughness and a Reduced-Order Model

Our previous study showed that the decay rate of the oscillatory motion of graphene increases linearly with imposed surface roughness and a reduced-order model was developed to describe that motion [116]. The model is briefly reviewed here. The potential energy, E, as a function of the dimensionless offset ratio $x = L/L_0$, is written as

$$E = k_1 A_0 |x| - k_2 A_0 (1 - |x|) \cos\left(\frac{2\pi L_0 x}{p}\right). \tag{2.5}$$

The force can be obtained as

$$F = -\frac{dE}{dx}\frac{1}{L_0} + cL_0\frac{dx}{dt} \tag{2.6}$$

and the dynamics can be described by solving equation of motion:

$$F = m\ddot{x}. \tag{2.7}$$

In these expressions, A_0 is the area (in this case L_0^2), k_1 is the binding energy per contact area, k_2 is the amplitude of the oscillatory energy profile, p is the periodicity of the material structure, and c is a coefficient related to the roughness, which controls the friction. Increasing roughness increases friction which, in turn, linearly increases the decay rate of the oscillations [116].

We now examine the effect of increasing roughness on the self-retraction motion of both graphene and BN (since MoS_2 does not oscillate even for the ideally-flat layers, we do not expect any change in this behavior by increasing the roughness). The results in Figure 2.19 show that graphene and BN each exhibit a linear relationship between decay rate and roughness with similar slopes, but BN has a slightly higher decay rate at zero roughness, likely reflecting the larger energy barrier (Figure 2.16b,d). We also considered the effect of roughness on the decay rate for graphene and BN with the interaction strengths and sliding barriers artificially increased by taking $\varepsilon = 2\varepsilon_0$. The results show that the linear relationship is retained and increasing the interaction strength causes an effectively constant shift in the decay rate to higher values. This suggests that oscillatory motion is affected by both the potential energy barriers (intercept) and the roughness (slope), at least for materials with a structure similar to graphene.

To describe these observations, the reduced-order model presented in our previous paper [116] must be generalized. In our previous work, we observed that c depends linearly on the decay rate and then fit the dissipative friction coefficient c using the linear increase in decay rate with roughness predicted by the MD simulations. However, we observe in Figure 2.19 that there is a finite decay rate, even for ideally flat surfaces, which is associated with the surface structure and energy barriers, as discussed in the preceding section. To capture the effects of both roughness

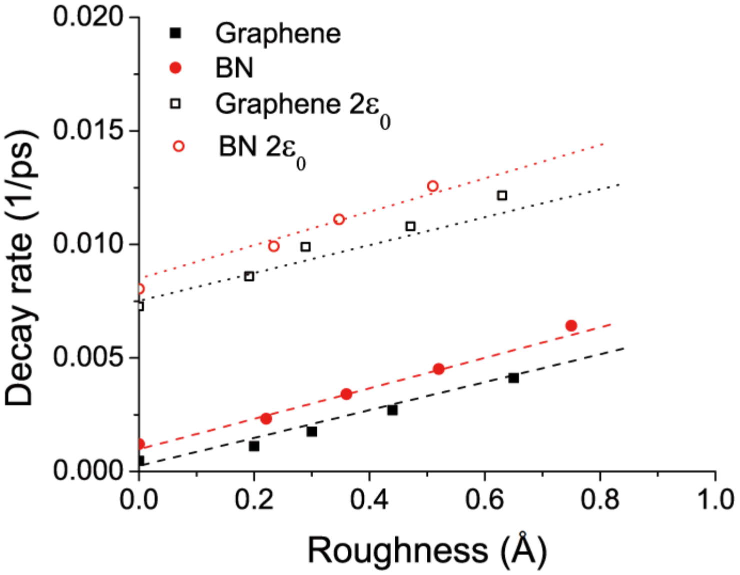

Figure 2.19: Decay rate as a function of roughness from MD simulations for graphene and BN with the original and artificially-increased LJ interaction strength.

Table 2.2: Reduced-order model coefficients A and B for graphene and BN with physical (first row) and artificially-increased ($2\times\varepsilon_0$, second row) interaction strengths.

Material	Energy barrier (meV/Å^2)	A (eV ps/Å^3)	B (eV ps/Å^2)
Graphene	5.59	0.087±0.007	0.003±0.003
	11.18	0.109±0.008	0.103±0.004
BN	7.48	0.099±0.006	0.014±0.002
	14.96	0.126±0.004	0.110±0.001

and energy barrier on the motion, the definition of the coefficient, c, must be made more flexible. We now propose that this coefficient have the general form

$$c = AR_q + B \tag{2.8}$$

where A and B are determined by the slope and intercept of the decay-rate versus roughness plot (Figure 2.19), and account for the effects of imposed roughness and energy, respectively.

The A and B parameters, as well as k_1 and k_2, can be obtained from static DFT and MD data. In this work, the surface energy, k_1, was obtained from periodic DFT calculations and found to be 0.01888 eV/Å^2 (24.78 meV/atom) for graphene and 0.02030 eV/Å^2 (27.68 meV/atom) for BN. The value of k_2 was calculated as the amplitude of the oscillatory energy profile that results from subtracting a V-shaped curve (given by $k_1 A_0 |x|$) from the MD potential energy versus the mismatch ratio. From our MD simulations, k_2 was calculated to be 2.5×10^{-4} eV/Å and 3.2×10^{-4} eV/Å for graphene and BN, respectively.

Table 2.2 shows the values of A and B obtained from linear fits to the MD data for graphene and BN with original and artificially-increased inter-layer interaction strengths. The differences between all values of A (the slopes in Figure 2.19) are on the same order as the standard error of the linear fit, indicating that the relationship between imposed roughness and decay rate is nearly independent of the material and sliding energetics. This contrasts with the B parameter that depends strongly on both material and interaction strength, and corresponds to the decay rate for ideally flat surfaces. We showed in Figure 2.17d that the decay rate increases exponentially with the energy barrier. Hence, the coefficient c in Equation 2.6 depends linearly on the roughness (with slope A) and exponentially on the energy barrier (through B), and these two effects are independent of each other.

The generalized analytical model can, in principle, be used to predict offset-driven motion for any material with any roughness. For example, Figure 2.20

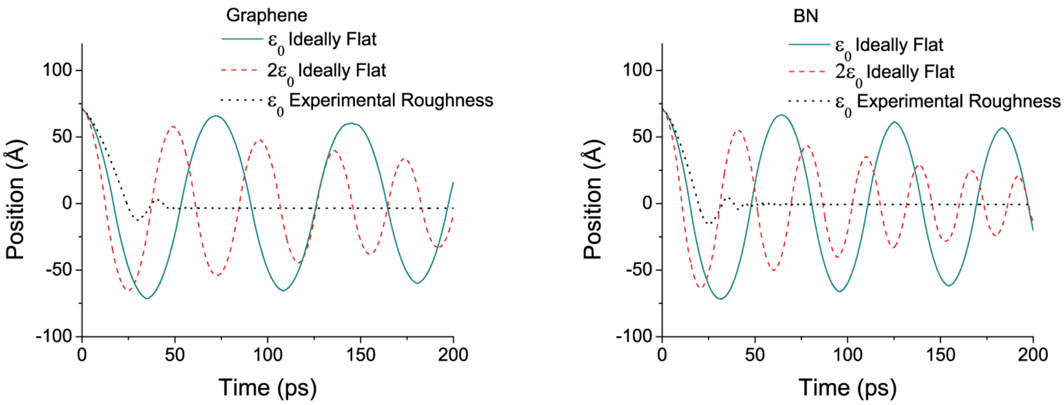

Figure 2.20: Oscillation behavior of graphene (left) and BN (right) predicted by the reduced-order model with different interaction strengths and roughnesses.

shows the predicted oscillation behavior of graphene and BN with the original and artificially-increased interaction strengths, which are consistent with the results obtained from the MD simulations. However, the more useful feature of the model is its ability to predict offset-driven motion for cases where MD simulations are not possible. For example, the roughness that can be imposed in MD is limited by the tractable simulation size and is typically smaller than roughnesses measured experimentally. However, the reduced-order model can be used to extrapolate the behavior of graphene and BN to experimental roughness values in order to predict the self-retraction dynamics of real materials. Figure 2.20 also shows the oscillation behavior predicted by our model extrapolated to a roughness of 5Å, which is consistent with the range of experimentally-measured roughnesses of graphene [119] and BN [127]. For both BN and graphene, the predicted behavior is oscillatory but heavily damped, with at most one observable oscillation. This result is consistent with the previously-reported experiments on graphene [4, 109, 112].

Our simple reduced-order model appears to capture the energetics- and roughness-dependent oscillation behavior of BN and graphene accurately. In the case of MoS_2, the overdamped behavior of the ideally-flat system at any interaction strength (Figure 2.16c) prevents calculation of the decay rate and, consequently, the A and B parameters for this material. The value of B is likely one or more orders of magnitude higher than those for graphene and BN. It is important to note that the energy barrier for MoS_2 is only three times larger than those of graphene and BN, which means that this is not the only factor contributing to B, and that the layer geometry (and in particular its corrugation, as illustrated in Figure 2.15f) also affects this coefficient. Nevertheless, since the decay rate always increases with roughness, we do not expect this material (or others with similarly-corrugated layers) to present oscillation experimentally in any case.

2.4.4 Conclusion

Oscillation and self-retraction of laterally-offset layers has been observed experimentally for graphene. In a previous article, we explained the oscillatory behavior and its damping mechanisms by inter-layer friction as determined by imposed roughness. Given the potentially-relevant technological implications of this phenomenon, in this article, we extend the study to the self-retraction and oscillation behavior of generalized layered materials, with particular emphasis on graphene, boron nitride, and molybdenum sulfide. A multi-scale approach utilizing density-functional theory, molecular dynamics simulation, and an extension of our previously-proposed reduced-order one-dimensional model is used.

We predict that flat layers of BN will exhibit heavily-damped oscillatory motion, very similar to that observed for graphene, on the experimental size-scale. For MoS_2, only self-retraction motion and no oscillation is predicted due to the inherent roughness (corrugation) of its surface. For graphene and BN, the decay rate of the oscillatory motion is linearly dependent on the imposed surface roughness and increases exponentially with the potential energy barrier for sliding. In general, both relatively-flat surfaces and low potential-energy barriers for sliding are necessary for a layered material to exhibit oscillatory self-retraction.

A generalization of our reduced-order one-dimensional model is proposed that can be applied to quantitatively explain the experimental oscillatory and self-retraction motion of layered materials. The model contains parameters that can be easily derived computationally. Tuning the substrate-dependent roughness of layered materials (e.g. by applied stress, impurities, etc.) like graphene and BN, guided by the model, could ultimately be useful in the design of nano-scale oscillators for device applications.

2.5 Frictional Anisotropy on Quasicrystal Approximant Surfaces

2.5.1 Introduction

A quasicrystal is a structure that is ordered but not periodic, which contains a quasicrystalline pattern filling all available space, but lacking translational symmetry. Quasicrystals usually exhibit very low friction which is important for variety of applications, e.g. nonstick coating for cooking utensils, surgery tolls, razor blades. However, the low friction between quasicrystal surfaces and a contacting probe remains a puzzle [128]. Most of the proposed and realized applications of quasicrystals have taken advantage of this low friction [129–133]. Anomalously low friction has been reported at length scales ranging from atomic probes to engineering pin-on-disk experiments, in air and in vacuum, and at such low normal forces as to avoid any surface damage, even at the atomic scale, as well as in ploughing experiments [134]. Quasicrystals exhibit lower friction than related periodic phases, called approximants, of similar chemical composition [134,135], suggesting but not proving that more than surface chemistry is involved. At the same time, the lack of periodicity in quasicrystals makes them hard, and low friction could be a consequence of hardness [136–140]. A 2005 experiment by Park *et al.* sought to dispense with all such surface-dependent effects by measuring the friction between a thiol-passivated AFM probe and a two-fold surface of a decagonal AlNiCo quasicrystal [141]. On this surface, one direction is periodic, the other quasiperiodic. That surface damage was averted through the intervening thiol was demonstrated by STM imaging before and after the friction measurements. The experiment, in ultra-high vacuum, found an eight-fold anisotropy in the magnitude of sliding friction.

Such a large surface anisotropy was virtually unknown in atomic-scale measurements; a recent review of theories of quasicrystal friction dubbed it the “giant frictional-anisotropy effect” [128]. Filippov *et al.*, the first to attack the problem computationally, reported reproducing the experimental anisotropy in a Langevin model in which mean feature spacings differed in the periodic and quasiperiodic directions; the quasiperiodicity itself was not relevant [142–144]. However, three of us, using the same methods, found that small changes in the parameters could change the sense of the anisotropy and argued, moreover, that Filippov’s parameters did not correspond to scanning tunneling microscope (STM) images of the experimental surface [145].

Other plausible explanations include entrainment of the thiol chains passivating the AFM tip and the difficulty of either exciting or propagating phonon or electronic modes. In such a complex system, it would not be surprising if each of these mechanisms played a role; on the other hand, the generic result of low friction in different quasicrystalline materials under different circumstances suggests a generic mechanism tied to quasicrystallinity. Controversy over the frictional anisotropy on d-AlNiCo echoes controversy over the various contributions to atomic-scale friction on other surfaces that do not combine periodic and quasiperiodic order [146–149].

By testing each of the proposed mechanisms (except electronic), MD simulation on d-AlNiCo may provide clues to the nature of atomic-scale friction generally [150], and that is the purpose of the current paper [1].

2.5.2 Methods

Perhaps the only simple aspect of the surfaces of quasicrystals is that they appear to reflect the underlying bulk structures without reconstruction [151]. While these materials exhibit a high degree of long-range positional order, as demonstrated in Fourier space by very sharp diffraction peaks [152], they do so without periodicity; in one sense, their unit cells are infinite. As a consequence, only a few bulk structures have been proposed at a level permitting comparison to experiment [153]. This poses a particular challenge to the simulation of atomic-scale friction on quasicrystal surfaces. However, quasicrystalline approximants contain local symmetries and structural motifs similar to those of their quasicrystalline counterparts [154] and are more suitable for MD simulations because of their periodicity.

In this work, H1 d-AlCoNi approximants with a unit cell of 25 atoms supplied by Widom were used [155]. These crystal structures were repeated in space to create model substrates. The apex of an AFM tip was then introduced into the models to enable simulations of sliding friction. The size and sliding surface of the approximant sample and the size, shape, and material of the tip were varied. The tip was subjected to a normal load and slid across the substrate surface in two orthogonal directions, corresponding to periodicity and (approximate) quasiperiodicity on the sample surface. Friction was then calculated as the time average of the lateral force resisting that sliding. In all cases, temperature was controlled using a Langevin thermostat, and the simulations were run using the LAMMPS simulation software [105]. In what follows, references to the “quasiperiodic” direction are intended in the sense of an approximant, thus referring to the larger of the two periodicities.

New parameters to describe Al-Co-Ni alloys, compounds and mixtures for the Embedded Atom Method (EAM) [156] were recently made available via the NIST Interatomic Potentials Repository Project [157] based on the binary Ni-Al potential [158] and elemental Co potential [159]. We used this model to describe the interactions within the H1-approximant sample. The Al model tip was also obtained by cutting atoms from the original slab into a 2 nm radius hemisphere. The uppermost atoms of the tip were treated as a rigid body and pulled along the substrate at 5 m/s by a virtual atom connected via a harmonic spring with spring constant 16 N/m. This model is illustrated in Fig. 2.21(a). The bottom-most layers of atoms in the substrate were fixed. All unconstrained atoms in the system were coupled to a Langevin thermostat in the two directions orthogonal to sliding with a target temperature of 300K.

---

[1] This section appeared in slightly different form as Zhijiang Ye, Ashlie Martini, Patricia Thiel, Heather H. Lovelady, Keith McLaughlin, and David A. Rabson, “Atomistic simulation of frictional anisotropy on quasicrystal approximant surfaces”, Phys. Rev. B (2016) under review. It is reproduced here by permission of the other authors.

We also constructed another model of thiol-passivated TiN tip to mimic that used in experiments. The model system is illustrated in Fig. 2.21(b). We first created models of a block of TiN (40×10×40 Å) and 20 thiol molecules using Accelrys Materials Studio. Then, we transferred the structures into LAMMPS and artificially increased the interaction strength between the bottom surface atoms of the TiN tip and the carbon atom at one end of each thiol molecule so that one end of the thiol molecules was attached to the TiN bottom surface after equilibration. The TiN slab was subsequently treated as a rigid body. The Polymer Consistent Force Field (PCFF) was used to describe bond, angle, torsion, and out-of-plane interactions between all tip (TiN and thiol) atoms, the EAM potential was again used to describe the inter-atomic interactions between substrate atoms, and the Lennard-Jones (LJ) potential was used to model the long-range interactions between tip and substrate with parameters obtained using standard mixing rules. All other simulation parameters and conditions were the same as described for the hemispherical Al tip model.

2.5.3 Results

Fig. 2.22 shows the average friction of the hemispherical tip sliding on the H1-approximant substrate at different loads. We observed that, while the simulation captures frictional anisotropy, it is the opposite direction of that observed in experiments, *i.e.*, friction is smaller in the periodic direction. In addition, we observed significant substrate wear, even at moderate loads, so could not run the simulation at loads larger than ∼6 nN.

The observation of wear from a bare tip is actually consistent with experimental observation and is also the reason that the experiments used a TiN tip passivated with hexadecane thiol [141, 160, 161], eliminating wear, as verified by STM imaging before and after. To capture this in the simulation,

Fig. 2.23 shows the average friction of the thiol passivated TiN tip sliding on the H1-approximant substrate at different loads. We observed higher friction in the periodic direction than the quasiperiodic direction, consistent with the trend observed in experiments. The magnitude of the friction and friction coefficient were also roughly comparable to the experiments, although the anisotropy was much smaller. In this case, we did not observe any noticeable wear on the surface, confirming that the thiol molecules indeed contributed to reducing wear.

Since frictional measurements are noisy, verifying the anisotropy in Fig. 2.23 requires an analysis of the uncertainties. Fig. 2.24 shows a sample run at 80 nN load in the quasiperiodic direction: the noise is large compared to the time-averaged

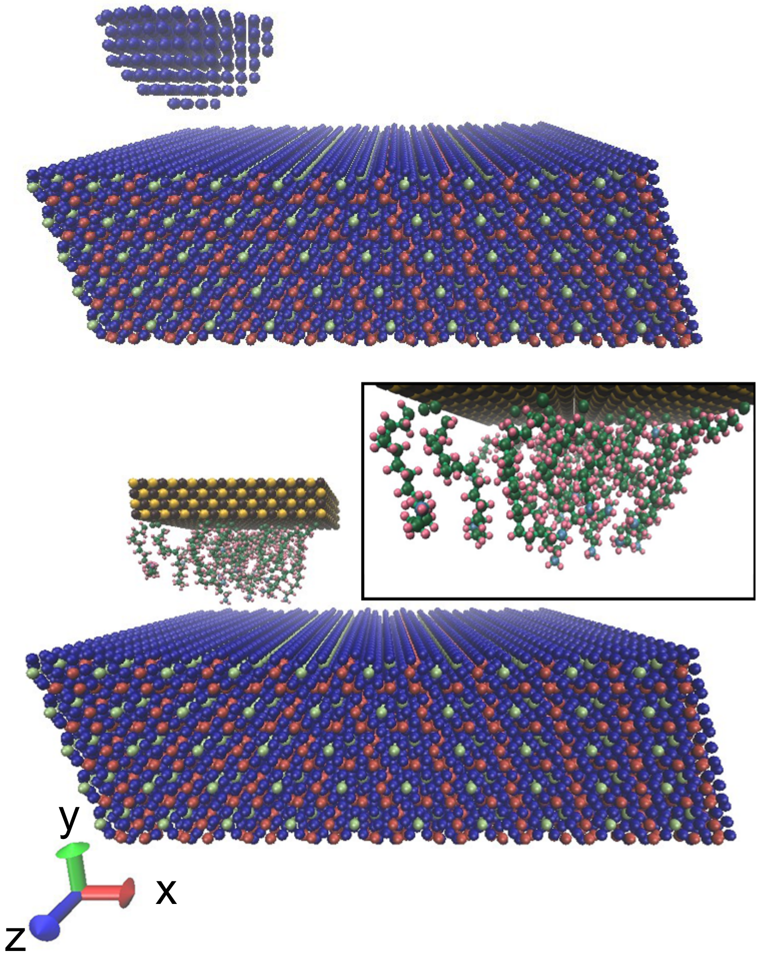

Figure 2.21: MD models of a hemispherical tip (upper image) and a thiol-passivated TiN tip (lower image and inset) sliding on d-AlCoNi substrate. Spheres represent atom positions where colors correspond to different elements: yellow - Ti, black - N, dark green - C, light blue - S, pink - H, red - Co, green - Ni, blue - Al.

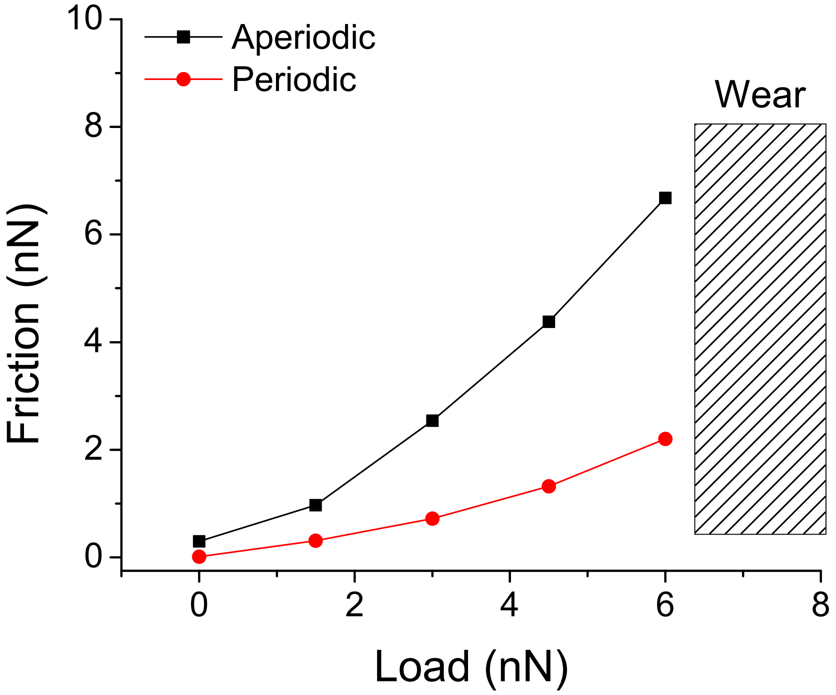

Figure 2.22: Average friction force increasing with load for a hemispherical aluminum tip sliding on an H1 approximant substrate. Friction magnitude is reasonable, but the frictional anisotropy is opposite to that observed in previous experiments. Wear was observed at even moderate loads precluding characterization of friction above $\sim$ 6 nN.

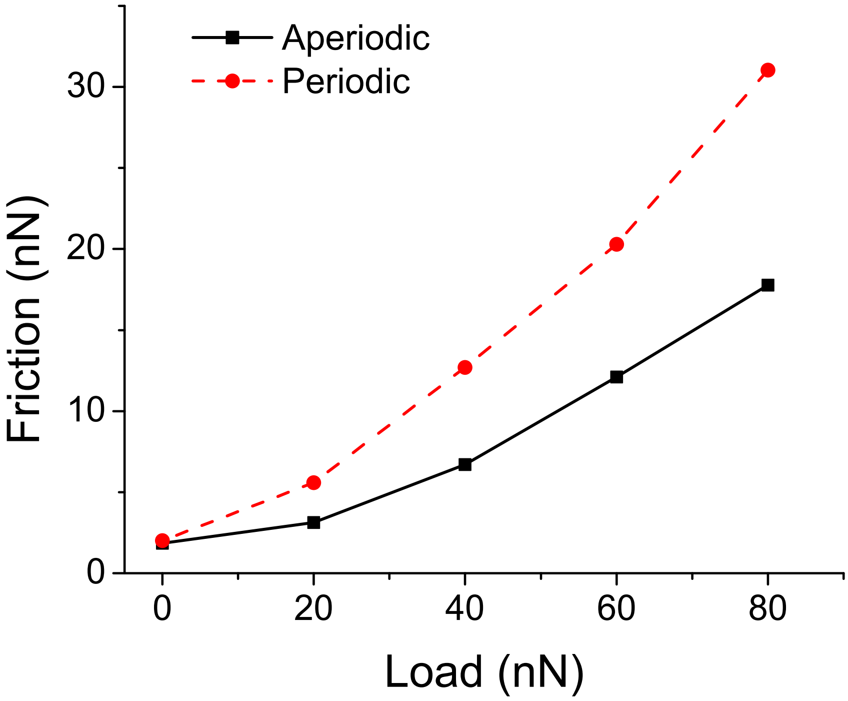

Figure 2.23: Average friction force increasing with load for a thiol-passivated TiN tip sliding on the H1 approximant substrate. No surface wear is observed, and both the magnitude and the anisotropy of the friction are roughly consistent with experiment.

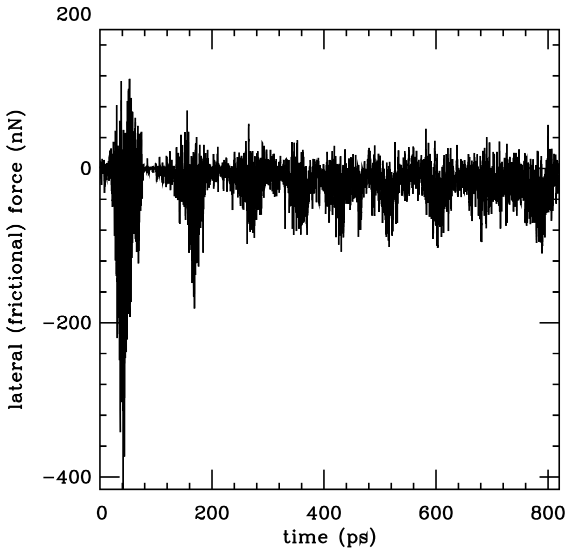

Figure 2.24: Sample run from Fig. 2.23 for the quasiperiodic direction at 80 nN load. The time series is noisy, but the pseudoperiod of ∼ 82–98 ps enables us to estimate error bars of smaller than 1.5 nN to the average negative lateral force of 18.7 nN. (The first 400 ps are excluded in computing the average.)

friction. A pseudo-period of ∼ 98 ps, possibly reminiscent of stick-slip friction, is evident in the time series; a similar pseudo-periodicity was observed in the periodic direction. Although experimentally stick-slip has been reported absent or suppressed at low loads in true quasicrystals [135,160,162], we would still expect it in this low-order approximant. A power-spectral estimate shows a broad peak closer to 82 ps than 98 ps, and we shall use this periodicity in estimating error bars. At the sliding speed of 5 m/s, this periodicity also corresponds closely to the approximant unit-cell size of 4.03 Å, although in other runs, there were differences between the stick-slip-like pseudo-periodicity and corresponding unit-cell dimension as large as 20%.

The figure suggests initial transient behavior that subsides by 300 ps. In these runs, we averaged only data past 400 ps. Table 2.3 presents the mean friction values with error bars. To estimate error bars, we collected the data past 400 ps into N bins each of duration equal to the pseudo-period so that the mean friction in each bin is considered an independent measurement. The error bars are then estimated as a sample standard deviation of the bins divided by $\sqrt{N}$. Since the pseudo-periods are themselves uncertain, we compared the means and estimated error bars for pseudo-periods 20% larger, 20% smaller, twice as large, and half as

Table 2.3: Frictional forces under 80 nN load with estimated uncertainties. Runs with rigid substrates eliminate lattice-vibration effects. For each type of substrate (non-rigid and rigid), the first row gives the frictional forces along the periodic and quasiperiodic directions. Friction and error bars in nN are estimated from equal-duration bins given by the pseudo-period, with the error bar the standard deviation of the mean of the independent bins. The row labeled "worst" for each substrate type replaces the pseudo-period and error bar derived from an alternative binning procedure in which the bins are either as given previously, 20% larger or smaller, or twice or half as large, *whichever yields the largest error bar*. For both substrates, the periodic friction is larger than the quasiperiodic by at least seven standard deviations of the mean.

substrate	periodic friction	quasiperiodic friction
non-rigid	30.8(1.0)	18.7(0.9)
worst	*30.8(1.7)*	*18.4(1.5)*
rigid	39.2(1.5)	22.1(1.2)
worst	*39.2(1.5)*	*22.1(2.1)*

large as that extracted from the power spectrum. The table displays as "worst" the estimate with the largest error bar. In each case, the results show a highly significant anisotropy of order 60%–75% with negligible sensitivity to the binning procedure.

One hypothesis for the origin of the frictional anisotropy has involved the difficulty of exciting or propagating phonons through the quasicrystal in the quasiperiodic direction. We can test this by suppressing lattice vibrations entirely using simulations where the atoms in the substrate are artificially fixed in place after equilibration. If phonons were important, we might expect the anisotropy to decrease for the rigid substrate and for the overall friction to be lower. Table 2.3 shows exactly the opposite: the overall friction increases 20–30%, while the anisotropy remains approximately the same or increases slightly on the rigid substrate. With the substrate atoms fixed, the only degrees of freedom left are in the thiol-passivated tip. The difference in friction between the two cases could result from the depression of surface asperities in the non-rigid case, something we see when we plot atomic positions. On both substrates, however, the friction was higher in the periodic direction.

In order to understand why the thiol-passivated tip model was successfully able to capture the expected friction trends, we characterized the trajectory of the last carbon atom in the thiol chains as the tip slid. Figure 2.25 illustrates the vertical height distribution of the quasicystal surface as grey scale maps, where the

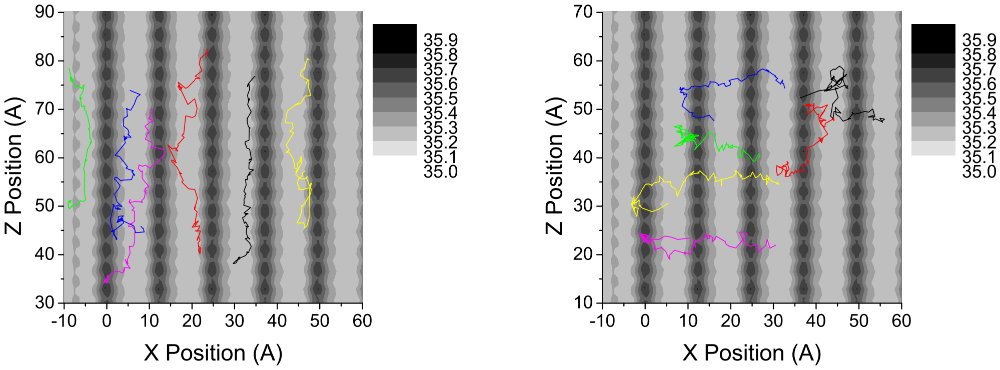

(a) (b)

Figure 2.25: The trajectories of the last carbon atom in the thiol chains when the tip slid in the (a) z-direction (periodic) and (b) x-direction (quasiperiodic). The z-periodicity is 4.03Å, while the periodicity of the approximant in the quasiperiodic x direction is 12.22Å. The gray-scale maps show the vertical heights of the quasicystal surface in Angstroms.

lighter gray corresponds to a lower vertical position. We can identify parallel furrows (low vertical positions) and peaks (high vertical positions) in the gray map due to the periodic surface structure of the quasicrystal. The colored lines indicate the trajectories of the last carbon atom in six representative thiol chains. We observed very different trajectories during sliding in the periodic and quasiperiodic directions. Most significantly, for sliding in the periodic direction (z-direction) illustrated in Fig. 2.25(a), the trajectories remained, on average, in the light colored regions on the gray scale surface height map, indicating that the chains were entrained in the surface furrows. This entrainment could contribute to adhesive friction. In contrast, for sliding in the quasiperiodic direction (x-direction) illustrated in Fig. 2.25(b), the thiol chain tail trajectories exhibited irregular motion patterns corresponding to limited chain entrainment.

Fig. 2.26 provides additional evidence for entrainment of thiol chains in furrows when the tip is dragged in the periodic direction. This shows a kernel-smoothed distribution (kernel width 0.3 Å) of lateral carbon positions for all carbon atoms at heights less than about 2.6 Å above the highest nominal (undepressed) surface-atom center, excluding the first 400 ps of the simulation. Split peaks centered at 6.3 Å, 19.9 Å, and 31.6 Å are roughly consistent with the known furrow centers at lateral positions $(6.61 + 12.22n)$Å for integer n. The splitting of the peaks could indicate affinity of carbons for the furrow sides, although the widths are not quite equal. We can also count the number of carbon atoms at heights less than or equal to the nominal surface height as "in" the furrows; we find 3.6 times as many such carbons when the tip is dragged in the periodic direction as when dragged in the quasiperiodic direction.

Fig. 2.27 shows adhesive energies and maximum forces for runs at 80 nN load stopped at times between 100 ps and 800 ps. After the sliding is stopped, the tip is separated from the substrate, up to a height of 3.2 nm (somewhat longer than the length of a thiol chain, 2.4 nm). We calculated the force on the tip as a function of distance from the substrate during lift-off. The left half of the figure shows total integrated adhesive energy, the right half the maximum force. Both show substantially greater adhesion after runs in the periodic direction, consistent with the idea of entrainment in furrows. Both also level off by 400 ps, supporting our previously cited evidence that a steady state is reached by that time. Entrainment of thiols in furrows and the consequent higher adhesive force when the tip is dragged in the periodic direction could contribute to increased friction. Experimental measurements of adhesive force [163–165] on the two-fold and ten-fold surfaces of d-AlNiCo were performed by lowering and raising of the tip in the normal direction rather than after dragging the tip across a surface, so a direct comparison to experiment is not possible.

2.5.4 Discussion

Entrainment of organic chains in surface furrows provides an intuitively attractive mechanism for anisotropy on this surface. When the tip moves in the periodic direction, parallel to the furrows, the chains preferentially stay aligned, and their adhesion to the furrow sides may contribute to friction. Conversely, when the tip moves perpendicularly, the chains splay in apparently random configurations; additionally, these configurations may change frequently as the chains move across successive ridges in the (approximately) quasiperiodic direction, minimizing adhesion. Of course, this mechanism does not actually depend on quasiperiodicity; the H1 unit cell realizes only the 1/1 approximant to the golden mean. The idea that local topographic features, rather than quasiperiodicity, could control the anisotropy has also been advanced by Filippov *et al.* [142–144]. Using a Langevin model over an external potential representing the substrate, rather than molecular dynamics, the authors suggest that larger force gradients on the atomic scale in the periodic direction could explain the anisotropy. However, the parameters in that model have been questioned [145], and small changes can lead to a reversed anisotropy. The furrow model on the other hand, makes no *ad-hoc* assumptions about effective atomic shapes and should be robust against uncertainties in structural determination.

The furrow model does not come close to the eight-fold observed anisotropy in frictional force. Sliding velocities in these simulations were much larger than in

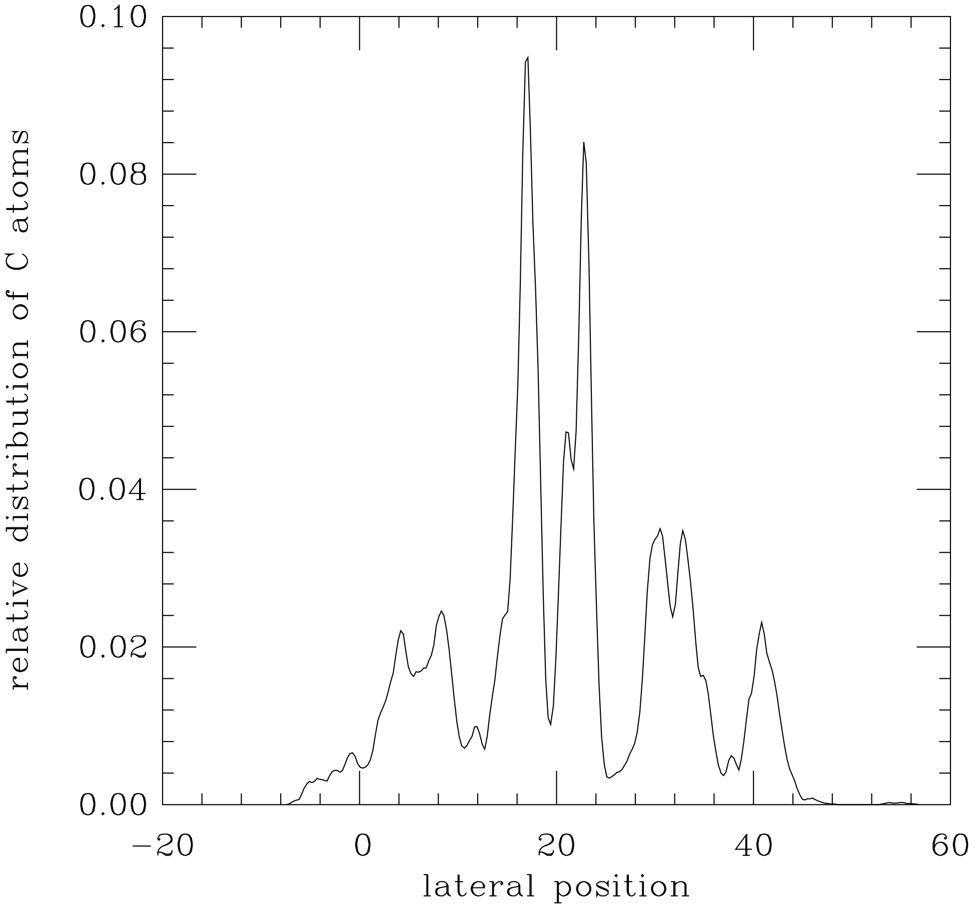

Figure 2.26: Relative distribution of lateral position of carbon atoms during the second half of the simulation dragging in the quasiperiodic direction (*i.e.*, the position axis is along the *periodic* direction.) Only atoms with absolute height less than 38 Å, about 2.6 Å above the nominal surface height, are counted. Split peaks centered at 6.3 Å, 19.9 Å, and 31.6 Å are consistent with carbons localized near furrow edges, where the furrows are spaced 12.22 Å apart.

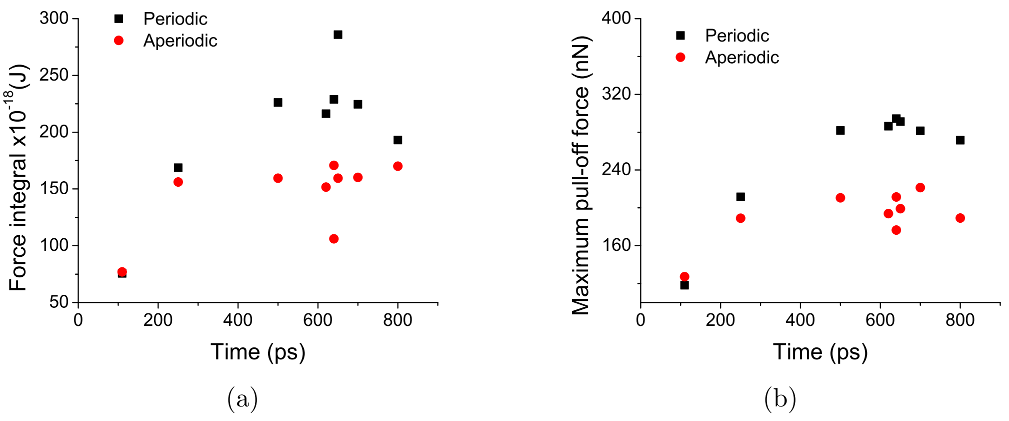

Figure 2.27: Adhesive energies (left) and maximum adhesive forces during lift-off (right) after runs at 80 nN load of durations between 100 ps and 800 ps. The graphs show greater adhesion for runs in the periodic direction, consistent with entrainment of thiol chains in furrows.

the experiment, and it is possible that one would see larger effects at realistic speeds, if they could be achieved.

However, any model relying solely on local topographic features fails to answer the question of why surface friction appears to be lower on the doubly quasiperiodic surfaces of true quasicrystals than on approximants, and lower on the approximants than on other phases in these alloy systems. Nor does it address why quasicrystals show lower friction in engineering-scale pin-on-disk experiments in air, with ploughing through an oxide layer, as well as in nanoscale experiments in vacuum [134].

The Fibonaccium model was designed to test the idea that the difficulty of either exciting or propagating phonons in a quasiperiodic direction of a quasicrystal having both periodic and quasiperiodic directions could account for the anisotropy. These runs found no such effect, and although theoretically phonon spectra in a quasicrystal should exhibit a dense set of gaps [166, 167], experiments find mostly isotropic elastic properties [168, 169]. That friction, likewise, appears isotropic in a model capturing the quasiperiodicity of real quasicrystals while ignoring their topography, weakens the case for the phonon hypothesis.

There are at least three ways out. First, none of the simulations attempted to date considers electronic excitations which may play a role [148]. Second, unrealistic aspects of molecular dynamics, such as scan speeds or finite-size effects, may obscure physical mechanisms.

Finally, it may be that we're looking at two different effects. The giant frictional anisotropy on the two-fold surface of d-AlNiCo may in fact be due entirely to local topographic features, such as thiol-chain entrainment, having nothing to do with quasiperiodicity, while the relatively low friction of quasicrystal surfaces compared to those of approximants, and of approximants compared to other periodic phases, could be due to the greater hardness of the quasicrystals and to a pseudogap in the density of electronic states [128, 170]. Both are definite effects of quasiperiodicity for the quasicrystals and of unit-cell size for the approximants. Both are neatly factored out on the two-fold quasicrystal surface, possibly leaving topography as the only feature different in the two directions.

2.6 Load Dependent Friction Hysteresis on Graphene

2.6.1 Introduction

One important phenomena of the complexity of friction is the sliding-history dependence of friction. This phenomenon can manifest itself in a number of ways, but here we will focus on the behavior observed when friction is measured using an AFM as the normal load is increased and then decreased for a two-dimensional material sample, graphene. Friction experiments have shown that, at a given normal load during a load-unload cycle, the friction force measured during unloading is significantly larger than the friction force that was measured during loading [101,171–176], and the behavior is reproducible (i.e., not due to irreversible wear). This behavior, referred to as load-dependent friction hysteresis, suggests important contributions to friction have not been accounted for in many of the proposed friction models. Note that, while surface wear can result in friction hysteresis [172], such behavior can leave observable damage, and the subsequent friction measurements will be different. Wear can often be avoided in AFM studies, and indeed none of the studies discussed above reported wear. This shows that repeatable hysteresis can occur without irreversible damage or material displacement.

Load-dependent friction hysteresis has been observed on a variety of materials, including graphene [101, 171], polymer layers [173, 174, 177–179], silica and muscovite mica [176]. All of these studies reported higher friction during unloading than loading, but the measurements have also been found to be sensitive to various experimental parameters and conditions. For example, the magnitude of the hysteresis on graphene was observed to increase with maximum applied load [171]. It was also shown that temperature can affect friction hysteresis on poly(N-isopropylacrylamide) surfaces [174]. However, hysteresis was found to be independent of humidity, loading rates, and material contrast on poly-methylmethacrylate (PMMA) surfaces [173]. These finding suggest that friction hysteresis can arise from different, complex physical mechanism.

So far, several different mechanisms have been considered to explain load-dependent hysteresis. For graphene and graphite, friction hysteresis was explained by the relaxation of the out-of-plane deformation of the topmost, locally-delaminated graphene layer upon unloading [101,171]. In methylcellulose films, the hysteresis was attributed to an irreversible reorganization of the topmost polymer layer. This reorganization was suggested to have arisen from the combination of high load and shear stress [177], which resulted in the lifting of this topmost polymer layer from its substrate as load was decreased. A comparable mechanism has been proposed for the hysteric friction behavior of graphene [171] and graphite [101]. Friction hysteresis on polymers has also been explained in terms of the temperature-dependent interaction of the polymer with water present on the surface [174], and by viscoelasticity leading to contact area hysteresis between loading and unloading [178–180]. Another hypothesis, applicable to multiasperity contacts, is that microscopic motion, induced by Poisson contraction or expansion, produces a strong memory dependence of contact area as a function of the loading history [173]. Finally, the water meniscus that forms between tip and substrate in humid air has been shown to lead to friction hysteresis at a silica-mica contact [176].

Friction hysteresis therefore represents a complex aspect of frictional sliding that is not well understood, sensitive to multiple experimental parameters, and attributable to a variety of different mechanisms. In this paper, we probe the origins of load-dependent friction hysteresis on graphene using AFM measurements and MD simulations. Here, the samples used in this study were synthesized by Dr. A. T. Charlie Johnson's group and AFM experiments were performed by Dr. Philip Egberts. The experiments, conducted under ambient conditions (21°C and 40% relative humidity), provide direct evidence of the behavior, and the simulations of atomic friction in vacuum and humid air conditions are used to explore the mechanisms that underlie the experimental observations. The simulations enable investigation of the roles of three previously proposed friction hysteresis mechanisms – out-of-plane deformation, irreversible structural reorganization, and the presence of water in the sliding interface – and their possible effects on frictional behavior. Our study provides atomic insight into the mechanisms underlying load-dependent friction hysteresis on graphene and potentially other materials that exhibit a similar behavior.

2.6.2 Methods

The fully atomistic model consisted of the apex of an amorphous SiO_2 AFM tip placed on a multilayer graphene surface with and without water molecules near the contact as shown in Fig. 2.28. The graphene substrate had in-plane dimensions of 16×10 nm^2; the positions of the atoms in the bottom graphene layer were fixed. The amorphous SiO_2 tip apex was obtained by heating and quenching a block of crystalline SiO_2 and then cutting the hemispherical shape (2.5 nm radius) from the block. The topmost atoms in the tip were treated as a rigid body that was subject to a range of external normal loads (-18∼60 nN) and connected by a harmonic spring to a support that moved laterally at a constant speed of 1 m/s. The spring had stiffness of 8 N/m in the horizontal directions, but did not resist motion in the vertical direction (normal to the graphene surface). A Langevin thermostat was applied to the free atoms maintained a temperature of 300 K. The simulations were performed using LAMMPS simulation software [105].

The inter-atomic interactions within the tip, water and substrate were described via the Tersoff [181], TIP4P [182] and AIREBO [84] potentials, respectively, and the long range interactions between tip, water and substrate were modeled using the Lennard-Jones (LJ) potential. We initially used LJ parameters calculated using the standard mixing rules for estimating interactions between dissimilar atoms. However, to ensure the model was sufficiently accurate for this study, we compared

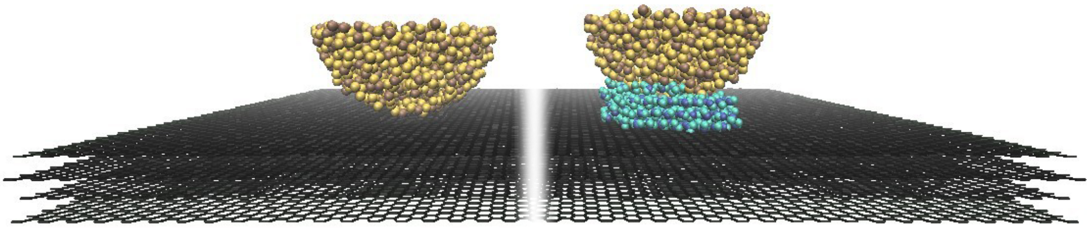

Figure 2.28: Snapshots of the MD simulations of an amorphous SiO_2 AFM tip apex sliding on a multilayer graphene surface with (right) and without (left) water molecules in the interface.

the contact angle between a water droplet and surface calculated from the simulation to the range of experimentally measured values. For both the graphene and SiO_2, we created a water droplet by placing an array of water molecules on the surface of the material and then running dynamics. The water molecules were attracted to one another and formed a droplet; these simulations were run until the potential energy of the system was stable, i.e. fluctuated around a constant value. Then we measured the water contact angle by linearly fitting the positions of the bottom 0.7 nm oxygen atoms at the perimeter of the water at the locations of the extreme contact anlge values, i.e., in front and back of the tip.

The water contact angle on SiO_2 was found to be 96°, much larger than the range of experimentally-measured values (31-66°) [183, 184]. These smaller values are well-established to be due to the presence of hydrophilic silanol (-OH) groups on the surface. The mimic the effect of these groups being present without explicitly modelling them (due to limitations of our potential), we fine-tuned the LJ interaction strength ε between the Si and the O atoms (ε_{Si-O}=0.00909 eV) until a contact angle of 36°, within the experimental range, was achieved. The water contact angle on graphene was calculated to be 112°, which was within the range of values (40° $\sim$ 127°) found in the literature [185–188]. Therefore, no parameter changes were required for this system. However, to explore the effect of wettability, we also ran simulations with an artificially strong water-graphene interaction strength (ε_{C-O}=0.00683 eV) which yielded an unphysically-small water contact angle of 40°.

2.6.3 Results

AFM friction experiments were conducted on chemical vapor deposited (CVD) graphene samples having less than one monolayer coverage, using silicon tips as the

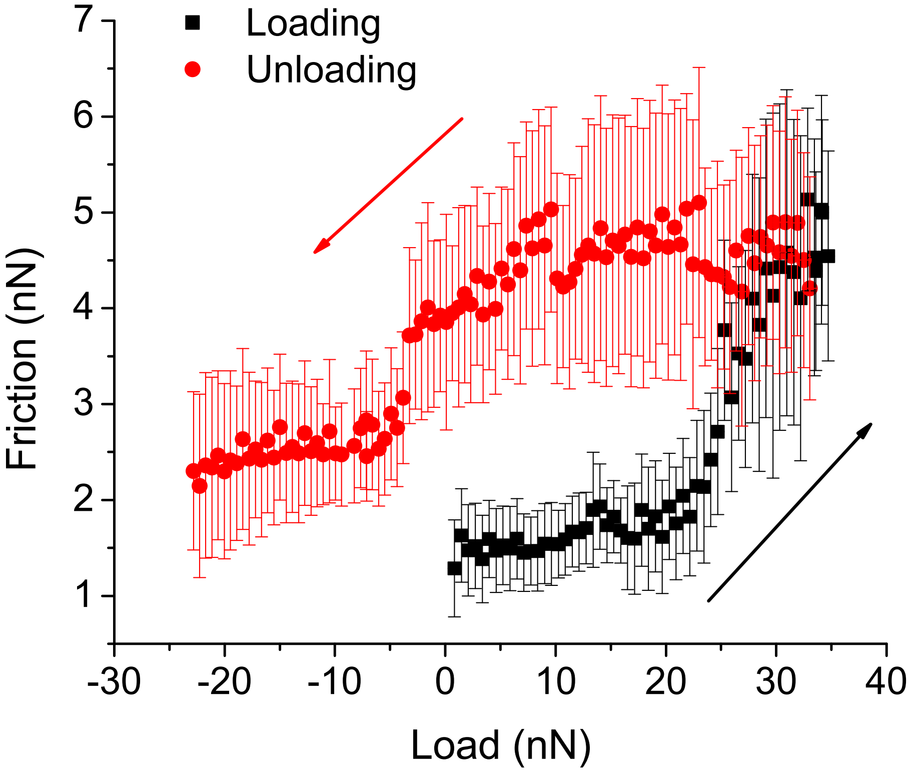

Figure 2.29: An AFM measurement of load-dependent friction hysteresis on graphene. Black squares show the friction measured while the load was increased to a pre-determined value (loading) and red circles show the friction measured while the load was decreased from the pre-determined set point until the tip was pulled out of contact with the sample. Error bars represent the standard deviation in the mean value of friction calculated. AFM experiments in this study were performed by Dr. Philip Egberts

counter surface. These CVD-graphene samples, which were examined on the original polycrystalline copper substrates, exhibited folded regions within the graphene islands, as described in Ref. [171]. The folded regions correspond to three layers of graphene covering the copper substrate, compared with the remaining area of the island that corresponded to one layer of graphene covering the copper substrate. Fig. 2.29 shows the variation of the friction force with normal force on this folded, three-layer graphene region. The data was acquired by measuring friction at a normal force of approximately 0 nN applied normal force, increasing the applied force to ∼35 nN, and then decreasing the normal force until the tip was pulled out of contact with the surface. Fig. 2.29 clearly shows significant friction hysteresis, well outside of measurement uncertainty. Examination of the surface after the measurement did not show any alteration of the surface (wear), which has been proposed as one of the mechanisms for friction hysteresis during load dependence measurements [172], but does not appear to be contributing to the hysteresis here. Additionally, no viscoelastic effects were observed as repeated measurements on single layer graphene in the same area showed that the friction force returned to the same value at applied normal forces during loading, which also suggests that wear is not a mechanism for the observed hysteresis [171].

MD simulations of sliding friction during loading and unloading were conducted for two possible cases, vacuum (Fig. 2.28 (left)) and with water present in the tip-sample contact (Fig. 2.28 (right)), in an attempt to reproduce the experiments most accurately. First, we used a hemispherical silicon dioxide tip sliding on three layers of graphene, matching the number of layers of graphene in the experiments, and in the absence of an atmosphere (vacuum) as illustrated in Fig. 2.28 (left). The simulated data showed that the friction force increased during loading and decreased during unloading, as shown in Fig. 2.30. However, no friction hysteresis was observed. Thus, the inability for the MD simulations to reproduce the experimental friction observations indicates a difference between the conditions in the simulations and experiments that must be addressed.

The experimental data were obtained at 40% humidity, and thus water (or other adsorbates) was likely present in the contact. Previous experiments on mica and silica surfaces suggested that humidity can affect load-dependent friction hysteresis due to a water meniscus present between the tip and substrate [176]. Other previous studies showed that water and small hydrocarbon molecules, adsorb on any surface exposed to air and can affect friction [189, 190]. To explore the influence of a water meniscus on the friction properties measured friction force, water molecules were placed between the tip and the substrate, as illustrated in Fig. 2.28 (right). Since the wettability of water on graphite has been shown to vary over time with environmental exposure [186], we modeled two cases: hydrophilic and hydrophobic. The hydrophilic case was modeled using artificially strengthened graphene-water interactions, corresponding to a contact angle of 40°, whereas the hydrophobic case

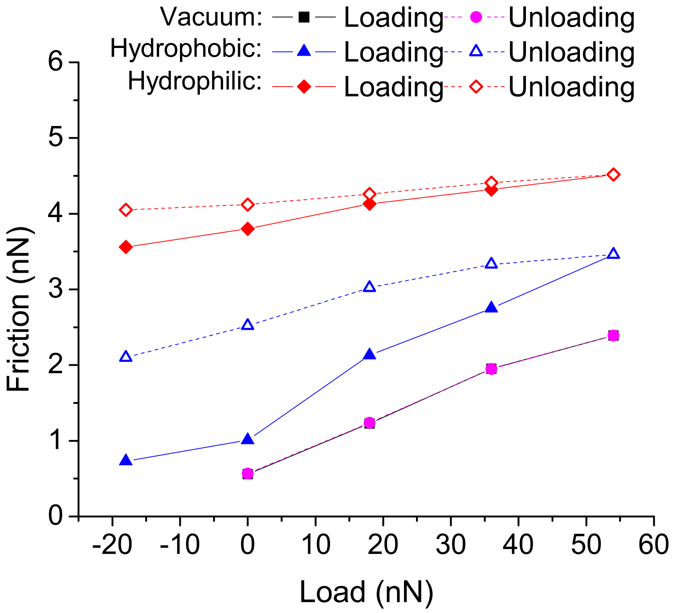

Figure 2.30: Load-dependent friction from simulations run in vacuum (loading and unloading represented by black squares and purple circles, respectively) and humid air. Blue triangles (solid and hollow for loading and unloading, respectively) are the friction for the standard water-graphene interaction strength (hydrophobic, 112° contact angle) and red diamonds (solid and hollow for loading and unloading, respectively) correspond to friction from simulations with the artificially strengthened interactions (hydrophilic, 40° contact angle).

was modeled with the weaker interactions, corresponding to a contact angle of 112°.

Fig. 2.30 shows that friction hysteresis was observed when water molecules were present in the simulation, with either contact angle. Furthermore, Fig. 2.30 shows that the magnitude of the hysteresis, or the difference between unloading and loading friction, is dependent on the hydrophobicity of the graphene surface: increasing the hydrophobicity of the surface increased the degree of hysteresis observed in the friction force. Finally, for both hydrophobic and hydrophilic surfaces, the average friction force during loading and unloading was larger than that calculated from the vacuum simulations. In the next section, the friction mechanisms attributing to the origins of the measured friction hysteresis in both experiment and simulation, as well as the offset between the friction force measured in the three simulations, will be discussed.

2.6.4 Discussion

To understand the observed friction hysteresis, we investigated previously-proposed mechanisms, searching for evidence of their contributions in our simulations. We first explored the potential role of out-of-plane deformation of the graphene [101, 171]. Out-of-plane deformation, also referred to as puckering, occurs when the upper graphene layer conforms to the tip such that there is a wrinkle in front of the tip that can resist sliding, as well as increase the area of the tip the graphene covers during sliding, and therefore increase friction. This deformation has been proposed to be the source of variations in friction with number of graphene layers [80, 104]. We quantified deformation in these simulations as the time average of the difference between the vertical position of the graphene wrinkle in front of the tip and the vertical position of the graphene in the contact below the tip. In all cases, with and without water, as well as with varying contact angle, the difference between the deformation during loading and unloading at a given load was statistically insignificant. This suggests that out-of-plane graphene deformation is unlikely to be contributing in the load-dependent hysteresis observed in the simulations.

Another hypothesis to explain load-dependent friction hysteresis is irreversible reorganization of the adsorbates in the contact interface, which has been proposed as an explanation for friction hysteresis in polymer layers [175, 178, 179] as well as adhesion hysteresis in various surfactant monolayers [191]. In this case, we looked for structural changes in the water in the contact area. Structure or organization of the water molecules within the contact was characterized using the radial distribution function (RDF) of the oxygen atoms in the water molecules, which has previously been used to quantify structure of water in both experiment and simulation [192]. Fig. 2.31 shows the RDF for four cases that are derived from the time and load averaged structure of the water molecules in the contact during the loading and unloading processes for both the hydrophobic and hydrophilic surfaces. Note that these are calculated only using the oxygen atoms in the contact area, i.e. the layer of water atoms adjacent to the graphene, and so do not necessarily exhibit the features expected for bulk water. Regardless, the height of the RDF peak (particularly the first peak) does provide a tool for characterizing structure. We first observe that the RDF peak is sharper (greater maximum value) for the hydrophilic case than the hydrophobic case, during both loading and unloading. Sharper RDF peaks correspond to more well-defined structure in the contact, which may partially explain the larger friction observed in Fig. 2.30 for the hydrophilic graphene. We also observe that, for either contact angle, the RDFs during loading exhibit slightly sharper peaks than during unloading. This suggests that the water adopts a more ordered structure during loading which is not completely lost on unloading. However, we also compare the structural hysteresis, i.e., the difference between the heights of the first RDF peak during loading and unloading, of the two contact angle cases (see inset of Fig. 2.31). Both contact angle cases exhibit structural hysteresis with approximately the same magnitude. This is inconsistent with the large difference in friction hysteresis between the hydrophobic and hydrophilic cases in Fig. 2.30 which indicates that, while irreversible reorganization may be a contributing factor, there is at least one other mechanism involved in the process.

We next explore the possible contribution of the water meniscus. In previous work, it was suggested that friction hysteresis may be attributed to hysteresis in the size of the contact area caused by water around the AFM tip which built up during loading and did not evaporate during unloading [176]. There is no evaporation in the simulations, but this gives us a clue as to another possible way the water could be affecting hysteresis. We quantified the size of the contact as the number of water molecules in contact with the graphene, where contact was determined based on an empirical distance criteria. Specifically, a water molecule was assumed to be in contact if the minimum distance between its oxygen atom and any carbon atom in the substrate was less than 0.35 nm, where 0.35 nm was chosen to be a reasonable estimate of contact based on visual observation of the simulation. Note that this is distinct from the common notion of contact area used for dry contacts, where the solid-solid contact area is usually considered. With water present in the simulation, the shearing interface during sliding becomes the water-graphene interface, rather than the silicon tip-graphene interface, as the silicon tip did not penetrate through the last layer of water molecules at any of the loads examined. We therefore will apply the term "contact area" in the remainder of the discussion to denote the size of this shearing interface, despite the term's typical restriction to solid-solid sliding interface. Furthermore, the tip and the water molecules form a single body in the simulations that slides together along the graphene surface, resulting in a necessary redefinition of the contact area as stated earlier. Thus, we consider the interaction area between the meniscus and the graphene for the present analysis.

Fig. 2.32 shows the number of water molecules in the contact as a function of load during loading and unloading (symbols) for both hydrophobic and hydrophilic

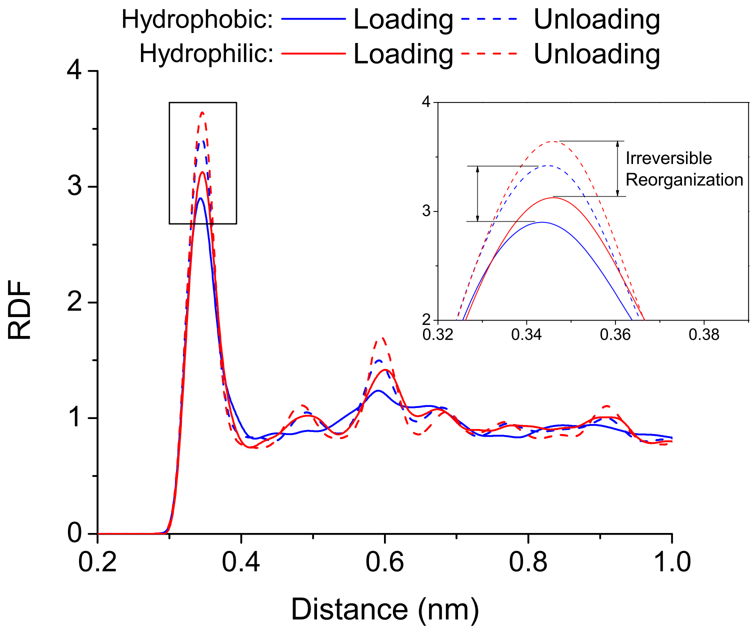

Figure 2.31: Radial distribution function of the O-O pairs in the water in the contact calculated during loading and unloading. Inset is a close up of the first RDF peak indicating there is some irreversible reorganization between loading and unloading, but the magnitude of this hysteresis (difference between RDF peak height during loading and unloading) is not dependant on contact angle.

graphene. The contact area of the water without the tip present is shown as dashed lines. Hydrophilic graphene corresponds to larger water contact areas as expected. This is demonstrated by the offset between the blue dashed line/data points and the red dashed line/data points in Fig. 2.32. Furthermore, the presence of the tip increases the contact area at the shearing interface, as demonstrated by the offset in the contact area between the dashed line and the data points for both cases shown in Fig. 2.32; while the effect is larger for hydrophobic graphene (13-61% increased contact area), the effect for hydrophilic graphene is still significant (5-15% increased contact area).

More importantly, the contact areas in Fig. 2.32 exhibit load-dependent hysteresis, consistent with the hysteretic friction behavior in Fig. 2.30. Similarly, the degree of hydrophobicity influences the size of the contact at the sliding interface, again with the same trend as the friction. More hydrophilicity corresponds to a bigger water-graphene contact area and higher friction. Therefore, the friction hysteresis appears to be a direct result of the hysteresis in the contact area of the shearing interface, i.e. between water and graphene, which is only observed if water is present in the interface.

This suggests that the water-graphene contact area, as opposed to puckering or structure of the water molecules in the contact, is the dominant friction mechanism of the three investigated. However, the origin of the contact area hysteresis itself requires further discussion, since it cannot be explained by evaporation as proposed previously [176]. One possibility is suggested by the difference between the hysteresis (in both friction and area) in the hydrophobic and hydrophilic simulations. It is well known that contact angle hysteresis can be observed when water is added to or removed from a droplet, or when a droplet moves on a tilted surface due to gravity, due to the pining of the contact line at impurities, defects, or other heterogeneities on the surface [193]. Therefore, it is possible that a meniscus is present at the tip-sample contact in the experiments, and contact angle hysteresis occurs during loading and unloading as depicted in Fig. 2.33. For the sliding case, there is a distribution of contact angles around the contact line, with the largest difference occurring between the front and the back side of the tip. This is because the front angle is always larger as the water is pushed forward by the lateral motion of tip. The load-dependent hysteresis applies to the contact angle at all locations around the contact line such that, during loading, all of the contact angles will decrease as the tip pushes down towards the surface; the contact area will increase with increasing load correspondingly. Then, during unloading, the contact angles will increase as the tip pulls the water up as load is decreased, but the hysteresis in all the contact angles (and the contact area) will prevent them from returning to the same magnitude at the same load.

We quantified the contact angle during loading and unloading in the simulations, by linearly fitting the positions of the bottom 0.7 nm oxygen atoms at the

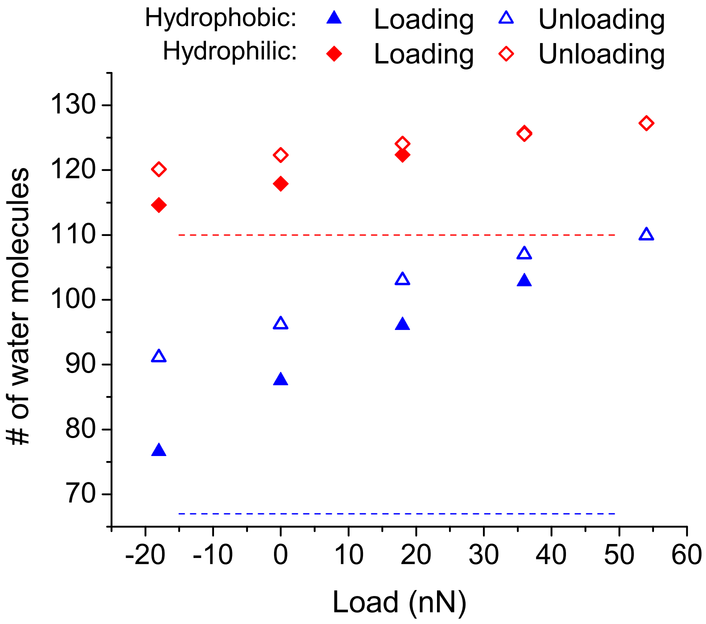

Figure 2.32: Number of water molecules in the contact (a measure of contact area) with the substrate during loading and unloading process. Blue triangles (solid and hollow for loading and unloading, respectively) correspond to the standard water-graphene interaction strength (hydrophobic graphene, 112° contact angle) and red diamonds (solid and hollow for loading and unloading, respectively) correspond to the artificially strengthened interactions (hydrophilic graphene, 40° contact angle). Dashed lines represent the contact area of the water on the graphene without the tip present.

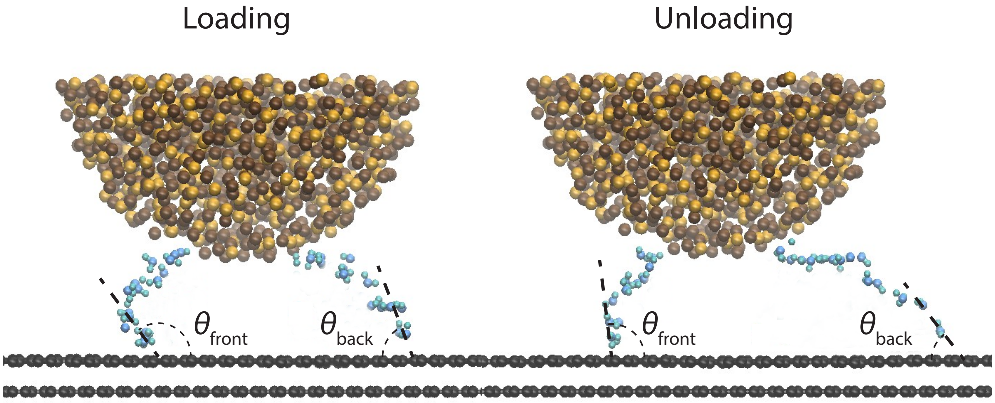
Loading
Unloading
θ_{front}
θ_{back}
θ_{front}
θ_{back}

Figure 2.33: Snapshots of the tip/water sliding (from right to left) along the surface at 0 nN during loading (left) and unloading (right). Only the oxygen atoms at the perimeter of the water droplet are shown in the snapshot from the MD simulation to simplify the image. The contact angles have been determined using the linear fits (thick dashed lines) of the outer edges of the water ball and are denoted θ_{front} and θ_{back} for each case.

Table 2.4: Contact angles in front of and in back of the tip during loading and unloading for each equilibrium contact angle. θ_0 is the equilibrium contact angle and $\theta_L - \theta_U$ is the contact angle hysteresis, the difference between the loading and unloading angles.

θ_0		θ_{front}	θ_{back}
$Hydrophilic(40^\circ)$	Loading	60.8°	41.8°
	Unloading	52.1°	35.2°
	$\theta_L - \theta_U$	8.7°	6.6°
$Hydrophobic(112^\circ)$	Loading	129.9°	63.1°
	Unloading	97.6°	51.5°
	$\theta_L - \theta_U$	32.2°	11.6°

perimeter of the water at the locations of the extreme contact anlge values, i.e., in front and back of the tip, shown in Fig. 2.33. The results, time averaged over loading and unloading for each equilibrium contact angle, are summarized in Table 2.4. We observe that both the front and back contact angles are clearly larger during loading than unloading. Furthermore, the difference between front and back angles is much greater for the hydrophobic case, consistent with the fact that the magnitude of contact angle hysteresis due to adding or removing water to a droplet tends to be directly related to the equilibrium contact angle [193]. Most importantly, the load-dependent contact angle hysteresis we observe is consistent with the friction hysteresis in Fig. 2.30 and contact area hysteresis in Fig. 2.32. This can be explained as follows: during loading, the water in the contact area is pushed outward and spreads out on the surface. The contact area increases while the contact angle decreases; then, during unloading, the contact line was pined to the surface, while the contact area decreases and the contact angle increases, they do not return to their initial values. Therefore, the friction hysteresis in the simulations, and possibly in the experiments, may be explained by contact area/angle hysteresis.

2.6.5 Conclusion

In summary, MD simulations were used to investigate the origins of load-dependent friction hysteresis measured in AFM experiments. Only simulations with water in the contact area were able to reproduce the experimentally-observed friction hysteresis. We then used the simulations with two different water-graphene interaction strengths to explore the origins of the hysteresis. First, the out-of-plane deformation of graphene was calculated from the atomic positions of the carbon atoms and found not to exhibit hysteresis, demonstrating that this mechanism does not explain the hysteresis observed in the friction. Based on the necessity of having water in the simulations to capture friction hysteresis, we next focused on mechanisms related to the water in the contact. Quantifying the structure of the water in the contact using a radial distribution function, we found that there was some hysteresis due to irreversible reorganization of the water molecules in the contact, but that hydrophobicity of the graphene surface did not affect the magnitude of the hysteresis, which was inconsistent with the friction trends. Given the small effect of hydrophobicity on irreversible reorganization, this mechanism could not fully explain the observed friction hysteresis. Lastly, we calculated the water-graphene contact area and found trends in the effect of loading/unloading and the effect of hydrophobicity that were consistent with those observed in the friction measurements in both experiments and simulations. The relationship between contact area and friction was explored by calculating the range of contact angles around the tip during sliding in the simulations. All contact angles around the tip exhibited hysteresis during loading vs. unloading, consistent with the friction measurements. Therefore, the simulations support the following mechanism to explain the load-dependent friction hysteresis: during loading, water is pushed outward as the contact area increased, and then during unloading, the water is pulled away from the surface decreasing the contact area, but not to its original value due to pinning of the contact line. The effect is much stronger for more hydrophobic graphene, where hydrophobicity was artificially controlled by changing the graphene-water interaction strength in the MD potential. This suggests an intrinsic energy dissipation mechanism related to the motion of water molecules across the graphene surface that is strongly dependent on humidity and the hydrophobicity of the material on which the friction is measured. The mechanism leading to the hysteresis itself appears to be an intrinsic aspect of the water-graphene interaction: the simulated graphene sample does not have any impurities or defects. Rather, an intrinsic pinning and dissipative interaction between water molecules and the graphene surface is seen to occur as forces act the move the water along the graphene surface. This effect could be further increased by features such as impurity or vacancy defects, steps, grain boundaries, or contaminants, all of which may be present in the experiment.

Chapter 3

NANOTRIBOLOGY ON IMPERFECT SURFACES

In most physical applications, "perfect" surfaces rarely exist. Often, surface defects, such as voids, impurities, stacking faults, and step edges exist and cause an imperfect surface. Studying and understanding the tribological behaviors on imperfect surfaces is significant for small-scale device applications, as the atomic sized defects play an important role in device performance. In this section, we aimed to answer the long standing question, discussed below, related to how surface defects (step edges) affect atomic friction. The overall goal is to understand friction due to well-characterized imperfect features and provide clues to the nature of atomic friction generally.

3.1 Effect of Tip Shape on Atomic Friction at Graphene Step Edge

3.1.1 Introduction

Experimentally, the effect of atomic-scale step edges on friction is typically measured using an AFM tip that scans forward and backward, such that during one line scan it moves down the step and during the next it moves up the step. The materials for which data is available are NaCl [25, 26, 28, 29, 194], MoS_2 [28], and graphite (multilayer graphene) [27–29, 195]. All of these report that there is a lateral force resisting motion as the tip moves up a step [25–28, 194, 195] which previous work suggests may be due to several different factors [196]. However, for a tip scanning down the step, two very different friction trends have been observed: the lateral force may assist [26] or it may resist the motion of tip [25–29, 194, 195].

The observation that lateral force resists motion as the tip moves down a step has been explained by the so-called Schwoebel effect [26, 28]. The original papers by Schwoebel present theory that describes activation barriers for diffusion at atomic steps [197, 198]. In the context of friction, the argument is that an additional lateral force is required to overcome this step-induced energy barrier. This picture is complicated, however, by a study that showed no resistive force at atomic steps for sufficiently sharp AFM tips [26]. In other words, the shape of the tip (specifically the bluntness) was found to affect the frictional resistance at a step edge. The interpretation of these results was that different friction trends can be associated with changes in the energetic profile due to the tip shape.

In this study, we explore the relationship between tip bluntness, the energy barrier at the step, and friction using MD simulation. We develop simulations that reproduce the experientially-observed friction trends and show that the connection between tip shape and energy is the tip trajectory over the step. Finally, we present a comprehensive explanation of the effect of tip shape on friction at a graphite step edge: shape affects tip trajectory, which in turn changes the potential energy landscape, and finally determines the friction force.

3.1.2 Methods

The MD simulation described the apex of an AFM tip scanning over a graphite step edge, see Figure 3.1. Three graphite sheets were ABA-stacked in the zig-zag configuration relative to the sliding direction, with an interlayer distance of 0.335 nm. The atoms in the bottommost layer of graphite were fixed to model a supporting substrate and the atoms at one end (in the scan direction) of all the layers were fixed as well to prevent relative sliding. The boundaries were periodic in the $x - y$ plane, and the boundary in the z-direction was formed by the fixed bottom layer of graphite and the rigid body of atoms at the top of the tip. The model tip had a hemispherical geometry and consisted of carbon atoms in a diamond structure.

Spherical tips comprised of diamond of various diameters (3.2, 5.6, 11.2 and 20 nm) were studied. We controlled the tip shape by removing atoms from the tip apex such that a hemisphere without truncation modeled a sharp tip and truncated hemispheres modeled blunt tips. We created two blunt tips, one with 25% of the hemisphere removed and one with 50% of the hemisphere removed. A constant external normal load was maintained on the rigid body at the top of the tip. The rigid body was connected by a harmonic spring to the support (virtual atom) that moved at 4 m/s in the x-direction. Even though there is large difference between the sliding speed in this simulation and that accessible to typical AFM experiments, previous research has shown that the energetics predicted by a high speed MD simulations can be reliably used in interpreting AFM data [199]. The spring had stiffness of 8 N/m in the x- and y-directions, but did not resist motion in the z-direction (normal to the graphite surface). A Langevin thermostat was applied to the free atoms in the system to maintain a temperature of 300K. The inter-atomic interactions within the tip and substrate were described via the AIREBO potential [200], and the long range interactions between tip and substrate were modeled using the LJ potential (energy minimum 0.016 eV, zero-crossing distance 0.28 nm). The simulations were performed using the LAMMPS simulation software [105].

3.1.3 Results and Discussion

Figure 3.2 shows the MD-predicted lateral force experienced by the sharp (a) and blunt (b and c) tips as they move down the step. A negative lateral force

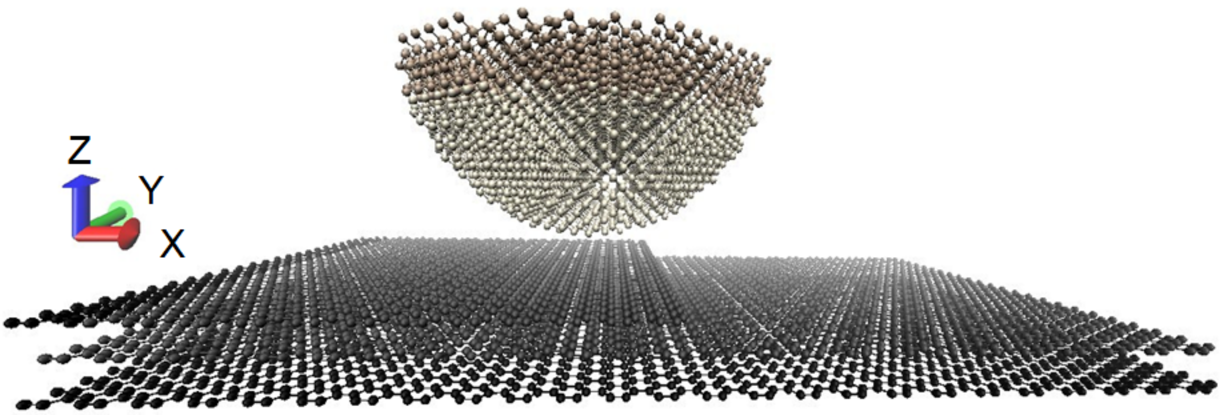

Figure 3.1: Illustration of the MD simulation of a 5.6 nm diameter AFM tip sliding over graphite with a step edge.

corresponds to an assisting force that helps the tip move forward and a positive lateral force corresponds to a resistive force that impedes the tip's motion. We can compare these plots in terms of three characteristic features: the first lateral force peak, the minimum lateral force, and the second lateral force peak, as shown in Figure 3.2 (a). The first lateral force peak occurs before the tip moves down the step and is the feature identified in experiments as the lateral force that resists the motion of tip [25, 25–29, 195]. The minimum lateral force is an assistive force observed in measurements taken using a sharp tip only [26]. The second lateral force peak occurs after the tip has moved down the step; this feature has not been reported experimentally but, as will be discussed later, is reasonable in terms of the energetic landscape near the step.

Our simulation results show that the first lateral force peak and the minimum lateral force valley exist regardless of the tip shape, but their relative magnitudes change significantly. We evaluate the effect of truncation by comparing these two features for our three model tips: perfect hemisphere (i.e. 0% truncation), 25% truncation, and 50% truncation. As shown in Figure 3.2 (d), the magnitude of the first lateral force peak increases (becomes more positive) while the magnitude of the minumum lateral force decreases (becomes less negative) with increasing degree of truncation. This explains the experimental observation that an assistive force is only observable (i.e. large enough to be measured) for sharp tips and that the resistive force is dominant for blunt tips [26]. The magnitude of the relatively small second lateral force peak changes little with truncation.

We explored the effect of tip truncation for different normal loads (from 2 to

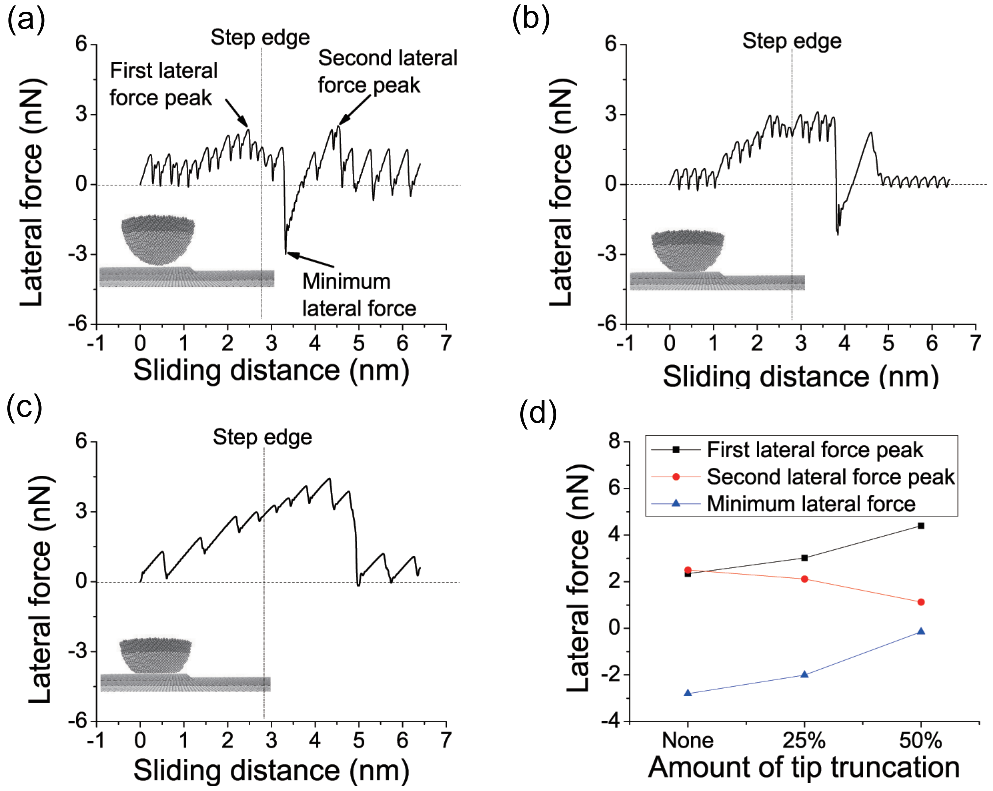

Figure 3.2: Lateral force for (a) sharp, (b) 25% truncated and (c) 50% truncated tips scanning across the graphite step edge. The tip diameter is 5.6 nm and the normal load is 0 nN in these three plots. (d) Variation of specific features of the lateral force traces with amount of tip truncation.

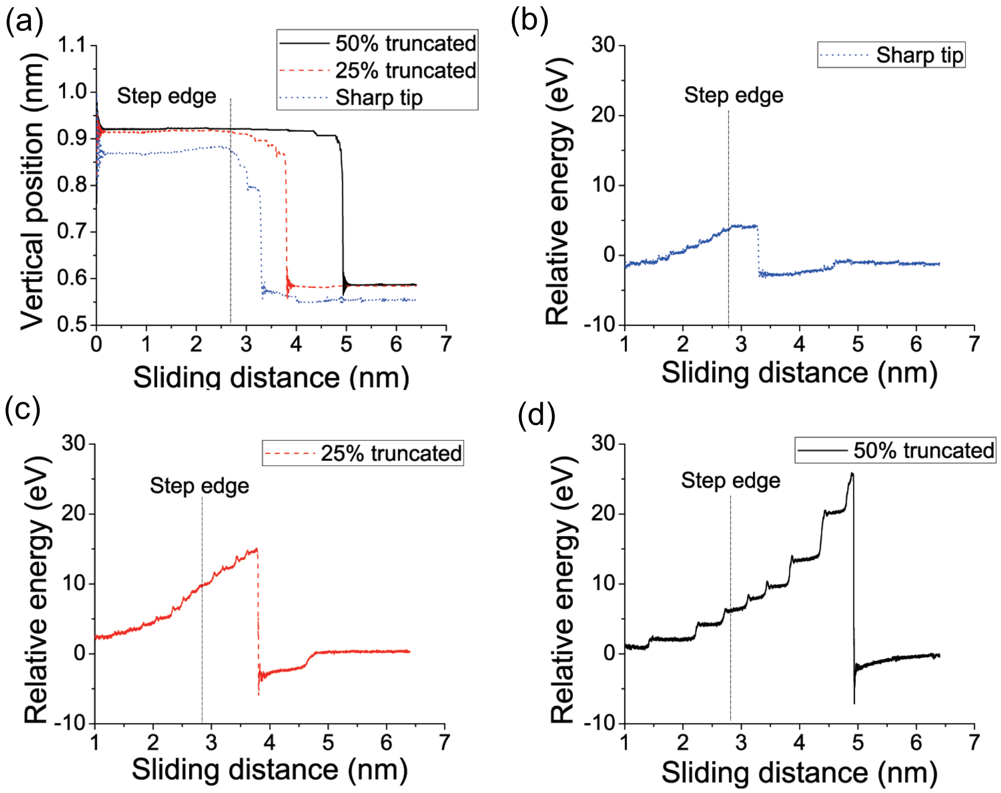

Figure 3.3: (a) The vertical positions of tips of different bluntness scanning forward across the step edge. Potential energy of the (a) sharp, (b) 25% truncated and (b) 50% truncated tips scanning forward across the step edge.

15 nN) and tip radii (from 3.2 to 20 nm) in our MD simulations. The results are consistent with the preceding discussion and the results in Figure 3.2, although the actual friction forces naturally depend on the tip geometry and load.

We now analyze the connection between tip bluntness and friction. One of the benefits of MD simulation is that we have atomic-scale information about the contact throughout the sliding process. We tracked the positions of the bottommost atoms of the three different tips during scanning; the results are shown in Figure 3.3 (a). The vertical position of the bottom of each tip does not change during the first 2 nm of sliding, indicating that the tip is moving along the upper terrace. The sharper tips are slightly closer to the graphite (0.24 nm with sharp tip, 0.26 nm with 25% truncated tip and 0.265 nm with 50% truncated tip) potentially because they experience a greater pressure for the same load. Then, at a sliding distance that is dependent on the tip shape, there is a sharp drop in the vertical position of the tip indicating that it has moved down the step. The distance from the step at which this drop occurs is significant and will be called the step-down distance. After the drop, the vertical position of each tip is again roughly constant indicating they are moving along the lower terrace. It is important to note that the change in vertical position as the tip moves from the upper to the lower terrace is approximately equal to the graphite interlayer distance of 0.335 nm. However, the key observation from Figure 3.3 (a) is that the step-down distance moves further from the step as the bluntness of the tip is increased. Specifically, the step-down distance is 0.65 nm for the sharp tip, 1.05 nm for the 25% truncated tip and 2.25 nm for the 50% truncated tip.

Previous experimental studies interpreted their results using a one-dimensional empirical potential energy model [26, 28]. These models predict there is an energy barrier (the Schwoebel barrier) at the step which can be used to explain the extra friction force. If the energy barrier is increased, a larger friction force is necessary to overcome it. We repeat this type of analysis using our MD simulation. The potential energy profiles predicted by our model for each of the three tips are shown in Figure 3.3 (b), (c) and (d). The energy is expressed relative to that of the tip on the lower terrace. We observe that the distance at which the energy is at a maximum is the same as the tip step-down distance. In addition, the maximum energy (the energy barrier) increases with tip bluntness. Thus, our findings corroborate the previous suggestion that friction at a step is due to an energy barrier, and the magnitude of that barrier (and the corresponding resistive force) is affected by tip shape. However, our simulations reveal that the connection between shape and energy is the tip trajectory (step-down position). Note that we also observe an energy well just after the step edge which is consistent with the observation of the minimum lateral force and second lateral force peak in the MD simulations.

3.1.4 Conclusion

In summary, atomistic simulations of friction at a graphite step edge reveal that the connection between tip bluntness and friction is the tip trajectory. A blunter tip will step down at a position further from the step itself; this in turn increases the height of the potential energy barrier at the step; finally, the larger energy barrier requires a larger friction force to overcome it. The results explain the relationships between tip bluntness, tip trajectory, potential energy and friction.

3.2 Atomic Friction at Exposed and Buried Graphene Step Edges

3.2.1 Introduction

Friction at the atomic scale has been at the forefront of scientific interest in recent years. In general, atomic-scale friction study is important because it can lead to a fundamental understanding of how friction occurs, as well as provide the knowledge base needed for rational design of nanomechanical devices. The focus of this work is graphite, a solid lubricant that exhibits low friction and wear, large Young's modulus, and high load bearing capacity [201]. This material can be reliably modeled using MD simulations and accessed experimentally using an AFM. More importantly, graphite is stable, atomically-flat, and ordered. These properties are ideal for studying friction because its well-defined atomic features can be directly correlated to friction patterns. In this research, we focus on the atomic-scale friction at graphite step edges.

There are two types of step edges: exposed, where the step occurs at the outmost layer; and buried, where the step is underneath another layer of material. Most previous experiments and simulations focused on friction at exposed step edges, including those on NaCl [25,26,28,194], MoS_2 [28], and graphite [27,28,31,195,202–204]. In all cases, enhanced friction was observed at the step edges during step up scans, i.e. as the AFM tip moved up the step from a lower to higher terrace. However, during step down scans, some studies reported enhanced friction at the step [25, 27, 28, 31, 195, 202] while other did not [26, 31, 202]. This difference has been attributed to tip bluntness, which can affect the energetics and trajectory of the tip as it moves over the step [26, 202], and environmental effects, which can change the friction behavior at the steps through a meniscus formed between tip and substrate [31]. In addition to the extensive research on exposed step edges, two recent experimental studies [203, 205] measured friction on both exposed and buried graphite steps and reported much smaller friction at the buried step edges. However, more investigation is required to understand these observations.

In this paper we investigate the origins of friction at exposed and buried graphite step edges using AFM measurements combined with fully atomistic MD simulations. To our knowledge, there have been no previous fully atomistic simulations of buried steps. Experiments and simulations are used to characterize friction as the AFM tip scans up and down the exposed and buried steps. The effect of tip bluntness on friction trends is also explored. The MD simulations provide detailed information about the surface topography and shape of the tip, both of which determine the trajectory of the tip as it moves over steps. Specific features of this trajectory are then used to explain the observed friction trends.

3.2.2 Methods

Experimentally, the highly oriented pyrolytic graphite (HOPG) samples (Alfa Aesar) were cleaved right before the measurements. A commercial AFM (NT-MDT

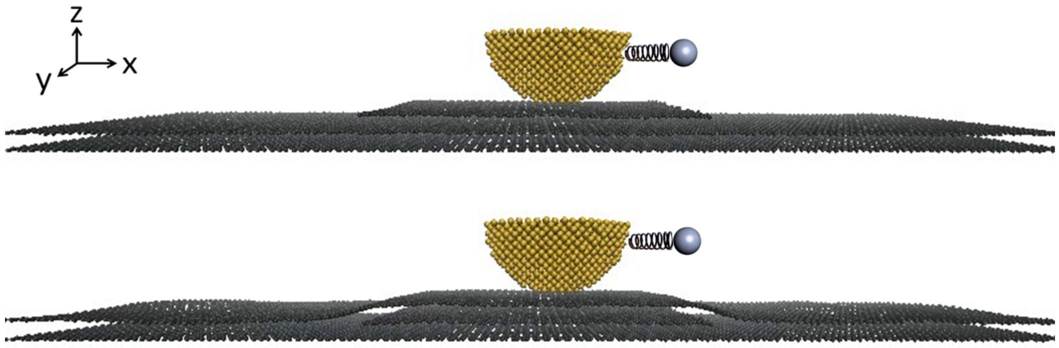

Figure 3.4: Illustration of the molecular dynamics simulation of a 2.8 nm radius AFM tip sliding over exposed (top figure) and buried (bottom figure) step edges on graphite.

SOLVER Next) was used for the lateral force imaging. Silicon cantilevers with an integrated tip (Mikromash CSC37) were used as force sensors. The normal bending and lateral twisting spring constants of the force sensor were determined using the Sader method [206, 207]. The optical sensitivity of the detector was assumed to be the same in both lateral and normal directions [208]. All AFM experiments were conducted at room temperature at 0 nN applied load (unless otherwise specified).

The fully atomistic model, illustrated in Fig. 3.4, mimicked the apex of the AFM tip scanning over exposed and buried step edges. For exposed step edges, a smaller layer ($7 \times 11nm^2$) of graphene was placed on top of two larger layers ($21 \times 11nm^2$). For buried step edge, the smaller layer of graphene was placed in between the two larger layers. The model tip consisted of carbon atoms in a diamond structure. The sharp tip was a hemisphere with a 2.8 nm radius and the blunt tip was a truncated hemisphere. To simulate the compliance of an AFM system, the tip was connected by a harmonic spring to a support that moved with a constant speed of 6 m/s in the x-direction. The spring had stiffness of $k = 8N/m$ in the x- and y-directions, but did not resist motion in the z-direction (normal to the surface). Zero normal load was applied to the tip, but it was allowed to move freely in response to normal forces due to interactions with the substrate. The atoms in the bottommost layer of the substrate were fixed, and the top three layers of tip acted as a rigid body. A Langevin thermostat was applied to the remainder of the atoms to maintain a temperature of 300 K. Periodic boundaries were applied in the $x - y$ plane. The inter-atomic interactions within the tip and substrate were described via the AIREBO potential [200], and the long range interactions between

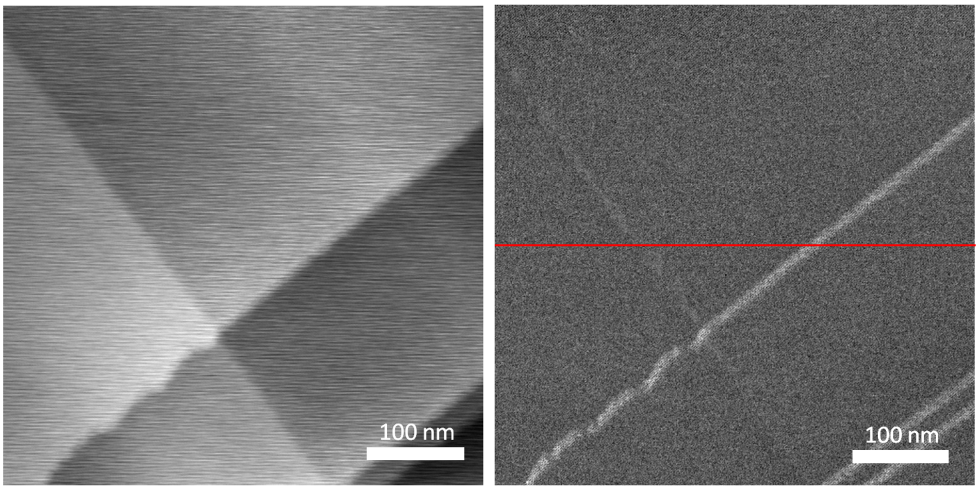

(a) (b)

Figure 3.5: AFM measurements of step edges on HOPG obtained using a sharp tip: (a) topography and (b) lateral force, where the exposed and buried steps can be identified by the different contrast.

tip and substrate were modeled using the Lennard-Jones potential with parameters from ref. [200]

3.2.3 Results and Discussion

A previously-unused, i.e. sharp, tip was selected for the first set of experimental measurements. The tip had a radius of 6.6 ± 2.1 nm, as estimated using the Johnson-Kendall-Roberts (JKR) model [209] based on a pull-off force of 9.5 ± 3.2 nN. Fig. 3.5 shows an AFM topography image of the HOPG surface with two step edges and a corresponding lateral force image. Both steps were single layer as indicated by their height of $\sim$0.3 nm. Exposed and buried steps could not be distinguished in the topography image. However, in the lateral force image, the exposed steps exhibited much higher contrast than the buried steps [205].

Fig. 3.6(a) shows line profiles of the lateral force during a forward scan (step down) and backward scan (step up). During a forward scan, a positive lateral force resists motion, i.e. friction, and during a backward scan, a negative lateral force corresponds to friction. A friction peak was observed at both exposed and buried steps during the backward scan. However, the friction at the exposed step was 2.2 ± 0.6 (averaged over 10 measurements) times larger than at the buried step. No significant friction peak was observed at either step during forward scans. This

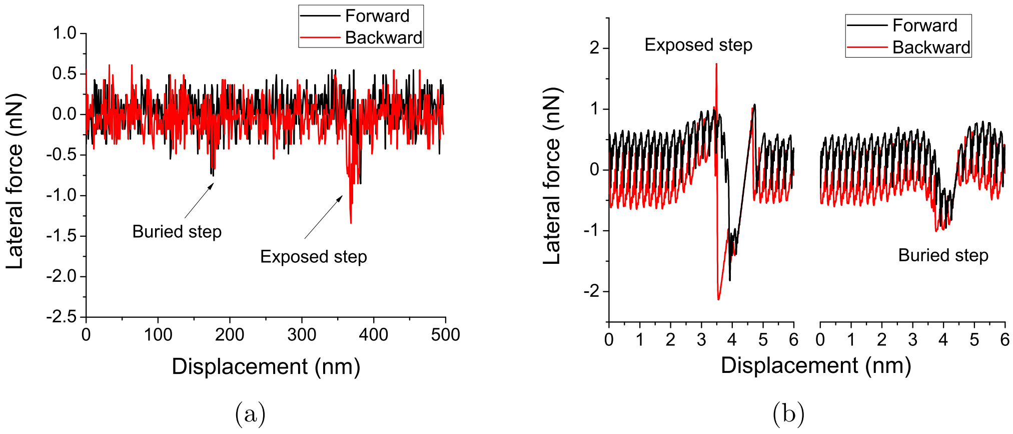

(a) (b)

Figure 3.6: Line profiles of the lateral force at exposed and buried steps obtained using a sharp tip from (a) AFM and (b) MD simulations. Results are displayed such that the tip moves down the step during forward scans (black lines) and up the step during backward scans (red lines).

observation is consistent with previous reports of friction at exposed steps measured using atomically sharp tips [26, 202].

To model the sharp tip experiments, we performed MD simulations with a hemispherical tip scanning across exposed and buried step edges. Fig. 3.6(b) shows the predicted lateral force from forward and backward scans. During backward scan, friction peaks were observed at both exposed and buried step edges and, consistent with experiment, the friction peak at the exposed step was 2.9 times larger than at the buried steps. During forward scans, although friction peaks were observed at both steps, they were almost an order of magnitude smaller than those from the backward scans. Although friction peaks were not observed in the forward scans in experiment, this may be because the enhanced friction at the step was smaller than the noise in the friction measurement. In the simulations, where the forward scan friction peaks were detectable, the friction at the exposed step was 1.6 times larger than that at the buried step.

Previous experiments on NaCl surfaces [26] and our previous simulations on graphite [202, 204] indicated that tip bluntness may affect the friction at exposed step edges. To investigate the effect of tip bluntness on exposed and buried step edges, we repeated our AFM measurements with a tip that was made blunt by repeated scanning at 50 nN load. Evidence of the tip getting blunter can be found in the pull-off tests performed before and after high load scanning, which showed that the pull-off force increased by a factor of three (from 9.5 ± 3.2 to 26.9 ± 8.5 nN)

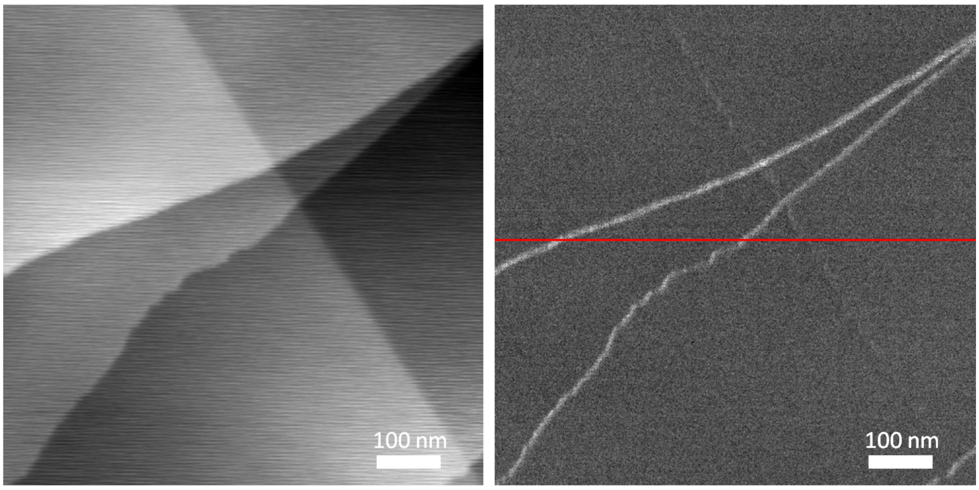

(a) (b)

Figure 3.7: AFM measurements of step edges on HOPG obtained using a blunt tip: (a) topography and (b) lateral force, where the exposed and buried steps can be identified by the different contrast.

after repeated scanning. The radius of the blunt tip was 18.4 ± 5.8 nm, estimated using the JKR model.

After obtaining the blunt tip, we located a region with exposed and buried steps. Fig. 3.7(a) shows the AFM topography image of the HOPG surface with step edges. Fig. 3.7(b) shows the lateral force image, in which the buried step edge exhibited lower contrast than the two exposed step edges. All steps were single layer.

Fig. 3.8(a) shows the line profiles of the lateral force from forward and backward scans measured with the blunt tip. We observe the friction peaks at the steps in this case are wider than those measured with the sharp tip, which is another indication of tip bluntness [204]. During backward scans, friction peaks were observed at both exposed and buried step edges, and, similar to the sharp tip, the friction peaks at the exposed steps were 2.6 ± 0.7 (averaged over 10 measurements) times higher than at the buried steps. During forward scans, friction peaks were observed at exposed steps. This observation differed from the measurements taken with a sharp tip, where friction peaks were not observed at steps during forward scans, both here and in previous research [26, 202]. At buried steps, we did not observe friction peaks during forward scans, consistent with our sharp tip results and previous experiments on buried steps [203, 205].

We performed simulations with a blunt tip (truncated hemisphere) scanning

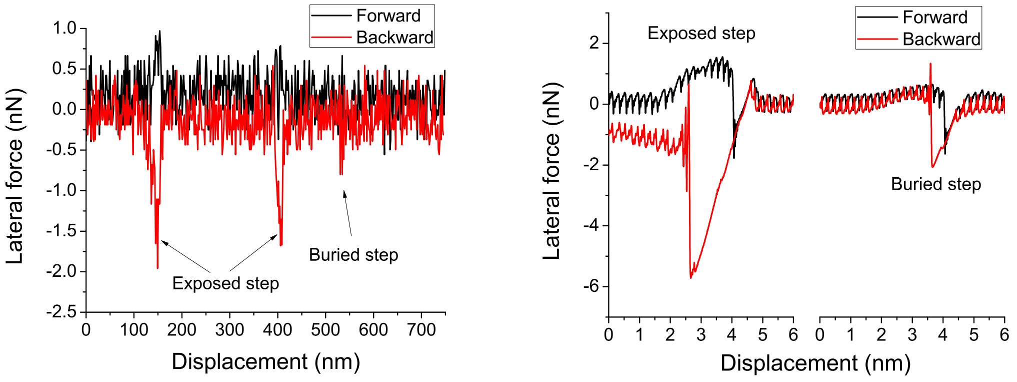

(a) (b)

Figure 3.8: Line profiles of the lateral force at exposed and buried steps obtained using a blunt tip from (a) AFM and (b) MD simulations. Results are displayed such that the tip moves down the step during forward scans (black lines) and up the step during backward scans (red lines).

across exposed and buried steps. Fig. 3.8(b) shows the predicted friction from forward and backward scans. During backward scans, the friction peak at the exposed step was 2.7 times higher than at the buried step. During forward scans, the exposed step friction was 2.5 times higher. At both steps, the friction stepping up was approximately 5 times larger than that stepping down. The quantitative differences between forward and backward scans, and between exposed and buried steps, are consistent with our observations from experiment.

In the previous section, it was shown that friction (a) is always larger at exposed than at buried steps, (b) is larger when the tip moves up as compared to down a step, and (c) increases when a blunt tip is used to measure it. Previous research on stepping down at exposed steps suggested that the trajectory of the tip as it scans over a step can affect friction [202] . The trajectory is the convolution of the surface topography and the tip shape, both of which are varied in this research. Unfortunately, the resolution of our AFM topography images is not sufficient to observe differences between the various cases and, although we can estimate tip size from pull-off measurements, detailed tip shape information is not available. However, the MD simulations provide the level of detail, both with respect to topography and tip shape, necessary to perform the analysis.

Fig. 3.9 (a) shows the trajectory of the two tips as they move over the exposed and buried steps. Note that there is some variation in these trajectories depending on if the tip is moving up or down the step, but we found these differences to be

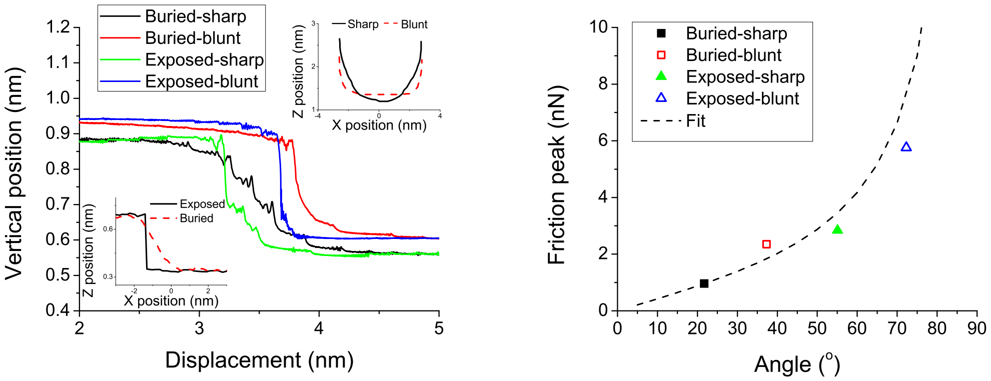

(a) (b)

Figure 3.9: (a) The trajectories of the sharp and blunt model tips as they move over exposed and buried steps. These trajectories are the convolution of the topography of the surfaces and the tip shape, illustrated in the insets. (b) The peak friction force at the step as a function of the angle of the trajectory relative to the horizontal. The dashed line is a fit to equation $F = \tan\theta F_a$.

relatively small. The topography of the surfaces is shown in the lower left inset of this figure and reveals that the surface profile at the buried step is smoother than that at the exposed step. Profiles of the tip shapes are shown in the upper left inset. Both tip shape and surface topography contribute to the tip's trajectory, such that the smoothest trajectory is observed for the sharp tip moving over the buried step. Next, we analyze the observed friction trends in terms of these trajectories, first as the tip moves up the step and then as it moves down.

When the tip moves up the step, the key feature of the trajectory that determines friction is the angle relative to horizontal, θ, through which the tip travels. We characterized θ as the slope of the trajectory at the position where the maximum friction occurred. Fig. 3.9 (b) shows that the peak friction at exposed or buried steps, obtained using a sharp or blunt tip, increased monotonically with this angle. For a given tip (sharp or blunt), the incline angle was smaller at buried steps than at exposed steps, so less lateral force was required to move the tip to the upper terrace. For a given step (exposed or buried), the sharp tip traveled up the step at a smaller angle and, therefore, the peak lateral force was smaller. The incline angle is a measure of the contribution of the normal force F_a to the peak friction at the step F, so we can estimate $F = \tan(\theta)F_a$. We fit the data in Fig. 3.9 (b) to this expression and obtained value of F_a=2.41 nN. Although there is no external normal load applied in the simulation, there is normal force between the tip and substrate due to adhesion. The adhesive force estimated using JKR model was found to be 3.53 nN, which is reasonably consistent with the fit value of F_a. This indicates that the analysis performed here relating trajectory to peak friction through incline angle is appropriate.

The friction associated with the tip moving down a step is associated with trajectory, like step up, but through a different mechanism. In this case, a larger incline angle does not increase the resistance to sliding. However, it has been shown in previous studies that an energy barrier (the Schwöebel barrier) occurs at atomic steps and this energy barrier can increase friction at a step down [26, 28, 31, 202]. The Schwöebel barrier arises from the lower coordination of atoms at the step edge which leads to enhanced interaction energy with, in this case, the atoms in the tip. Here, we characterized the energy barrier as the difference between the maximum potential energy of the tip as it moves down the step and the its energy while scanning on a flat terrace. Fig. 3.10(a) shows the potential energy of the sharp and blunt tips as they scan across the exposed and buried steps, with the energy barrier illustrated for one case. As shown in Fig. 3.10(b), the peak friction the tip experienced at the step increased monotonically with the magnitude of the energy barrier. This is reasonable because a larger force is required to overcome a higher energy barrier. We observed that the energy barrier was much larger at exposed steps than at buried steps, consistent with the larger friction at exposed steps. Also, the energy barrier was larger with a blunt tip than with a sharp tip and, therefore, a higher friction peak was observed with the blunt tip.

Our previous simulations of exposed graphite steps [202] suggested that the trajectory of the tip (Fig. 3.9) can be correlated to the energy barrier. To relate trajectory to energy, we identified the maximum separation distance between the tip and substrate during scanning. This was quantified by calculating the minimum distance between the bottommost atom of tip and the top layer atoms of the substrate at each point along the trajectory and then finding the maximum value of this minimum distance. Fig. 3.10(c) shows the energy barrier increases with maximum separation distance. This is reasonable since the energy barriers at the steps have been shown to be dominated by dispersion and dispersion energy decays as R^{-6} with the interatomic distance [202]. In other words, geometrically close contacts between tip and substrate are favored and the increased separation between tip and substrate gives rise to a high energy barrier. The maximum separation distance was greater at exposed steps than at buried steps, and greater for the blunt tip than the sharp tip, consistent with the observation of a larger energy barrier and higher friction peak for exposed steps and the blunt tip. Therefore, our simulations revealed that the type of steps and the tip bluntness affected the trajectory of the tip, which determines the potential energy, and thus the frictional behavior.

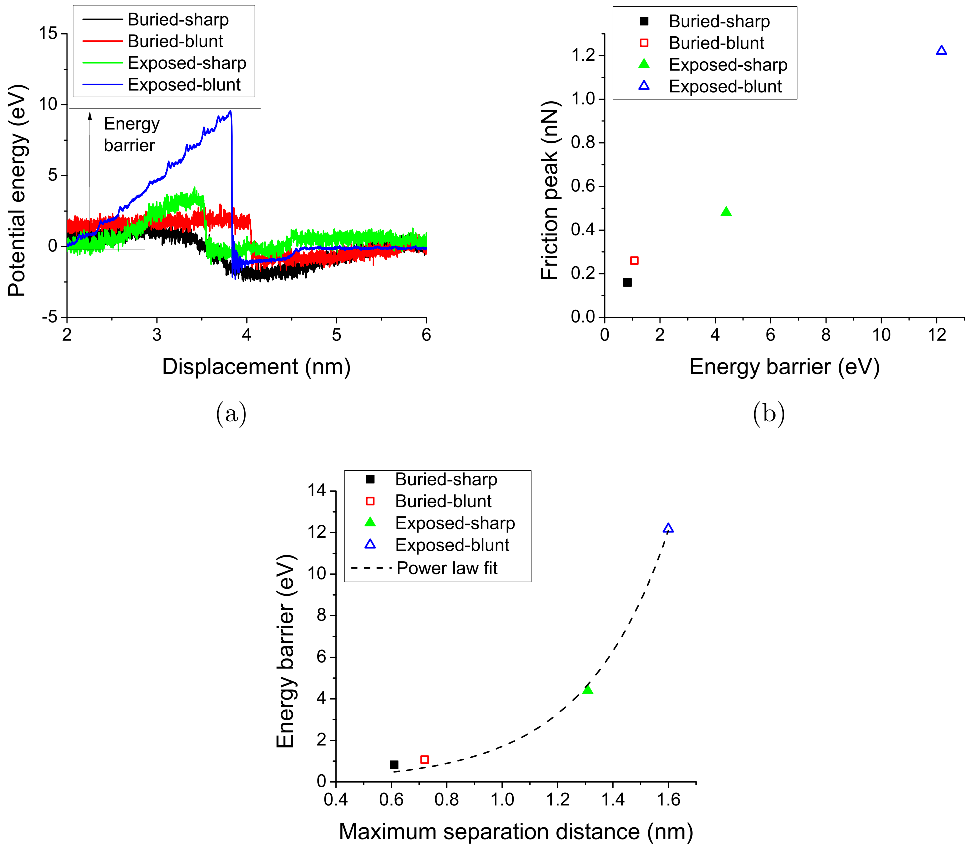

(a) (b)

(c)

Figure 3.10: (a) The potential energy of the tip as it moves down the step where the energy barrier is identified as the difference between the maximum energy and the energy on a terrace. (b) The friction peak at the step as a function of the energy barrier. (c) The energy barrier as a function of the maximum separation distance where the dashed line is a power law fit to the data.

3.2.4 Conclusion

AFM measurements and MD simulations were used to investigated the origins of friction at exposed and buried graphite step edges. To our knowledge, this is the first fully atomistic simulation of buried steps or their friction. The experiments and simulations revealed distinct friction behavior as the AFM tip scanned up or down the exposed and buried steps. We also observed that tip bluntness affected these results. With a sharp tip scanning up the step, friction peaks were observed at both exposed and buried steps, and they were consistently higher at the exposed steps. However, when the sharp tip scanned down the step, friction peaks were either not observed (experiment) or very small (simulation) at either type of step. With a blunt tip, trends similar to the sharp tip were observed for step up scanning. However, stepping down, the blunt tip exhibited enhanced friction, and it was larger at the exposed step.

The MD simulations provided a means of analyzing these friction trends in terms of the trajectory of the tip, which was recognized to be the convolution of the graphite surface topography and the tip shape. The buried step and the sharper tip resulted in smoother trajectories. In the case of moving up a step, the angle of incline of the trajectory at the step determined how much of the normal force contributes to frictional resistance to sliding. Since there was no external load applied, the normal force was due to adhesion between tip and substrate. Moving down a step, the connection between trajectory and friction is an energy barrier at the step whose magnitude increases with the increasing distance from the step to the tip as it steps down. This distance was smaller for smoother trajectories and so explained the smaller energy barrier and lower friction at buried steps and for the sharp tip. Thus, the smoothness of the trajectory of the tip in the simulation was related to friction, albeit through different mechanisms when scanning up or down. Since the observed friction trends were consistent in the simulations and experiments, it is feasible the explanations provided by the simulation are applicable to the experimental measurements as well. Overall, this study is significant for the development of a fundamental understanding of the friction mechanisms on graphite and other layered materials.

Chapter 4

NANOTRIBOLOGY UNDER EXTREME CONDITIONS

Solid lubricants, such as 2D materials (graphite, molybdenum disulfide, boron nitride) and soft metals/metal alloys, are useful for lubricating machine components that operate under extreme conditions, i.e. very high/low temperatures, very fast/slow sliding speeds, and under vacuum or humid air conditions. In this section, we investigated the tribological performance of solid lubricants under extreme conditions by characterizing friction across a wide range of sliding speeds and temperatures under ambient and vacuum conditions. The overall goal is to understand friction due to different operating conditions and enable the enhanced performance of nanoscale mechanical components as well as the development of next generation devices.

4.1 Effect of Environment on Atomic Friction at Graphene Step Edge

4.1.1 Introduction

Currently, most experiments, simulations, and theoretical studies of atomic friction on graphite/graphene have focused on ideal, atomically flat surfaces [199, 210, 211]; such idealizations may not reflect the topography of many practical surfaces. A specific example of a non-ideal feature ubiquitous to crystal surfaces is a step edge. It has been found that lateral forces change locally when nanoscale tips slide across step edges [25–29, 212]. In atomic-scale studies of surface steps, the chemistry and stability of atomic steps are strongly influenced by the environment. For example, atomic steps on ionic crystals become mobile in the presence of water vapor [213]. Although not mobile, the chemical potential of atoms at graphite (multilayer graphene) steps are also strongly influenced by the environment [214]. Thus, the environment could significantly affect friction. Furthermore, recent studies have shown that atomic friction on flat surfaces is also strongly influenced by the presence of water through the formation of a meniscus at the tip-sample contact [215], suggesting that the environment could also influence the friction force occurring at atomic steps and other defects. However, clear evidence for this has not yet been established in the literature: in two specific atomic friction studies of steps on graphite, higher friction at surface steps was observed in both humid air [28] and ultra-high vacuum (UHV) [27], despite the different environmental conditions.

In addition, the environment strongly affects the wear of graphite at macroscopic scales [216]; links to nanoscale behavior to explain this are lacking.

Here, we address the influence of the environment on atomic-scale friction to understand the mechanisms that govern friction at graphene step edges and to address seemingly divergent literature results of atomic-scale studies at step edges where friction behavior was independent of the environment. We study this environmental effect using fully atomistic MD simulations in a system that match the experiments in terms of sample material, tip size, compliances, and presence/absence of adsorbates. Comparison between simulation and experiment (performed by Dr. R.W Carpick's group) enables a more complete understanding of the lateral force response.

4.1.2 Methods

The fully atomistic MD model mimicked the apex of an AFM tip scanning over a graphite step edge having a zigzag termination, and is graphically illustrated in Fig. 4.1 (e). Although this termination affects electronic properties [217], these are not captured in atomistic simulations and, therefore, no edge termination effect on friction was observed in these simulations. Model hemispherical tips with radii between 2 and 8 nm consisting of carbon atoms in a diamond structure were used. To match the compliance of the AFM system, the tip was connected by a harmonic spring to a support. The spring stiffness was $k = 8$ N/m in the directions parallel to the plane of sliding. To scan, the support was moved laterally with a constant speed of 4 m/s. While this exceeds the experimental scan speed by 7 orders of magnitude (a problem endemic to most AFM-MD studies), the model predictions are still meaningful. In previous work we showed that, although caution is required when comparing inertial or dynamic effects, energetic parameters extracted from MD simulations with reliable potentials matched in every other respect to AFM experiments [199]. The top three layers of the tip acted as a rigid body on which a constant normal load was applied. The substrate consisted of three graphene layers with the bottommost layer fixed. In certain simulations, water molecules were placed in the vicinity of the tip-substrate contact. A Langevin thermostat was applied to all atoms whose positions are not constrained to maintain a simulation temperature of either 10 K or 300 K. The boundaries were periodic in the sliding plane, and the boundary in the surface-normal direction was formed by the fixed bottom layer of the substrate and the rigid body of atoms at the top of the tip. Atoms within the tip and substrate interacted via the AIREBO [200] potential. The TIP4P potential was used for the water molecules [218], and the Lennard Jones potential was used to model interactions between graphite layers ($\epsilon = 0.00384$ eV, $\sigma = 0.34$ nm), between the tip and graphite ($\epsilon = 0.00384$ eV, $\sigma = 0.34$ nm), and between water molecules and the tip/substrate ($\epsilon = 0.006499$ eV, $\sigma = 0.319$ nm).

4.1.3 Results and Discussion

In previous studies [25–29, 212], two types of friction behaviors at a step edge were observed: geometric friction-the lateral force peak at a step edge is negative during both forward (step down) and reverse (step up) scanning, and enhanced friction-the lateral force peak at a step edge is positive during forward scanning but negative during reverse scanning. Figure 4.1 (A) shows a lateral force profile for a sliding tip in a vacuum environment. Here, a positive lateral force in the forward scanning direction and a negative lateral force in the reverse direction correspond to a resistive force that impedes the tips motion. a negative lateral force in the forward scanning direction and a positive lateral force in the reverse direction correspond to an assisting force. The lateral force peak at the step edge is negative in both the forward and reverse directions, characteristic of geometric friction. Analysis of the dependence of friction force with normal force in Figure 4.1 (C) shows that a slightly higher amount of dissipation is observed at the step edge compared to on the terrace. Also, the peak lateral force in both forwards and reverse direction exhibit a negative correlation with normal force. Comparable results were obtained as the tip radius was varied from 2 nm to 12.5 nm, always showing geometric friction.

In previous experimental studies, enhanced friction at atomic step edges was attributed to the "Schwoebel Barrier" [26, 28]. The original papers by Schwoebel presents a theory that predicts the probability with which steps on crystal surfaces will capture atoms diffusing on the surface [197, 198]. Most experimental work mentioned above applied this theory and developed a static 2D model to illustrate the presence of an energy barrier at the step and the effect of atomic interaction strength on its size. Similarly, we varied the interaction strength between the atoms in the tip and the atoms in the graphene from $\epsilon =$ 0.0001 to $\epsilon = 0.016$ eV in our MD simulation. However, we found that this parameter did not, with any combination of tip size and shape, affect the transition from geometric to enhanced friction. However, MD simulations confirm this modified potential at the step edge is responsible for the slight increase in frictional dissipation observed at the step edge, which changes slightly in tandem with the enhanced potential at the step edge.

The previous experimental results [31] suggested that the adsorption of water or other contaminants at the step can cause enhanced friction. To capture this effect in the model, we introduced water molecules into the simulation near the tip-substrate contact. Figure 4.1 (B) shows the lateral force profile when water molecules are placed between the tip and the surface (graphically illustrated in Figure 4.1 (F)). Including water in the simulation resulted in the appearance of enhanced friction at the step edge similar to experiment. Figure 4.1 (D) shows the dependence of friction on normal force in this configuration. The trends in the variation of peak lateral force and friction on load is similar in our simulation and previous experimental results [31].

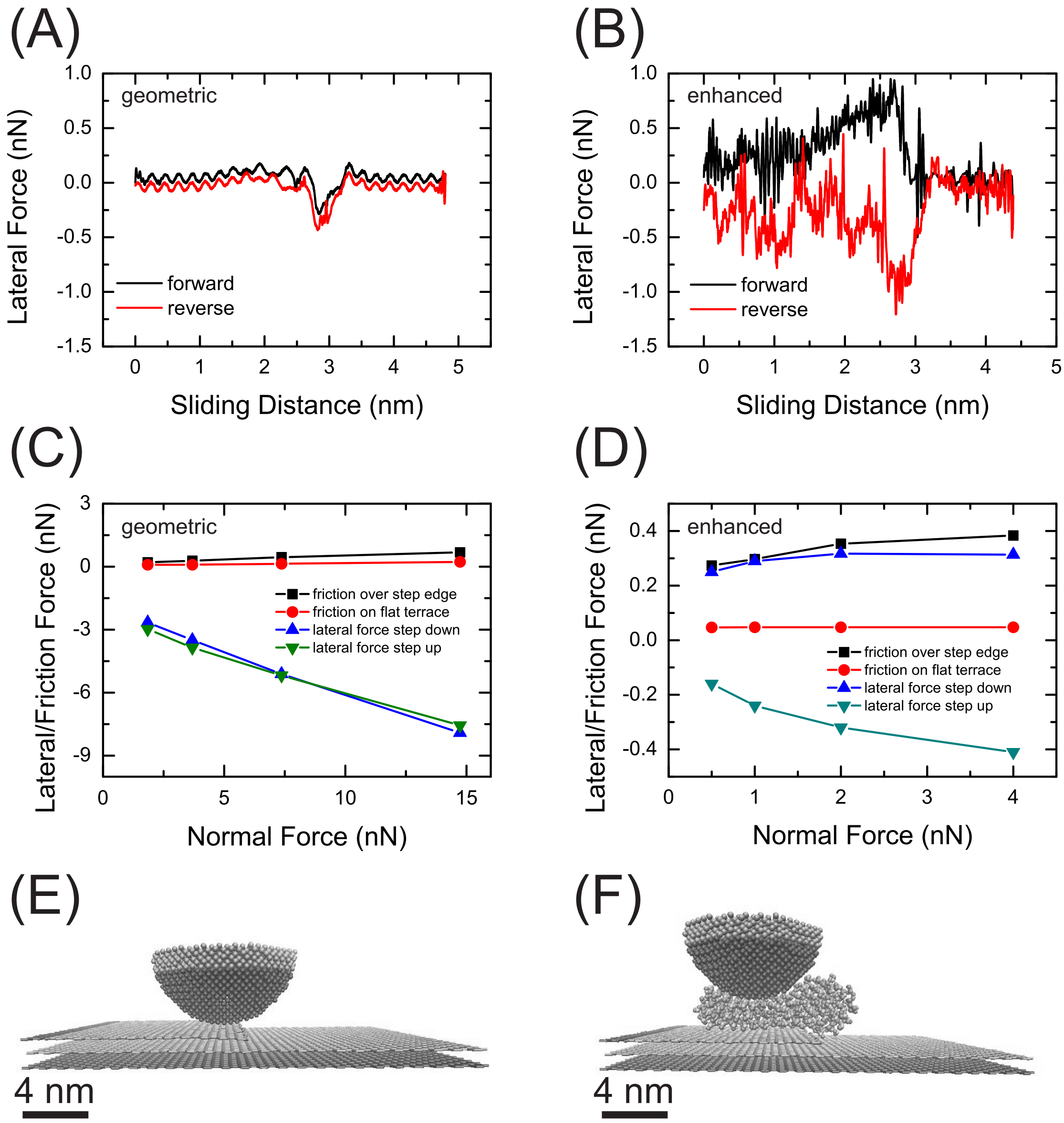

Figure 4.1: MD simulation results of step friction on graphite. Friction line profile acquired under (A) vacuum conditions (normal force = 0 nN) and (B) dry nitrogen conditions, having two layers of water (normal force = 0 nN). The load dependence of friction measured (C) in vacuum and (D) with water. Illustrations of the 2 nm radius tip sliding over the graphite substrate (E) in vacuum and (F) with water. (A), (B), (E) and (F) are from simulations conducted at 300 K. The load dependence results in (C) and (D) were acquired at 10 K.

All the experiments and simulations in HV conditions discussed previously resulted in geometric friction, regardless of the tip size. However, Steiner *et al.* showed that it was possible to switch from geometric friction to enhanced friction in vacuum by wearing the tip apex. Several studies of tip wear have shown that tip wear often results in a flattened tip apex, rather than an increase in the tip radius [219,220]. To examine this effect, we studied truncated tips in MD simulation, which are created by removing successive layers of atoms from the apex of the tip. The lateral force profile and load dependence (see supplementary materials) show the hallmarks of enhanced friction at the step edge consistent with the suggestion that a worn tip can increased the frictional dissipation at the step edge [26].

The MD simulations reproduced the experimental observations that enhanced friction is observed in the presence of humidity/water [31] and due to tip wear as suggested by Steiner *et al.* [26]. We analyzed the simulations to understand the relationships between atmosphere, geometry, and friction and identify two key mechanisms: the trajectory the tip takes over the step edge and the presence of water. In vacuum, friction at the step is determined by the trajectory of the tip. For sharp tips, the trajectory as the tip moves down a step is relatively smooth following the curvature of the tip apex. However, for worn or blunted tips, the apex curvature cannot smooth the trajectory and there is a sharp drop off as the tip moves down the step. This abrupt transition appears to result in additional resistive forces; the relationship between trajectory and resistance may in fact be understood in terms of the "Schwoebel-Ehrlich Barrier" which was proposed to be the cause of frictional resistance at a step edge in previous work [26, 28]. However, in MD simulations of spherical tips, enhanced friction could not be reproduced regardless of the strength of the Schwoebel-Ehrlich Barrier, or the increased strength of the potential barrier at the step edge. We believe that the small additional friction that was observed in the case of geometric friction is a result of the Schwoebel-Ehrlich Barrier, demonstrating the small influence it has on atomic friction studies, unless the tip apex is flattened. However, under ambient conditions, the effect of water/contaminants adsorbed at the step dominant the frictional behavior. When water is present, the trajectory is relatively unaffected by tip shape, but the water itself smoothens the trajectory the tip takes over the step. The smoothened trajectory reduces the amount of assistive force observed in the step down direction. On the other hand, water preferentially sticks to the step providing significant resistance to sliding either up or down the step. The combination of the reduction of the assistive force and the increased resistance to sliding over the step results in enhanced friction.

4.1.4 Conclusion

We have shown that, although the friction behavior on graphite terraces is not strongly affected by the environment, the presence of even a small amount of water at atomic step edges significantly increases friction. Separation of the frictional dissipation observed as the tip slides from the terrace over the step and the instantaneous lateral forces measured during this transition have uncovered the mechanism by which a sliding, nanoscale asperity experiences additional friction at atomic steps on graphite. The lateral force at a step edge on clean graphite surfaces is slightly more dissipative due to the effect of the Schwoebel barrier on the tip, but far larger friction occurs at step edges when water is adsorbed at the step.

4.2 Speed Dependence of Atomic Friction on Gold Substrate

4.2.1 Introduction

Atomic stick-slip sliding is an intriguing and fundamentally significant phenomenon, relevant to the understanding of elementary mechanisms of friction [221–223]. First observed using AFM, atomic stick-slip often occurs when two clean surfaces, at least one of which is crystalline, slide in relative motion [224]. Reduced-order models, such as the Prandtl-Tomlinson (PT) model, reproduce a remarkable number of features of atomic stick-slip sliding [225, 226]. These models explain the process as the build-up and then unstable release of energy in sufficiently compliant elastic elements of the system while traversing a periodic energy landscape (corresponding to the surface lattice sites) with sufficiently deep local energy minima. Upon slip at the maximum lateral force (the static friction force), physically unspecified dissipation causes the interface to stop slipping at the next lattice site (or sometimes multiples thereof [227]) and the process repeats. The PT model has recently been extended to include thermal energy, leading the prediction that static friction will increase with decreasing temperature and increasing scanning speed (the speed at which the sample is translated with respect to the fixed end of the cantilever). The velocity dependence friction has been studied using AFM [31, 93, 228–230] although in only one case [228] was stick-slip behavior actually resolved. Although not all findings from those reports agree with each other, the trend of increasing friction as a function of velocity is explained as thermal energy assisting in overcoming local energy barriers: faster scanning reduces the time in which thermal energy has to provide this assistance and so static friction is higher. However, validating models quantitatively, understanding how energy is dissipated, and describing the atomic-level processes by which slip occurs dynamically at the interface are beyond the capabilities of the PT model and are challenging because of the inaccessibility of the buried interface in experiments. Therefore, stick-slip is often considered using MD simulations, which provides a means of directly observing atomic interactions within the interface [23, 228]. However, the scanning speeds of AFM and MD have yet to overlap. This issue results from: (a) the femtosecond time steps used in standard MD to capture atomic motion which limit the time duration that can be simulated, constraining the simulations to high scanning speeds ($> 10^{-1}$ m/s); and (b) the far slower scanning speeds ($> 10^{-5}$ m/s) of AFM experiments which are typically constrained by mechanical and data acquisition limits. This discrepancy limits the ability to reliably compare results from AFM and MD.

Here, we close the gap between experiments and simulations for the first time by using parallel replica dynamics (PRD) to slow down MD simulation scanning speeds, and by improving the AFM apparatus to obtain higher experimental scanning speeds while resolving stick-slip behavior in both. Experiments in this study were performed by Dr. Robert W. Carpick's group. Other parameters, namely environment (vacuum), materials (a gold sample and a SiO_2 tip), contact area, temperature, normal and lateral stiffnesses, and load, are also matched as closely as possible. We observe single stick-slip events across 10 orders of magnitude of speed. However, the mean friction force at the same scanning speed is consistently higher in experiments than in simulations, and the trends fit to the thermally activated PT (PTT) model do not overlap. To identify sources of the discrepancy, we analyze the measured and predicted friction in terms of the PTT models physical parameters.

4.2.2 Methods

MD simulations consisted of the apex of an amorphous SiO2 AFM tip scanning over a Au(111) surface. The gold substrate had dimensions of $10 \times 10 \times 5$ nm^3 (length × width × thickness). The atoms in the bottom 1 nm of the substrate were fixed and the positions of the rest of the atoms in the substrate were unconstrained. The AFM tip was modeled as a truncated cone with a top surface diameter of 3 nm, bottom surface diameter of 2 nm, and 3 nm height. Amorphous SiO2 was obtained by quenching a block of crystalline SiO2 and then cutting the desired tip shape from the block. The topmost atoms in the tip were treated as a rigid body that was subject to a 0 nN external normal load and connected by a harmonic spring to a support that moves laterally at a constant speed. A Langevin thermostat was applied to the free atoms maintained a temperature of 300 K. In all simulations (MD and PRD), the inter-atomic interactions within the tip and substrate were described via the Tersoff [181] and Embedded-Atom Method (EAM) [231] potentials, respectively, and the long range interactions between tip and substrate were modeled using the Lennard-Jones (LJ) potential. The LJ parameters were calibrated by confirming that the work of adhesion (0.042 J/m^2) calculated from the simulation was consistent with the value of 0.05 ± 0.03 J/m^2 that measured experimentally. The simulations were performed using LAMMPS simulation software [232].

4.2.3 Results and Discussion

Figure 4.2 shows the mean experimental friction vs. scanning speed for both tips, with an inset showing a friction loop acquired at a scanning speed of 5.8 m/s. Single atomic stick-slip events were resolved up to speeds ∼10 μ/s, after which the number of data points per event were insufficient. For both data sets, the expected near-logarithmic increase in friction with speed is observed from the minimum scanning speed (∼1.7 nm/s), until a plateau occurs at ∼1-10 μm/s. The data was fit to the PTT model [233, 234] using the equation:

$$\frac{1}{\beta k_B T}(F_c - F_L)^{3/2} = \ln \frac{v_0}{v} - \frac{1}{2}\ln(1 - \frac{F_L}{F_c}) \tag{4.1}$$

where F_L is the mean static friction force, v is the scanning speed, T is the temperature, k_B is Boltzmanns constant, F_c is the mean static friction force at zero kelvin, β is a parameter related to the shape of the lateral potential profile which governs the rate of increase of friction with speeds at low speeds, and v_0 is a characteristic speed given by $v_0 = (2f_0\beta k_B T)/(3k_{tot}\sqrt{F_c})$, where f_0 is the characteristic slip attempt frequency, and ktot the total lateral stiffness of the system [16,18,19]. For a sinusoidal potential with periodicity a and barrier height E_0, $F_c = \pi E_0/a$ and $\beta = 3\pi\sqrt{F_c}/(2\sqrt{2}a)$.

The three fitting parameters, β, f_0, and F_c, were obtained by fitting the data to the PTT model. F_c was determined first as an average of the data points in the plateau. Then β and f_0 were fit to the data at all scanning speeds with their resulting values (Fig. 4.2, caption) differing between the two tips by factors of 1.9 and 6.5 respectively. These are reasonable given the differences in the two tip sizes and shapes.

Complementary simulations consisted of the apex of an amorphous SiO_2 AFM tip scanning over a Au(111) surface with dimensions of $10\times10\times5$ nm^3 (length × width × thickness). The key achievement here is the implementation of PRD, necessary to increase the duration of the simulations thereby decreasing the scanning speeds [235, 236] with a 0.1 nm transition criterion and 10 ps between transition checks. Speeds as low as 25 μm/s were achieved. The PRD method was optimized by the use of the truncated cone-shaped tip as it was highly stable, minimizing the number of atomic transitions not related to slips. The effective lateral contact stiffness of the system was set to 5.38 N/m, within the error of both experimental values. A Langevin thermostat was applied to unconstrained atoms in the system, which were maintained at a temperature of 300 K.

The simulation-predicted mean friction force is shown in Figure 4.3. Significantly, the slowest scanning speed obtained from PRD simulations (25 μm/s) is smaller than the fastest speed of experiments (∼580 μm/s). Overlapping datapoints at 0.1, 0.2 and 0.5 m/s from MD and PRD validate the PRD simluations. MD simulations were run at 0.5 K to mimic sliding friction without thermal activation; the resulting constant friction force plateau at 2.560.02 nN was used as F_c in the PTT model fit. Above scanning speeds of 4 m/s, friction increased rapidly with speed, deviating well above the predicted plateau. The unphysically high friction at high speeds is consistent with previous observations [37]. The present simluations reveal it is associated with surface wear, quantified empirically as the the root mean square surface roughness, which was observed to increase dramatically at these speeds. These high speed data were thus excluded from subsequent analyses. Fitting the simulation data up to 1 m/s then yields $\beta = (2.9\pm0.2)\times10^5$ N$^{3/2}$/J, and $f_0 = 120\pm30$ GHz.

To better compare experiment and simulation, the AFM data from Tip 1 (black squares) and the MD/PRD data (diamonds and blue circles) are plotted together in Figure 4.4. The clearly shows that while the speed gap between simulations and experiment has been closed, a significant difference exists despite the

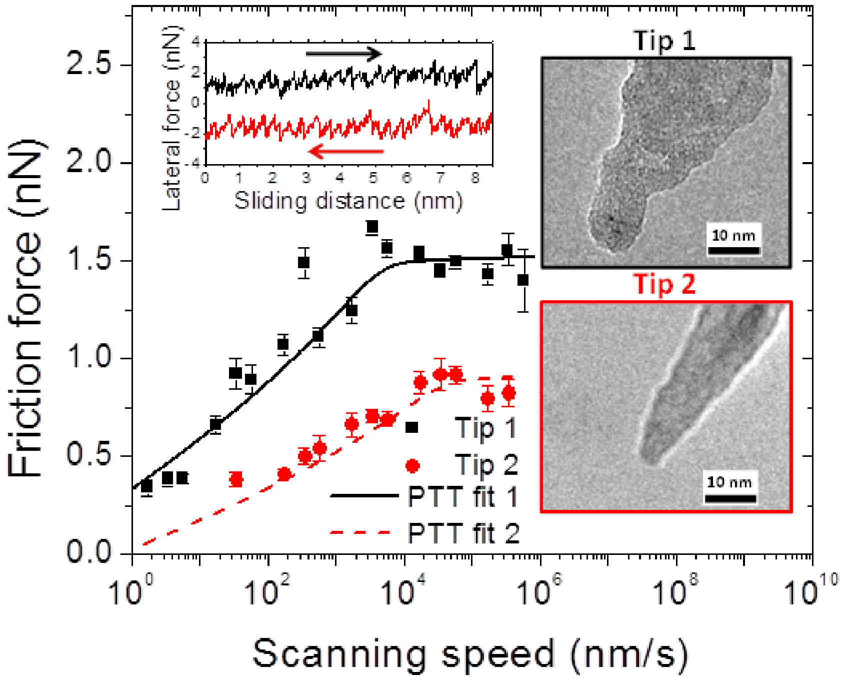

Figure 4.2: Friction force vs. scanning speed for Tip 1 (black squares) and 2 (red circles). The solid line (Tip 1) and dashed line (Tip 2) are fits of the PTT model to the data, which yield, for Tip 1: F_c= 1.5±0.2 nN, β = $(4.8\pm2.0)\times10^5$ $N^{3/2}/J$, and f_0 = 108±42 kHz; and for Tip 2: F_c = 0.9±0.2 nN, β = $(2.5\pm0.3)10^5$ $N^{3/2}/J$, and f_0 = 700±200 kHz. The normal applied force is 0.0±0.2 nN in both data sets. Error bars represent the standard deviation in the calculated mean friction force. Right insets are pre-mortem TEM images of the tips used for data acquisition. Top inset shows a friction loop acquired with Tip 1 at ~5.8 μm/s; atomic stick-slip pattern can be clearly resolved corresponding to scanning along the [110] direction. Arrows indicate the scan direction. AFM experiments in this study were performed by Dr. Robert W. Carpick's group.

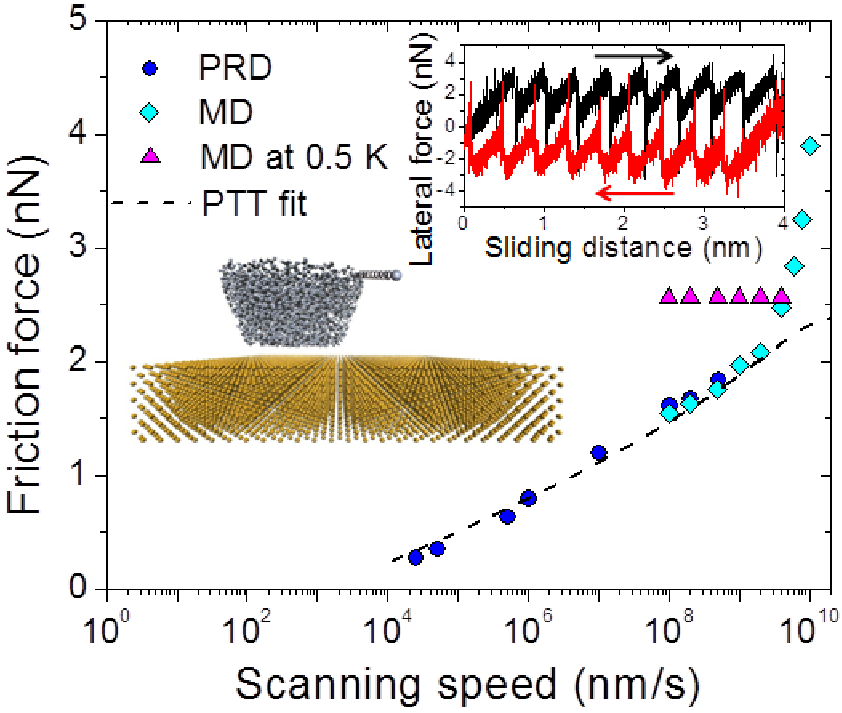

Figure 4.3: Friction force as a function of scanning speed from MD at 300 K (cyan diamonds) and 0.5 K (purple triangles), and PRD (blue circles) at 300 K. Dashed lines indicate fits of the PRD data to the PTT model using a value of F_c from the simulations at 0.5 K of 2.56±0.02 nN, yielding $\beta = (2.9\pm0.2)\times10^5$ $N^{3/2}/J$, and $f_0 = 120\pm30$ GHz. Left inset: model of the SiO_2 tip and the Au(111) substrate. Top right inset: a friction loop showing clear atomic stick-slip along the [100] direction. Arrows indicate the scan direction. Experiments in this study were performed by Dr. Robert W. Carpick's group.

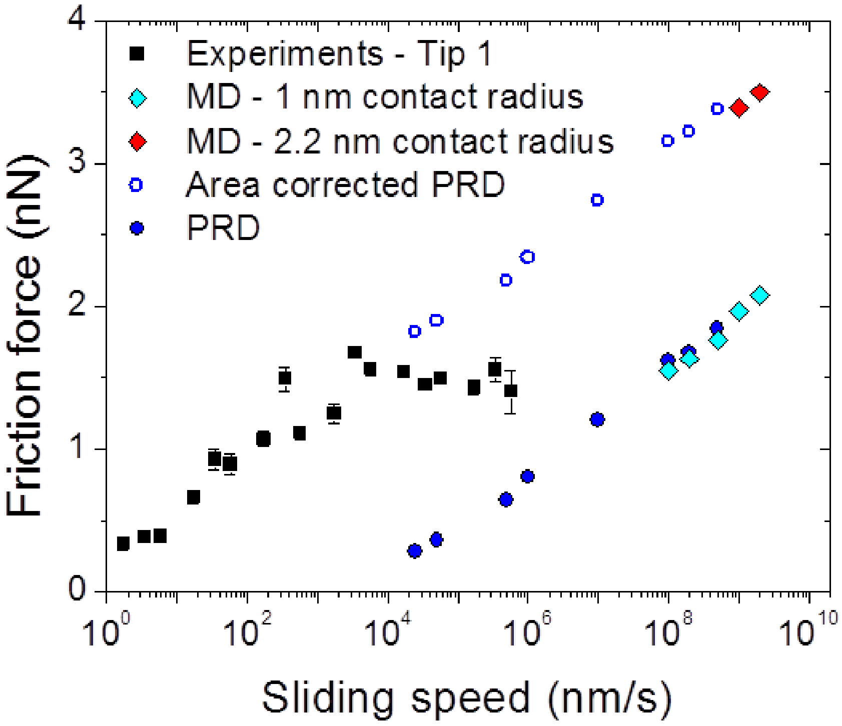

Figure 4.4: MD (cyan and red solid diamonds), PRD (blue solid circles), and experimental results from Tip 1 (black squares) plotted together. MD predictions are reported for 1 nm (cyan diamonds) and 2.2 nm (red diamonds) contact radii; the relationship between F_c and contact size is also used to extrapolate the PRD data (blue hollow circles)

optimally matched conditions. Comparing β, F_c, and f_0 fit values provides clues to the origins of this difference. The β values are reasonably consistent (2.9×10^5 $N^{3/2}/J$ from simulation, and 4.8×10^5 $N^{3/2}/J$ and 2.5×10^5 $N^{3/2}/J$ from experiments). The magnitude of F_c from simulation (2.56 nN) is somewhat larger than the two experimental values (0.85±0.18 and 1.5±0.2 nN), but is the same order of magnitude. Moreover, the value of f_0 from simulation (120±30 GHz) differs by orders of magnitude with those from experiments (108±42 kHz and 700±200 kHz). The remainder of this manuscript examines the root causes of the differences in F_c and f_0, which may explain the difference in the predicted and measured friction.

The discrepancy in F_c may have three origins: differences in tip shape, scanning direction, and contact area. First, a truncated cone-shaped model tip was used to optimize the PRD simulations; this differs from the hemispherical experimental shape indicated by TEM images (Figure 4.2, inset). The influence of tip geometry was investigated by simulating a hemispherical tip with the same approximate contact radius as that of the truncated cone; these simulations were performed only at fast scanning speeds (i.e. using MD, not PRD). The change to a hemispherical model tip increased friction only slightly ($\sim$6%), an amount within the uncertainty of the contact mechanics calculations, indicating that geometry cannot explain the experiment-simulation difference. Second, the scanning direction was [110] in the experiments and [100] in the simulations. However, MD simulations run over a range of scanning directions produced only a 4% change in mean friction force. Therefore, scanning direction is also not likely to be responsible for the discrepancy. Finally, we evaluated the effect of contact area. Recall that the simulation area was designed to match a value estimated from experiments, where that estimate was based on a continuum model, a limitation imposed by being unable to directly measure contact area experimentally [93]. To test the sensitivity of F_c to contact area, simulations with tips having different circular contact radii were conducted. Friction increased linearly with contact area, consistent with previous theoretical [228] and experimental observations [237,238]. The linear relationship between friction and contact area suggested that increasing the model simulation contact radius from 1 nm to 2.2 nm should result in very good matching between simulation and experiment (Figure 4.4, hollow blue circles). This contact radius (2.2 nm) is still close to the experimental estimation, and certainly feasible given the limitations of using a continuum model to describe nanoscale contact [94,97] and the large error associated with determining the tip radius. This suggests that the contact area may contribute to the observed difference in friction between experiment and simulation. However, such a shift will not resolve the complete disagreement in the onset speed of the plateau.

The experiment-simulation discrepancy can only be fully resolved by addressing the difference in attempt frequency, f_0. This difference may be due to the difference in mass (inertia), as discussed previously [37]. Specifically, the tip apex in MD/PRD simulation is only comprised of a few thousand atoms, significantly smaller than the AFM tip or the cantilever, both of which exhibit thermal vibrations that can produce slip attempts. For a harmonic system, the attempt frequency will be related to the structures effective mass, m, by $f_0 = \frac{1}{2\pi}\sqrt{\frac{k}{m}}$, where k is the spring stiffness. This expression, with the fit values of f_0 from experiment and simulation and the known simulation tip mass, predicts an effective experimental tip mass of $m_{exp} \sim 10^{-11}$ kg, corresponding to a volume of $\sim 4 \times 10^{-15}$ m^3 (assuming a density of 2.6 g/cm^3 [239]). While it is not exactly known how much of the tip actually contributes to the thermally activated friction, the calculated volume is consistent with that of a real AFM tip, estimated to be $\sim 7 \times 10^{-16}$ m^3 based on the TEM tip images and the use of a method of disks from the tip profile [28]. We cannot directly test this using MD simulations given the size-scale limitations of the model. However, simulations of tips scanning at 1 m/s with artificially increased atom masses showed that friction increased with mass, consistent with our numerical solutions of the PTT model (higher mass reduces f_0; fewer slip attempts per second lead to higher mean friction, similar to the effect of scanning faster). Thus, the small model tip mass provides one explanation for the difference between simulation and experiment.

However, within the range of contact areas, tip masses, and scanning speeds explored in the simulations, the experimentally observed friction plateau is not reproduced. Physically, the plateau represents attaining a high enough scanning speed that available vibrations of the atoms at the end of the tip apex no longer have enough time assist in overcoming the local interfacial potential energy barriers [240]. In the PTT model, only those thermal vibrations of the tip apex are considered; other thermal noise sources, such as thermally induced vibrations of the cantilever, or athermal instrument noise, such as mechanical vibrations of the AFM apparatus and electronic 60 Hz noise, are not included despite the fact that they can also lower the activation barrier to slip by adding energy into the contact [240, 241]. Both athermal and thermal noise sources are inherent in every experiment, but not fully captured in simulations. By applying the master equation method [31], the influence of both noise sources can be captured simultaneously via numerical modeling. In this approach, both noise sources can be specified in the model, with athermal noise vibration amplitudes in experiments calibrated through comparison of their amplitude with respect to thermal noise sources in a Fourier spectrum of cantilever vibrations. This analysis indicates that two transition points can occur: a plateau-like reduction in slope at low speed determined by low frequency instrument noise, and a plateau at high speed due to higher frequency thermal noise [241]. The master equation method was applied assuming a thermal vibration of the cantilever at 200 kHz and an amplitude of 0.20 nm. This amplitude corresponds to a temperature of 1800 K based on the equipartition theorem [242], thus, the noise observed in the experiment is likely a combination of the thermal noise from the AFM cantilever oscillating at its first lateral resonance and athermal noise associated with the mechanical vibrations of the AFM apparatus. This modeling is the only current mechanism by which the low-speed friction plateau observed in experiments and the high-speed friction plateau observed in simulations can be linked.

4.2.4 Conclusion

In summary, the speed dependence of atomic stick-slip friction between silica AFM tip apexes and atomically-flat gold surfaces has been studied using optimally-matched AFM experiments and MD simulations with overlapping scanning speeds. For both experiments and simulations, the friction vs. scanning speed trend matches that predicted for thermally activated slip, but the magnitude of forces and the onset speed of the friction plateau disagree. Analysis indicates that the interfacial potential shape parameters β match well, but vastly different attempt frequencies are at play; differences in the mean athermal friction force F_c may also contribute. The magnitude of the forces can be explained by differences in contact area, but the onset of the plateau requires explaining the discrepancy in the attempt frequency. This can be attributed to noise from the thermal vibrations of the cantilever or other athermal noise sources within the instrumentation.

This study thus bridges the gap between atomic scale friction mechanisms and those observed for real mechanical systems by observing atomic stick-slip over nine orders of magnitude. Across this range, stick-slip is observed to follow the PTT model: the tip resides in and then escapes from local potential energy minima, due to the applied shear force assisted by vibrations. This validates using the rich array of data available from MD simulations to interpret AFM experimental results.

4.3 Temperature Dependence of Atomic Friction on 2D Materials

4.3.1 Introduction

Frictional energy dissipation is particularly important in affecting the performance of microscale and nanoscale devices. While some notable progress has been made in reducing friction and wear in these systems [243, 244], new challenges exist when considering elevated temperature operation of these systems. Higher temperature operation is important for many reasons: some devices need to be able to work in elevated temperature environments (e.g., sensors in combustion systems); suitable high temperature performance of micro or nanodevices would alleviate expensive heat sinking and thermal management schemes [245]; and next-generation hard-disks will involve high-temperature operation, and tribological issues are major challenges for this technology [246]. Temperature dependence of friction is also important for many other engineered systems, such as tip-based thermal lithography methods (which use atomic force microscopy) that involve sliding contact [247], nanoelectromechanical systems (NEMS) which may involve tribological contacts potentially at elevated temperatures, automotive engine tribology [248], and hydraulic fracturing [249–251]. Thus, understanding the effects of temperature on friction is critical for a wide range of applications. Previous studies suggest that friction for many materials can be significantly reduced by increasing the temperature, a phenomenon known as thermolubricity [252–254]. Understanding this has potential to allow it to be used in applications to conserve energy.

Here, MD simulations are carried out to study the temperature dependence of atomic friction on 2D materials, including graphene, MoS_2, and BN. For the first time, temperature dependence of friction on three 2D materials are compared under the same conditions. Friction trends are correlated to the energetics of surfaces, where the energy barrier varies with different types of materials.

4.3.2 Methods

The atomistic model is illustrated in Figure 4.5. In this model, the apex of an AFM tip scanned over bilayer graphene, BN and MoS_2 with zero normal load applied. The bottom layer of each material was fixed. The top three layers of the tip was treated as a rigid body which was connected by a harmonic spring to the support that moves at 1 m/s in the sliding direction. The spring had stiffness of 8 N/m in the horizontal directions, but did not resist motion in the vertical direction (normal to the graphene surface). A Langevin thermostat was applied to the free atoms in the system to maintain a temperature of 300K. The inter-atomic interactions within the tip and graphene, BN and MoS_2 substrates were described via the AIREBO potential [84],the Tersoff potential [122], and the Reactive Empirical Bond Order (REBO) potential [123],respectively, and the long range interactions between tip and substrate were modeled using the Lennard-Jones (LJ) potential

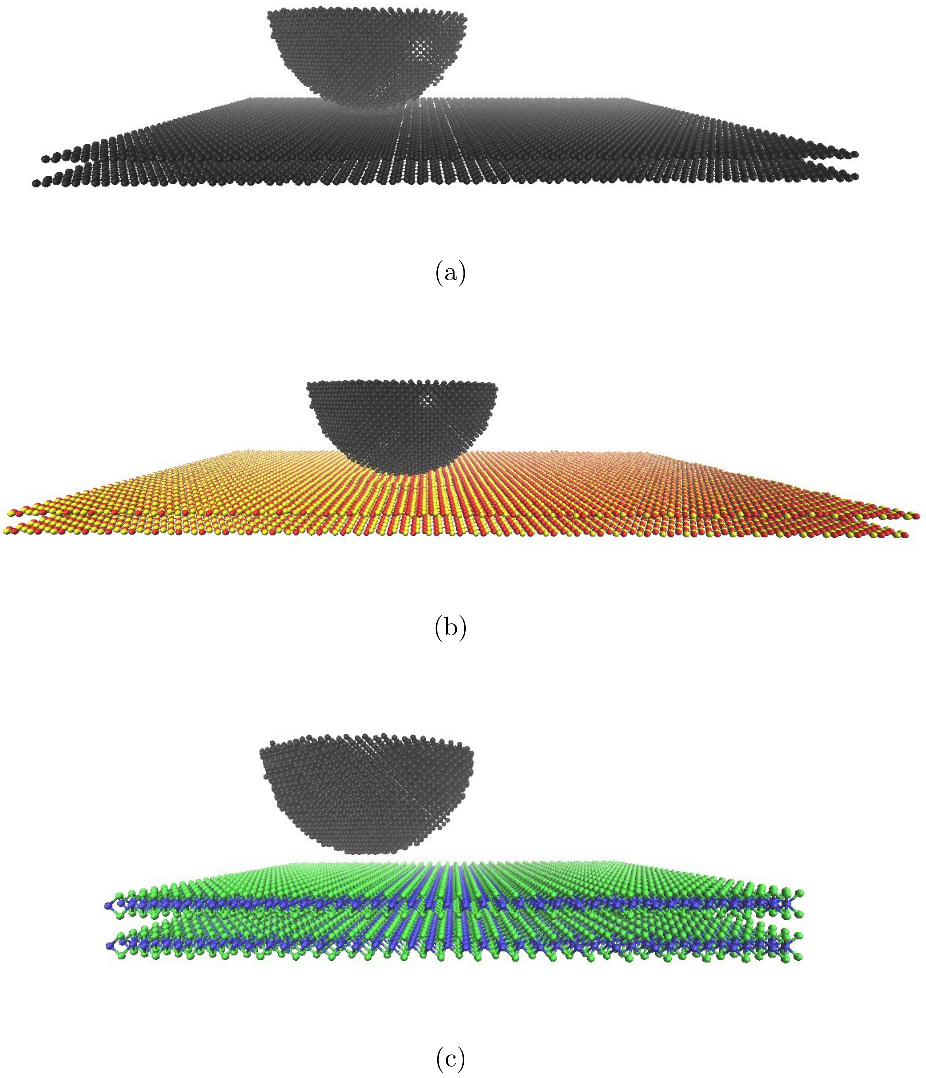

(a)

(b)

(c)

Figure 4.5: Snapshot of an MD simulation of a hemispherical diamond tip sliding on (a) graphene (b) BN and (c) MoS_2.

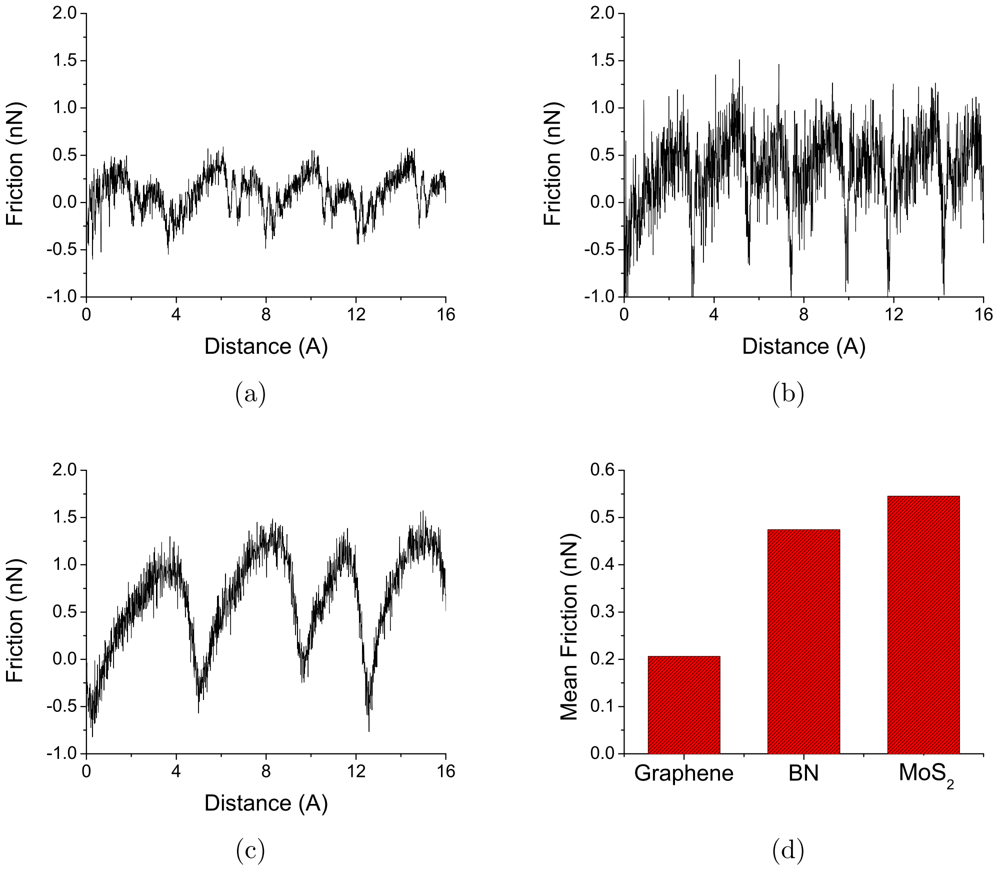

(a) (b) (c) (d)

Figure 4.6: Friction trace on (a) graphene (b) BN and (c) MoS$_2$ surface. (d) Mean friction of three different materials.

with parameters adopted from Ref. [84]. The simulations were performed using the LAMMPS simulation software [105].

4.3.3 Results and Discussion

Figure 4.6 shows the friction trace on graphene, BN and MoS$_2$ surfaces. Stick-slip patterns are observed in all three materials. However, the friction magnitude are different. We characterize the mean friction over 3.2 nm sliding distance, the results are shown in Figure 4.6 (d). Friction is highest on MoS$_2$ surface and lowest on graphene surface.

Figure 4.7 shows the friction predicted at different temperatures. Our results show that friction for all three materials reduces with increasing the temperature,

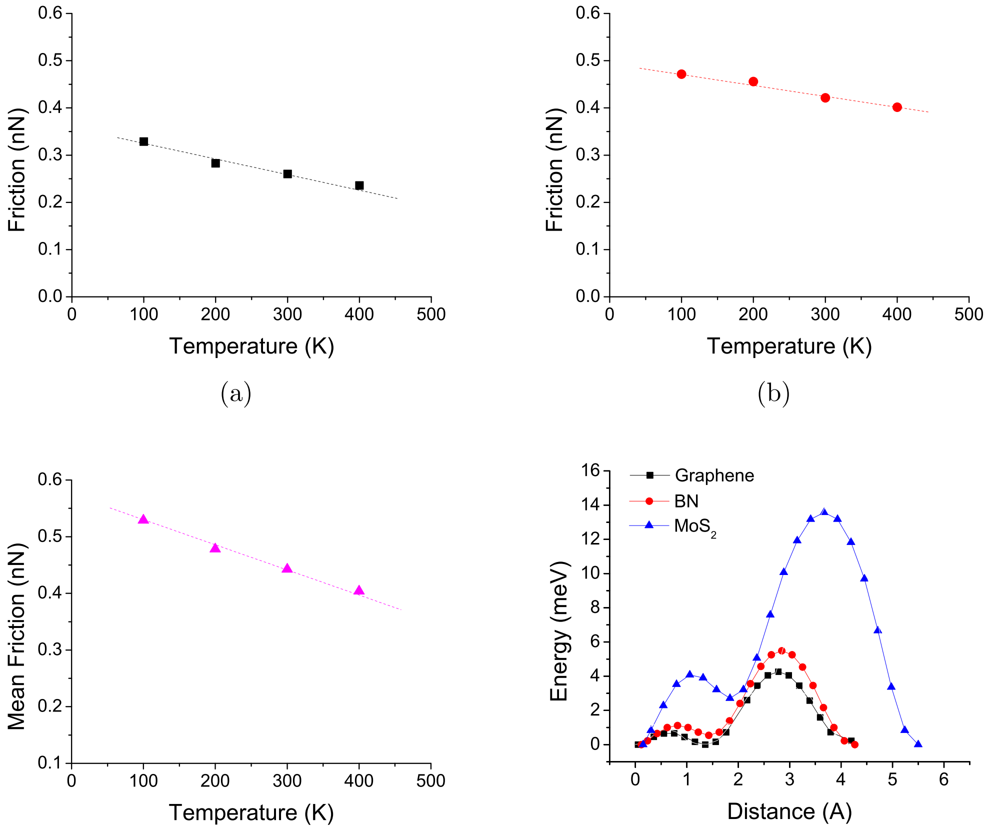

(a)

(b)

(c)

(d)

Figure 4.7: Temperature dependence of friction on on (a) graphene (b) BN and (c) MoS_2 surfaces.(d) Potential energy surfaces on different materials.

a phenomenon known as thermolubricity [252–254]. Thermolubricity is usually explained using thermal activation, where thermal motion assists the sliding process therefore lead to a lower friction. A linear fit was applied to data. The slope of MoS_2 was largest and the slope of graphene was smallest. We believe this phenomena is related to the potential energy surfaces, shown in Figure 4.7 (d). The different energy barriers of three materials could affect the thermal activation process, which need further study to confirm.

4.3.4 Conclusion

MD simulations are carried out to study the temperature dependence of atomic friction on 2D materials, including graphene, MoS_2, and BN. For the first time, temperature dependence of friction on three 2D materials are compared under same conditions. MoS_2 shows the largest friction and highest slope of temperature dependence trends. Friction trends could be correlated to the energetics of surfaces. However, further study are needed.

Chapter 5

ELECTRICAL AND THERMAL TRANSPORT AT NANOSCALE INTERFACE

Nanotribology is truly interdisciplinary. It requires contributions from a variety of areas including solid/fluid mechanics, physics, chemistry, and materials science, as tribological properties (friction, wear, etc.) are directly related to the energy transport, mechanical/electrical properties, and chemical reactions at the interfaces. In this section, we studied the electrical and thermal transport properties at nanoscale interfaces. The overall goal is to provide insights into the mechanisms underlying interfacial electrical and thermal conductivity at small scales.

5.1 Nanoscale Electric Contact Between an AFM Tip and Graphene Substrate

5.1.1 Introduction

Recently, single layer graphene (SLG) and multi layer graphene (MLG) have been the focus of extensive research as new electronic materials due to their unique properties, such as high electrical and thermal conductivity [54, 255–257], very low friction [42, 80, 104] and the quantum hall effect [256, 258, 259]. Many studies have focused on electrical properties due to the wide applicability of SLG and MLG to various electronic and electromechanical devices [260–264]. Contact resistance is one of the major factors limiting device scalability, reliability and performance in these devices [265, 266]. However, measurements of contact resistance have been inconsistent and its determining factors remain elusive [267]. Although there are quite a few studies on metal-SLG contact [267–272], a limited number of papers have focused on the electrical properties of metal-MLG contact [65, 67–70, 70, 71]. Several such studies have focused on the effect of number of graphene layers on contact resistance [67–69]. Other studies revealed a pressure dependency of electrical conductance on a double layer graphene surface [65] and that conductance is affected by step edges observed on the surface of MLG [65, 70, 70, 71]. These findings highlight at the critical role of the contact and its atomic-scale features in determining nanoscale resistance.

Here, we explore this important relationship between a nanoscale contact and its resistance by studying the electric contact between a platinum-coated AFM

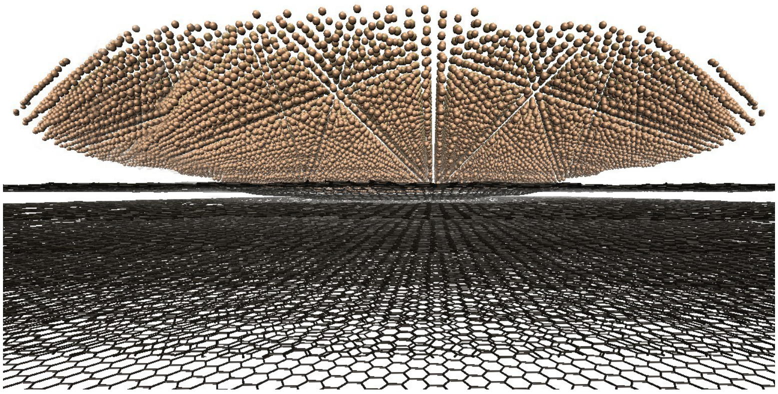

Figure 5.1: Snapshot from a molecular dynamics simulation of the apex of a 32 nm radius AFM tip placed on a seven layer graphite substrate.

tip and highly oriented pyrolytic graphite surface. Based on the measured contact resistance (performed by Dr. M.H. Lee's group) with different size AFM tips under various loads, we investigate the contact between tip and substrate using complementary simulations. The simulations are used to predict real and apparent contact area, and then this information is used with the resistance measured experimentally to calculate contact resistivity. The results are analyzed in terms of the ability of the two contact area definitions to capture the effects of load and tip size on resistance.

5.1.2 Methods

An atomistic model described the near-contact region of the experimental system. As shown in Figure 5.1, the model includes the apex of an AFM tip and an adjacent graphite substrate. Seven graphene sheets were ABA-stacked, with an interlayer distance of 0.335 nm. Here we used 7 layers of graphene to represent the top layers of the graphite thin film. The assumption is reasonable in the light of a recent report showing that the transition to a bulk-like resistivity appears at 7 - 8 layers of graphene [69]. The atoms in the bottommost layer of graphite were fixed to model a supporting substrate and the atoms at one end of all the layers were fixed as well to prevent relative sliding. The boundaries were periodic in the $x-y$ plane, and the boundary in the z-direction was formed by the fixed bottom layer of graphite and the rigid body of atoms at the top of the tip. The model tips had a hemispherical geometry and consist of platinum atoms in a FCC structure, with the same radii as the experimental tips (32 and 77 nm). A constant external normal load was maintained on the rigid body at the top of the tip. A Langevin thermostat was applied to the free atoms in the system to maintain a temperature of 300K. The inter-atomic interactions within the tip and substrate were described via the Embedded Atom Method (EAM) potential and the AIREBO potential [200] respectively, and the long range interactions between tip and substrate were modeled using the LJ potential (energy minimum 0.022 eV, zero-crossing distance 0.295 nm). The simulations were performed using the LAMMPS simulation software [105].

5.1.3 Results and Discussion

Figure 5.2 shows the resistance measured using AFM with 32 and 77 nm radius tips under loads between 100 and 800 nN. For the 77 nm radius tip in Figure 5.2 (b), there are three sets of data. All resistances measured with the 77 nm tip are smaller than those measured with the 32 nm tip. Further, for both tips, resistance decreases monotonically with increasing load.

The potential sources of the measured resistance are the Pt-coated tip, the graphite and the contact itself. The resistivity of Pt is very small ($\rho_{Pt} \sim 10^{-7}\ \Omega \cdot m$ [273]), so the tip can be neglected as a major factor. The resistance of the graphite film in this system can be estimated as $R_g = \frac{\rho_g}{kt}$, where k is a geometric constant and t is thickness [274]. For our experiments, t=0.2 mm and the geometric constant can be estimated to be on the order of 1. The maximum resistivity of graphite is in the out-of-plane direction and has been found to be up to $\rho_g \sim 10^{-3}\ \Omega \cdot m$ [275]. This means that the largest possible resistance contribution of the graphite is likely to be on the order of 10 Ω. This is orders of magnitude smaller than the measured resistivity reported in Figure 5.2 which suggests that the dominant resistance is due to the contact itself.

Contact resistance can be defined as $R_c = \rho_c/A$ where ρ_c is the contact resistivity with units of $\Omega \cdot m^2$ and A is the contact area [276]. This Ohms law-based relationship was derived for larger scale contacts. However, although alternatives to Ohms law have been developed for cases where continuum assumptions may break down [62, 63], we apply the simplest form of the contact resistance equation. This approximation is justified by recent work demonstrating ohmic scaling to the atomic limit [64].

The challenge in evaluating the contact resistance expression is that contact area is difficult to define at nanoscale. There are two possible definitions of contact area, real and apparent. On larger length scales, the apparent contact is the area between two solid surfaces defined by the boundaries of their macroscopic interface and "real contact" includes the effect of the roughness and can be considered as the sum of the contact areas of many micro scale asperities [277]. These concepts have been applied to small-scale contacts, such as those considered here, with the apparent area defined in terms of the boundaries of nanoscale interface and the real contact area the sum of atomic-scale asperities [94, 97, 278]. Further, for nanoscale contacts, it has been shown that geometry and loading conditions may affect real

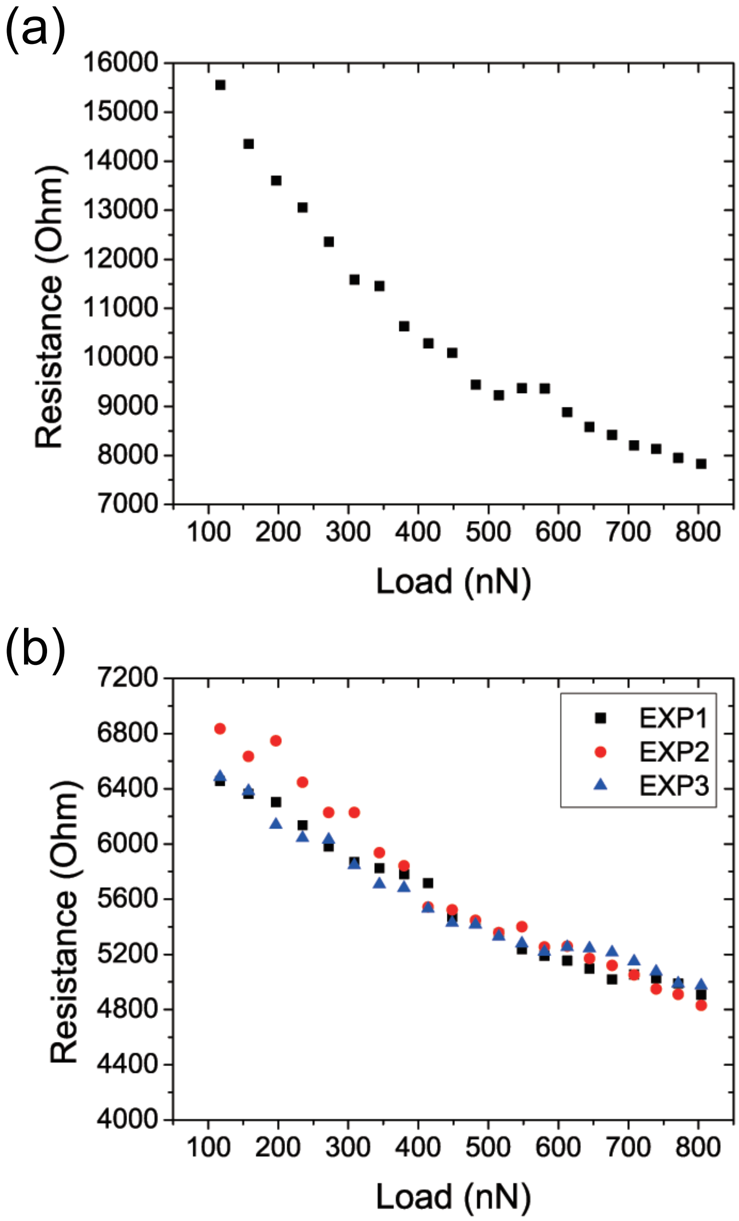

Figure 5.2: Contact resistance as a function of load measured by conducting AFM with (a) 32 nm and (b) 77 nm tips on graphite. Credit to Dr. M.H.Lee's group

and apparent contact area very differently [94, 97, 278]. The contrast between real and apparent contact area in our simulations is illustrated in Figure 5.3 where the color contour map shows the distribution of the tip-substrate atom distances and the black spheres represent tip atoms in contact with the substrate. Tip atoms in contact are defined as those within 0.3 nm of a substrate atom. The threshold value of 0.3 nm is used simply because it is the average of Pt interatomic distance (0.27nm) and graphite interlayer distance (0.33 nm). As expected, the real contact area appears to be only a subset of the apparent contact area.

Using the simulation data, we can determine the real and apparent areas of contact as functions of load for both model tips. We quantify real contact area, A_r, as the number of atoms in the contact multiplied by the average surface area per atom [97]. The apparent contact area, A_a, is calculated as the circle having a radius equal to half the distance between the contact atoms furthest from each other in the plane of the contact. Variation of contact size with load and tip radius calculated from MD simulation using these two definitions of contact area is shown in Figure 5.4 (a). We next use these results from simulation and the experimentally-measured resistance to calculate the contact resistivity where we assume $R \approx R_c$. Note that the contact resistance from experiment shown in Figure 5.2 was obtained at slightly different loads that the contact areas from simulation shown in Figure 5.4 (b). Therefore, power-law interpolation was used to estimate contact area from the simulation data at the experimentally-measured loads.

We observe that the contact resistivity calculated using apparent contact area increases with load, but is nearly constant when calculated using the real contact area. Ideally, the effect of load on resistance can be captured entirely by the contact area such that the contact resistivity is a constant. Therefore, the trends in Figure 5.4 (b) indicate that real contact area is a better measure of contact size that apparent contact for nanoscale electrical resistance studies.

We also observe that the contact resistivity in Figure 5.4 (b) calculated using real contact area is larger for the smaller tip. This suggests that there is other factor (in addition to area) that changes with tip size and affects contact resistance. A previous study on the resistivity of few-layer graphene showed the resistivity is linearly related to the distance between adjacent graphene layers [279]. We assume a similar relationship is applicable to contact resistance. Our simulations reveal that the average distance between the bottommost atoms of the tip and the topmost atoms of the substrate is $\sim 7\%$ smaller with the 77 nm radius tip as compared to the 32 nm radius tip due to greater deformation. This is very consistent with the observation that the contact resistivity calculated from the real contact area of the 77 nm radius tip is $\sim 9\%$ smaller than that calculated from the real contact area of the 32 nm tip. Therefore, tip size appears to affect resistance not only through contact area but also through near-contact deformation. Further study is needed to quantify the effect of deformation and determine if there are other factors involved.

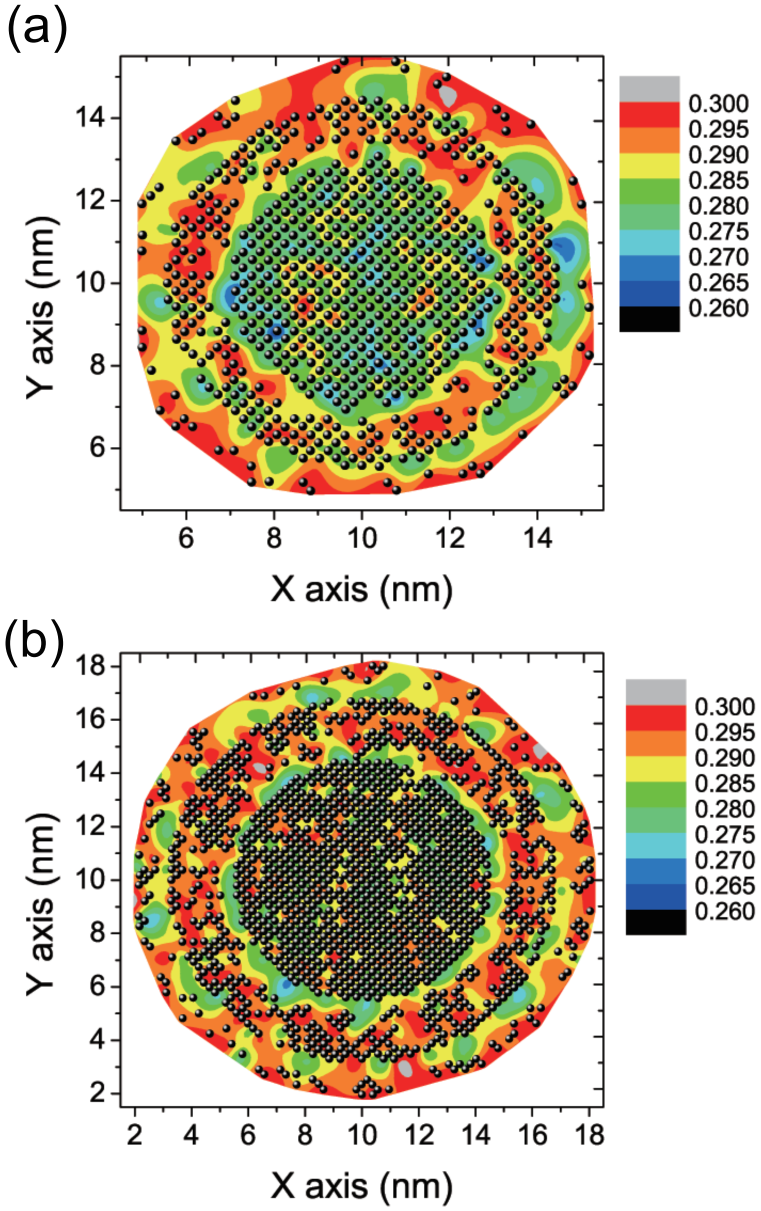

Figure 5.3: Illustration of the real (black spheres) and apparent (color contour) contact areas for the (a) 32 nm and (b) 77 nm tips from an MD simulation of contact with a 200 nN load. The colors in the contour plot reflect local distances between the tip and substrate; legend units are nm.

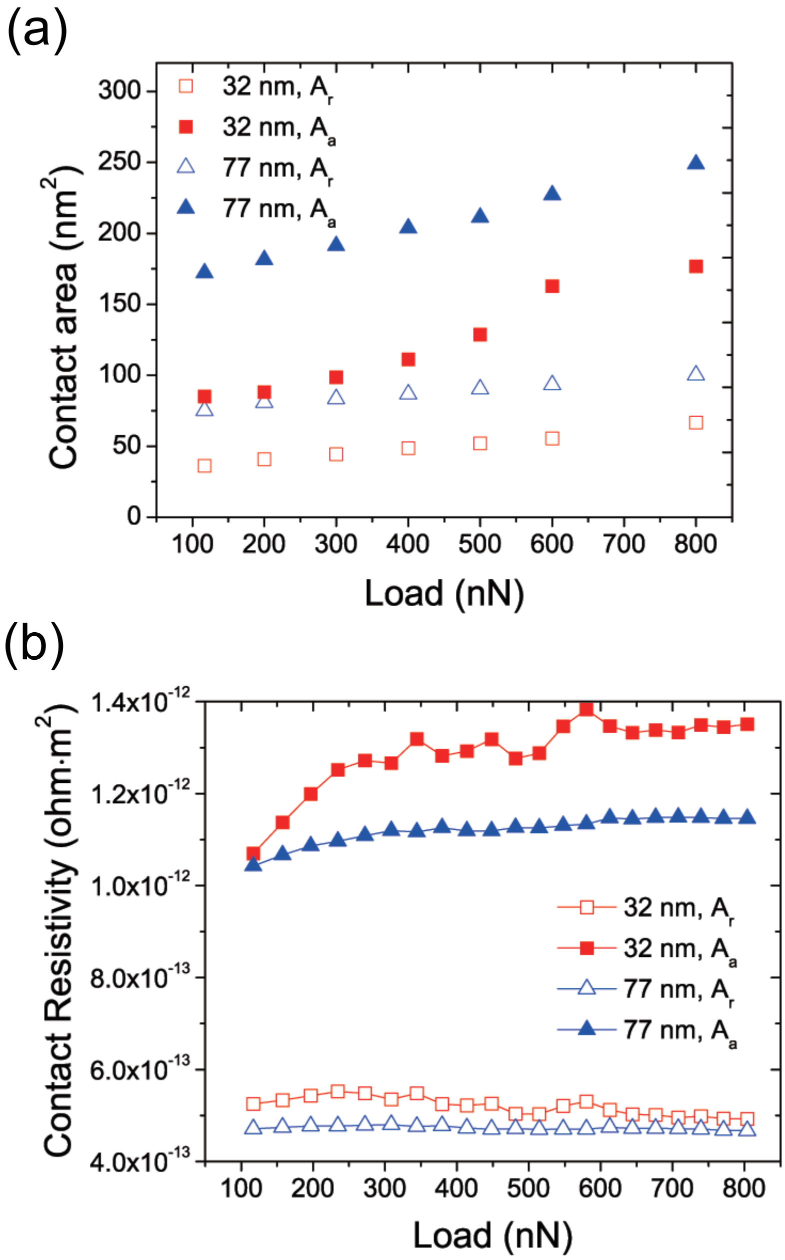

Figure 5.4: (a)Variation of real and apparent contact area with load and tip radius calculated from MD simulation. (b)Contact resistivity calculated from the experimentally measured resistance and the simulation-predicted real A_r (hollow symbols) and apparent A_a (solid symbols) contact areas for the 32 nm (squares) and 77 nm (triangles) radius tips.

5.1.4 Conclusion

To summarize, we study the nanoscale electric contact between an AFM tip and graphite surface. The resistance of different size tips (32 and 77 nm radii) under various loads (100 to 800 nN) is measured by AFM with voltage applied between tip and substrate. Analysis of the various potential contributions to the measured resistance indicates that the contact itself is the dominant factor. Contact resistance is related to contact resistivity and contact size. Atomistic simulations are used to quantify contact size in terms of real and apparent contact area. Contact resistivity is then calculated using measured resistance and both definitions of area from simulation. We observe that contact resistivity is independent of load only if the real contact area is used in the calculation which indicates real contact area is a better measure of contact size. The effect of tip size on contact resistance, however, cannot be fully captured by either definition of contact which indicates that contact resistivity is somewhat affected by tip size. Analysis suggests that one mechanism by which this might happen is through the interface distance. Overall, this study reveals that, although load and tip size affect the resistance of nanoscale electrical contacts, these effects can be predominantly captured by correctly defining contact size as the real contact area. Since real contact area can be readily calculated from simulations, this study encourages further collaboration between experiments and simulations for investigating nanoscale electrical contacts. Most significantly, this study emphasize the role of atom-scale contact features in determining contact resistance at the nanoscale.

5.2 Thermal Conductivity of Cellulose Crystal at Nanoscale Interface

5.2.1 Introduction

The increasing interest in flexible electronics has pushed development of new nanomaterials that provide seamless integrated structure-property interactions required for a variety of new, efficient configurations in electronic devices (e.g., organic solar cells, organic light emitting diodes, etc.). Of particular interest is the development of materials with high flexibility, impact strength and transparency with tailored stiffness, thermal expansion, and thermal conductivity to minimize stability problems at interfaces within the electronic architectures. While a broad number of materials are being investigated in this regard, cellulose derivatives [280–283] represent attractive candidates due to their abundant, renewable, and sustainable character [284]. Particularly, the unique set of properties exhibited by cellulose nanocrystals (CNCs) rod-like nanoparticles (5-20 nm wide, 50-500 nm long) [285] greatly expand the range of attainable properties and potential applications [286] due to their intrinsic high anisotropy (Figure 1a) and remarkable organization capabilities [285, 287]. In the presence of solvents CNCs can form chiral nematic mesophases, which can in turn be transferred to the solid state after evaporation. The resultant chiral nematic nanostructures [288, 289] can be distinguished by their in-plane property isotropy and iridescent structural coloration [290, 291].

Although the CNC chiral nematic organization can act at long range and so serve as a structural template for other material types assembly [292, 293],external forces (e.g., shear, electric, magnetic, etc.) can disrupt the organization in order to align the CNCs in specific directions and obtain different material responses. For instance, shear-alignment of aqueous CNC suspensions has been previously explored to reduce the coefficient of thermal expansion of nanostructured CNC films, while maintaining film transparency [290]; such tendency is highly beneficial in the design of organic electronic devices, especially light emitting diodes [281, 283]. Thermal conductivity is also a critical property, where CNC orientation can be very advantageous to improve heat management and offer a more efficient integral performance (i.e., device stability and durability [281]). Nonetheless, any structural modification performed to enhance optical and thermomechanical properties will be inherently connected to changes in the films heat transport properties. It is therefore desirable to understand the potential interplay between thermal conductivity and CNC organization, enabling further heat control in nanostructured materials [294, 295].

Here, we combine MD simulations with experimental measurements to achieve a multiscale description of the thermal conductivity from single cellulose crystals to their organized nanostructured films having different degrees of CNC orientation, while highlighting the fundamental role played by CNC-CNC interfaces in the in-plane heat transport towards an integral design of nanostructured materials[1].

---

[1] This section appeared in slightly different form as Jairo A Diaz, Zhijiang Ye,

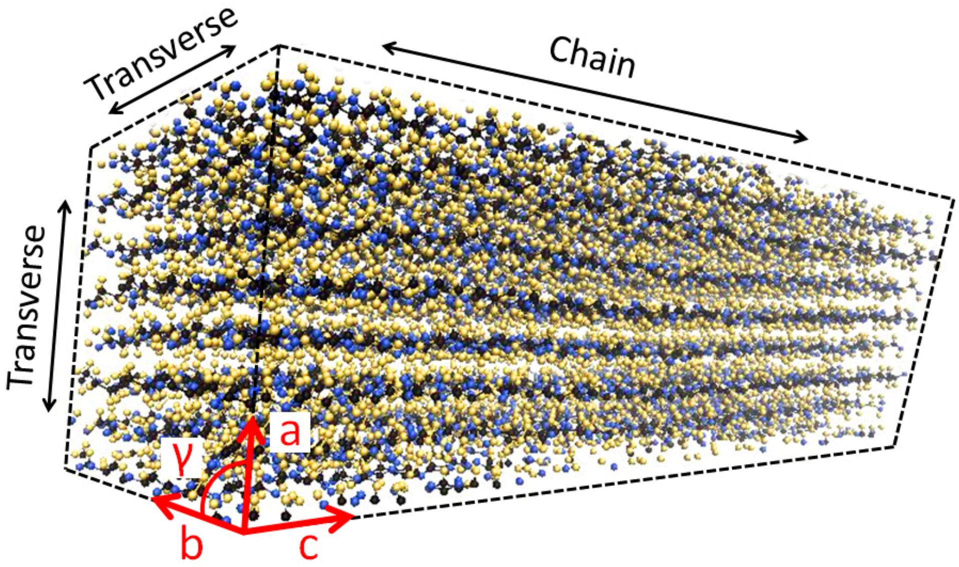

Figure 5.5: Atomistic illustration of a monoclinic single cellulose Iβ nanocrystal employed in MD simulations; spheres represent atoms with black carbon, blue oxygen, and yellow hydrogen.

Experiments in this study were performed by Dr. Jeffrey P. Youngblood's group.

5.2.2 Methods

Models of cellulose I crystals were constructed using Materials Studio software with unit cell parameters from X-ray diffraction [296] and simulations were performed using LAMMPS simulation software [105]. ReaxFF force field [297] was used to describe the atomic interactions. Note that a reactive force field is necessary to enable the model to capture the breaking (and potentially formation) of covalent bonds and it captures the hydrogen bonding. Two different systems were modeled: a single crystal ($3.65 \times 3.36 \times 10.80$ nm^3) (see Figure 5.5) and two adjacent crystals (each crystal $3.65 \times 3.36 \times 5.40$ nm^3) aligned in three different orientations (see Figure 5.6). Atoms at the two ends of the single cellulose I crystal or the two-crystal systems were treated as rigid bodies. First, the temperature of the model system

---

Xiawa Wu, Arden L Moore, Robert J Moon, Ashlie Martini, Dylan J Boday and Jeffrey P Youngblood, "Thermal conductivity in nanostructured films: from single cellulose nanocrystals to bulk films", Biomacromolecules 15, 4096-4101 (2016). It is reproduced here by permission of the other authors.

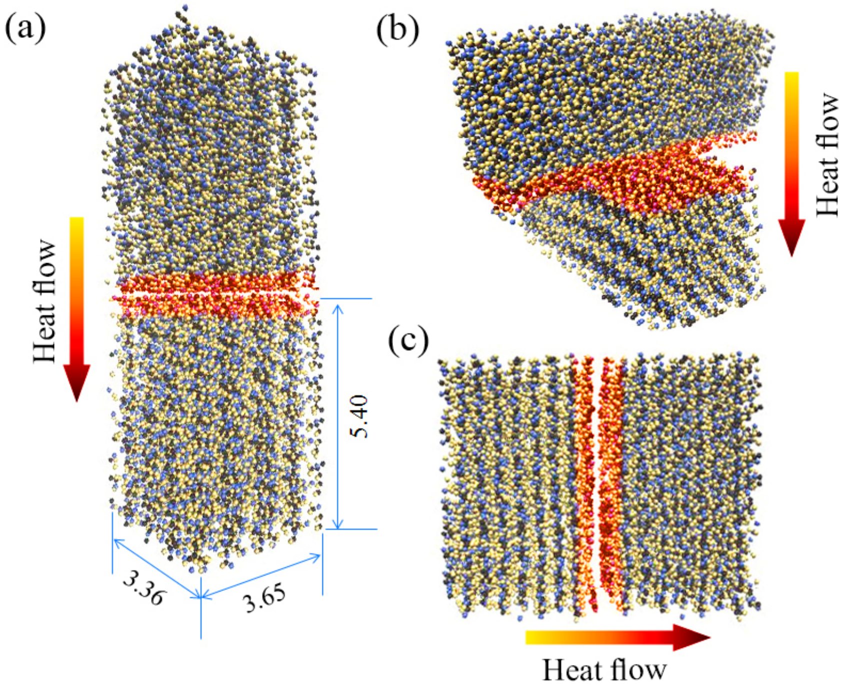

Figure 5.6: Configurations studied for interfacial thermal resistance: (a) chain, (b) transverse perpendicular, and (c) transverse parallel; The interface regions highlighted in red.

was set to 300 K and the structures were allowed to relax. Then, a constant heat flux was applied to the atoms adjacent to one of the rigid bodies and extracted the same heat flux at the other end. Simulations were run long enough to ensure the temperature distribution along the crystal or crystals was stable. Thermal conductivity of the system was calculated using Fouriers law based on the slope of the linear temperature distribution and the imposed heat flux. Four independent simulations were run for each case; values of thermal conductivity and associated error reported are the average and standard deviation from the four simulations.

5.2.3 Results and Discussion

In order to estimate the individual contributions of single crystals to the thermal conductivity of a bulk film, we calculated the thermal conductivity of a single cellulose I crystal using MD simulations (Figure 5.5). Although electrons are not included in the model, we assume predictions are reasonable since electronic contributions to thermal conductivity are small in electrically insulating materials.

[295,298] Thermal conductivities in the chain (c-axis) and transverse (a- and b-axes) directions were obtained from the slope of the linear temperature distribution and the imposed heat flux by using Fouriers law.

The thermal conductivity in the chain direction was predicted to be $\sim 5.7 \pm 0.9$ $\mathrm{Wm^{-1}K^{-1}}$ whereas the transverse directions exhibited lower values $\sim 0.72 \pm 0.12$ $\mathrm{Wm^{-1}K^{-1}}$. The ten-fold increase in the chain direction can be directly correlated to the intrinsic crystalline anisotropy, where weaker intermolecular interactions in the transverse directions [296] (i.e., hydrogen bonding in transverse directions as compared to covalent in the axial direction) can reduce phonon propagation. Materials with small unit cells, low thermal expansion and average sound velocity (high elastic modulus to density ratio) are expected to have high thermal conductivity at high temperatures (i.e., above Debye temperature) [299]. Except for their relatively large unit cells 0.658 nm3 [296], these properties are exhibited by the chain direction of a single cellulose I crystal [285, 290], therefore yielding a thermal conductivity that is almost five times larger than that previously reported for cellulose fiber/epoxy composites in the in-plane direction [281] ($\sim$1.1 $\mathrm{Wm^{-1}K^{-1}}$) and close to an order of magnitude larger than that exhibited by lingo-cellulosic specimens [300] (birch hardwood $\sim$0.25 $\mathrm{Wm^{-1}K^{-1}}$) and by other types of materials like amorphous polymers [238, 301] $\sim$0.2 $\mathrm{Wm^{-1}K^{-1}}$ as well as liquid crystal composites $\sim$0.7 $\mathrm{Wm^{-1}K^{-1}}$ [302] at room temperature.

We modeled the heat transport between two adjacent cellulose Iβ crystals in chain, parallel and perpendicular configurations (Figure 5.6) multiple interfacial configurations may be present during self-organization of two crystals (e.g. 21 configurations for 6 crystalline planes) following the same procedure implemented in the analysis of a single crystal, and assuming serial thermal resistance across the two cellulose Iβ crystals and the interface between them,

$$\frac{L_t}{k_t A} = \frac{L_{c1}}{k_{c1} A} + \frac{L_i}{k_i A} + \frac{L_{c2}}{k_{c2} A} \tag{5.1}$$

where, L_t is the total length of the two CNC model, L_{c1} and L_{c2} are the lengths of each cellulose crystal, and L_i is the length of the interface in the heat transfer direction (Figure 5.6). A similar naming scheme is used for thermal conductivity, k. The cross-sectional area, A, is perpendicular to the direction of heat transfer and is constant for a given configuration (Figure 5.5). k_i in the chain configuration was 0.043 $\mathrm{Wm^{-1}K^{-1}}$, calculated from Equation 1 by using: $L_{c1} = L_{c2} = 5.4$ nm as the lengths of the model crystals, L_i= 0.44 nm estimated for all configurations to be the average distance between two crystals [303] and thermal conductivities $k_{c1} = k_{c2} = 5.7$ $\mathrm{Wm^{-1}K^{-1}}$ and k_t= 0.77 $\mathrm{Wm^{-1}K^{-1}}$ calculated from slope of the linear temperature distribution and the imposed heat flux as described previously. Using the same approach, k_i for the parallel and perpendicular configurations were

Table 5.1: Summary of anisotropic thermal conductivity of aligned CNCs.

Material Type	Alignment	T[K]	Conductivity [W/(mK)]
Single crystal	Chain direction	300	5.7
Single crystal	Transverse direction	300	0.72
Crystal-crystal Interface	Chain config.	300	0.043
Crystal-crystal Interface	Transverse perp. config.	300	0.033
Crystal-crystal Interface	Transverse paral. config.	300	0.045

estimated around 0.045 and 0.033 $\mathrm{Wm^{-1}K^{-1}}$, respectively. All results are summarized in Table 5.1.

The interfacial thermal conductivity was approximately one order of magnitude smaller than the total thermal conductivity of two cellulose crystals in all three configurations, which supports the idea that heat transport in the bulk CNC films is limited by the interfaces between crystals. Interestingly, the range of interfacial thermal resistances (L_i/k_i) predicted for cellulose Iβ single crystals, 9.4 to 12.6 $\mathrm{GW^{-1}m^2K}$, is lower than that found in some low thermal conductivity thermoelectric alloys34 (e.g. $\sim$95 $\mathrm{GW^{-1}m^2K}$ for $\mathrm{Si_{0.7}Ge_{0.3}}$ at 300 K) and even than that of materials governed by weak van der Waals interactions [304] but exceptionally high thermal conductivity ($\sim$6.6 $\mathrm{Wm^{-1}K^{-1}}$) [305] like carbon nanotubes $\sim$83 $\mathrm{GW^{-1}m^2K}$. The lower thermal interface resistance between cellulose crystals can be mainly attributed to their strong surface hydrogen bonds, as thermal conductivity across interfaces scales with interfacial bonding strength [306–308], which suggests possible further steps in enhancing heat transport in CNC bulk films by controlling crystal-crystal interfaces and self-organization.

5.2.4 Conclusion

We described via MD simulations how the intrinsic anisotropy of single cellulose crystals produced a thermal conductivity in the chain direction that is ten times greater than that estimated in the transverse directions (Table 5.1, Figure 5.6). MD simulations confirmed a drastic decrease in thermal conductivity due to the interface between two cellulose crystals in several different configurations. Nonetheless, such inherent thermal transport barrier found for CNCs was almost an order of magnitude lower than that exhibited by carbon nanotubes, and equal those present in low thermal conductivity thermoelectric alloys. We also demonstrated how MD simulations and CNC orientation can closely describe and potentially control the conductive heat transport from nanostructured isotropic-chollesteric to anisotropic shear-oriented cellulose films, while keeping an intricate connection with the broad range of possible optical responses needed for further material usage in current and future cost-effective, technological applications.

Chapter 6

FUTURE WORK AND SUMMARY

Even though we have done significant amount of work on tribological, electrical and thermal properties of 2D materials, we believe there are still some interesting and important future research topics which will be described in following sections.

6.1 Future Work

6.1.1 Effect of Step Edges on Tip-Substrate Contact Under Electrical Field

Graphene, $\alpha - BN$ and MoS_2 are promising materials for nanoelectronic application due to their good electrical properties. However, studies have shown that the electrical properties of these materials can be affected by many factors. It was reported that electrical resistivity of graphene increased with number of layers [67–69]. The effect of doping on electrical conductivity of $\alpha - BN$ was also reported [66]. Another study revealed a pressure and temperature dependence of electrical conductance on a double layer graphene surface [65]. The electrical contact between an AFM and a perfectly flat surface has been well studied [267–272]. However, in practice, we have to deal with imperfections on surfaces (e.g. step edges). As shown in Chapter 3, step edges exhibit very unique behavior.

Previous study described that the electrical conductance of graphene was affected by step edges observed on the surface of multilayer graphene [65, 70, 70, 71]. However, the mechanisms of the step edge effect were not fully understood. Currently, no studies have been reported on the effect of step edges on $\alpha - BN$ and MoS_2 electrical conductance. Understanding the mechanisms underlying electrical properties is important to improving the performance of nanoelectronic devices and saving energy costs. Follow up research on the effect of step edges on tip-substrate contact under an electrical field can be performed. The electrical field applied between tip and substrate may be varied. The response of the materials to the electrical field (e.g. surface conformation) may be characterized and correlated to the electrical resistance. This study can help understand the mechanisms underlying electrical conductance at step edge regions.

6.1.2 Size and Layer Dependence of Thermal Conductivity on Graphene

In Chapter 5, Section 5.2, we investigated the thermal conductivity of cellulose nanocrystals. The thermal conductivity of layered materials is also an interesting and important problem which determines the performance of thermal management devices. Thus, understanding the mechanisms underlying thermal conduction is significant. Currently, there are many studies on the thermal properties of graphene at the atomic scale, but limited studies on that topic for $\alpha - BN$ and MoS_2. For graphene, studies revealed that thermal conductivity increased with the number of layers [47, 54], while others observed the opposite trend [49, 55, 56]. In addition, it was reported that there was no size dependence of graphene thermal conductivity based on the sample sizes from 2.9 to 9.7 um diameter [51], while other studies showed two different trends: conductivity decreased [51, 57] or increased [53, 58] with graphene size. For MoS_2, studies showed the thermal conductivity of MoS_2 was independent of number of layers [59,60]. However, overall, the size and layer dependence of graphene/$\alpha - BN/MoS_2$ thermal conductivity is not fully understood.

Follow up research can be performed to study the size and layer dependence of graphene, $\alpha - BN$ and MoS_2 thermal conductivity using MD simulation. The thermal conductivity and thermal conductance may be characterized for different size and number of layers of materials by applying a heat flux through the materials. This study can provide guidelines for small scale thermal device applications.

6.1.3 Temperature Dependence of Atomic Friction with Closely Matched Experiments and Simulations

As discussed in Chapter 4, Section 4.3, studying and understanding the mechanisms underlying temperature dependence of atomic friction is important for enhanced performance of many engineering systems as well as advanced understanding of how friction occurs in general. Generally speaking, three effects can be identified as being most critical in determining the magnitude of interfacial friction and its temperature dependence: thermal excitation (thermolubricity) [252–254], adsorbates (whose presence is controlled by temperature via adsorption/desorption) [309, 310], and water (a special case of an adsorbate, which leads to thermally-induced formation and evaporation of water meniscus) [215, 311]. However, it is still not clear which mechanism is dominant for a given materials under certain conditions.

Follow up research can be performed to study the temperature dependence of friction using closely matched experiments and simulations, including matching tip materials and geometries, substrate materials, sliding directions, applied load and environments. Specifically, friction at wide range of temperatures may be characterized in both experiments and simulations. Comparison between experiments and simulations can provide insights into the atomistic mechanisms that govern the temperature dependence of interfacial friction for nanoscale single asperity contacts. Ultimately, this study can provide the knowledge base needed for rational design of applications such as MEMS devices and tip-based nanomanufacturing processes.

6.2 Concluding Remarks

To summarize, we utilize atomistic simulations and experimental measurements to study and understand the fundamental mechanisms underlying tribological, thermal and electrical phenomena at the nanoscale interfaces of graphene, BN, MoS_2, gold and AlNiCo quasicrystals. First, we presented novel results on the trioblogical behavior on defect-free substrates. Specifical topics that we explored include the evolution of materials at the contact between an atomic force microscope probe apex and adjacent graphene substrate, the dynamic response of 2D materials to out of plane mechanical loading and lateral offset, and the effects of geometric features and surface chemistry on the resistance of a nanoscale contact to sliding. Second, we studied the trioblogical behavior on substrates with defects and explored the influence of tip and substrate geometrical features on the sliding resistance at nanoscale interfaces. Then, we systematically investigated the tribological performance of solid lubricants under extreme conditions (environment, speed and temperature) by characterizing friction across a wide range of sliding speeds and temperatures under ambient and vacuum conditions. Finally, we discussed the electrical and thermal transport properties at nanoscale interfaces and their connections to nanoscale contact features. In general, our study provides new, fundamental understanding of interfacial friction on well defined surface features and under a variety of environmental conditions, and provides insights into the mechanisms underlying interfacial electrical and thermal conductivity at small scales. These are exciting research areas with significant potential to further scientific understanding and enable technological advancements.

BIBLIOGRAPHY

[1] D. O'Hare, Inorganic materials, Inorganic Materials, Wiley, Chichester 24 (8) (1996) 174.

[2] J. N. Coleman, M. Lotya, A. ONeill, S. D. Bergin, P. J. King, U. Khan, K. Young, A. Gaucher, S. De, R. J. Smith, et al., Two-dimensional nanosheets produced by liquid exfoliation of layered materials, Science 331 (6017) (2011) 568–571.

[3] Z. Deng, N. N. Klimov, S. D. Solares, T. Li, H. Xu, R. J. Cannara, Nanoscale interfacial friction and adhesion on supported versus suspended monolayer and multilayer graphene, Langmuir 29 (1) (2012) 235–243.

[4] J. Yang, Z. Liu, F. Grey, Z. Xu, X. Li, Y. Liu, M. Urbakh, Y. Cheng, Q. Zheng, Observation of high-speed microscale superlubricity in graphite, Physical Review Letters 110 (25) (2013) 255504.

[5] W. Qi, M. Wang, Size and shape dependent melting temperature of metallic nanoparticles, Materials Chemistry and Physics 88 (2) (2004) 280–284.

[6] R. Narayanan, M. A. El-Sayed, Shape-dependent catalytic activity of platinum nanoparticles in colloidal solution, Nano Letters 4 (7) (2004) 1343–1348.

[7] Z. Ye, D. Lee, S. A. Campbell, T. Cui, Thermally enhanced single-walled carbon nanotube microfluidic alignment, Microelectronic Engineering 88 (9) (2011) 2919–2923.

[8] A. Yaya, B. Agyei-Tuffour, D. Dodoo-Arhin, E. Nyankson, E. Annan, D. Konadu, E. Sinayobye, E. Baryeh, C. Ewels, Layered nanomaterials-a review, Global Journal of Engineering Design and Technology 2 (2012) 32–41.

[9] S. Mouras, A. Hamm, D. Djurado, J.-C. Cousseins, Synthesis of first stage graphite intercalation compounds with fluorides, Revue de chimie minérale 24 (5) (1987) 572–582.

[10] K. S. Novoselov, A. K. Geim, S. Morozov, D. Jiang, Y. Zhang, S. Dubonos, I. Grigorieva, A. Firsov, Electric field effect in atomically thin carbon films, Science 306 (5696) (2004) 666–669.

[11] C. Lee, X. Wei, J. W. Kysar, J. Hone, Measurement of the elastic properties and intrinsic strength of monolayer graphene, Science 321 (5887) (2008) 385–388.

[12] A. K. Geim, K. S. Novoselov, The rise of graphene, Nature Materials 6 (3) (2007) 183–191.

[13] A. Lipp, K. A. Schwetz, K. Hunold, Hexagonal boron nitride: fabrication, properties and applications, Journal of the European Ceramic Society 5 (1) (1989) 3–9.

[14] M. Engler, C. Lesniak, R. Damasch, B. Ruisinger, J. Eichler, Hexagonal boron nitride (hbn): Applications from metallurgy to cosmetics, in: CFI. Ceramic forum international, Vol. 84, Göller, 2007.

[15] M. Sun, J. Adjaye, A. E. Nelson, Theoretical investigations of the structures and properties of molybdenum-based sulfide catalysts, Applied Catalysis A: General 263 (2) (2004) 131–143.

[16] C. Feng, J. Ma, H. Li, R. Zeng, Z. Guo, H. Liu, Synthesis of molybdenum disulfide for lithium ion battery applications, Materials Research Bulletin 44 (9) (2009) 1811–1815.

[17] J. Chen, N. Kuriyama, H. Yuan, H. T. Takeshita, T. Sakai, Electrochemical hydrogen storage in mos2 nanotubes, Journal of the American Chemical Society 123 (47) (2001) 11813–11814.

[18] P. D. Fleischauer, R. Bauer, Chemical and structural effects on the lubrication properties of sputtered mos2 films, Tribology Transactions 31 (2) (1988) 239–250.

[19] D. Dowson, D. Dowson, History of tribology, Longman London, 1979.

[20] H. P. Jost, et al., Lubrication (tribology) education and research, A Report on the Present Position and Industry Needs, Department of Education and Science, HM Stationary Office, London.

[21] O. Pinkus, D. F. Wilcock, Strategy for energy conservation through tribology, Tech. rep., American Society of Mechanical Engineers, New York (1977).

[22] K. Holmberg, P. Andersson, A. Erdemir, Global energy consumption due to friction in passenger cars, Tribology International 47 (2012) 221–234.

[23] Y. Dong, Q. Li, A. Martini, Molecular dynamics simulation of atomic friction: A review and guide, Journal of Vacuum Science & Technology A 31 (3) (2013) 030801.

[24] C. M. Mate, G. M. McClelland, R. Erlandsson, S. Chiang, Atomic-scale friction of a tungsten tip on a graphite surface, in: Scanning Tunneling Microscopy, Springer, 1993, pp. 226–229.

[25] E. Meyer, R. Luthi, L. Howald, M. Bammerlin, M. Guggisberg, H. J. Guntherodt, Site-specific friction force spectroscopy, Journal of Vacuum Science and Technology B 14 (1996) 1285.

[26] P. Steiner, E. Gnecco, F. Krok, J. Budzioch, L. Walczak, J. Konior, M. Szymonski, E. Meyer, Atomic-sacle friction on stepped surface of ionic crystals, Physical Review Letters 106 (2011) 186104.

[27] T. Müller, M. Lohrmann, T. Kässer, O. Marti, J. Mlynek, G. Krausch, Frictional force between a sharp asperity and a surface step, Physical Review Letters 79 (25) (1997) 5066.

[28] H. Hölscher, D. Ebeling, U. D. Schwarz, Friction at atomic-scale surface steps: experiment and theory, Physical Review Letters 101 (24) (2008) 246105.

[29] D. P. Hunley, T. J. Flynn, T. Dodson, A. Sundararajan, M. J. Boland, D. R. Strachan, Friction, adhesion, and elasticity of graphene edges, Physical Review B 87 (3) (2013) 035417.

[30] Z. Ye, A. Otero-de-la Roza, E. R. Johnson, A. Martini, Effect of tip shape on atomic-friction at graphite step edges, Applied Physics Letters 103 (8) (2013) 081601.

[31] P. Egberts, Z. Ye, X. Z. Liu, Y. Dong, A. Martini, R. W. Carpick, Environmental dependence of atomic-scale friction at graphite surface steps, Physical Review B 88 (3) (2013) 035409.

[32] J. S. Choi, J.-S. Kim, I.-S. Byun, D. H. Lee, M. J. Lee, B. H. Park, C. Lee, D. Yoon, H. Cheong, K. H. Lee, Y.-W. Son, J. Y. Park, M. Salmeron, Friction anisotropy–driven domain imaging on exfoliated monolayer graphene, Science 333 (6042) (2011) 607–610.

[33] Y. Mishin, A. Suzuki, B. Uberuaga, A. Voter, Stick-slip behavior of grain boundaries studied by accelerated molecular dynamics, Physical Review B 75 (22) (2007) 224101.

[34] B. Bhushan, J. N. Israelachvili, U. Landman, Nanotribology: friction, wear and lubrication at the atomic scale, Nature 374 (6523) (1995) 607–616.

[35] J. A. Harrison, R. J. Colton, C. T. White, D. W. Brenner, Effect of atomic-scale surface roughness on friction: a molecular dynamics study of diamond surfaces, Wear 168 (1) (1993) 127–133.

[36] B. Persson, O. Albohr, U. Tartaglino, A. Volokitin, E. Tosatti, On the nature of surface roughness with application to contact mechanics, sealing, rubber friction and adhesion, Journal of Physics: Condensed Matter 17 (1) (2005) R1.

[37] Q. Li, Y. Dong, D. Perez, A. Martini, R. W. Carpick, Speed dependence of atomic stick-slip friction in optimally matched experiments and molecular dynamics simulations, Physical Review Letters 106 (12) (2011) 126101.

[38] I. Barel, M. Urbakh, L. Jansen, A. Schirmeisen, Unexpected temperature and velocity dependencies of atomic-scale stick-slip friction, Physical Review B 84 (11) (2011) 115417.

[39] E. Gnecco, R. Bennewitz, T. Gyalog, C. Loppacher, M. Bammerlin, E. Meyer, H.-J. Güntherodt, Velocity dependence of atomic friction, Physical Review Letters 84 (6) (2000) 1172.

[40] F. J. Clauss, Solid lubricants and self-lubricating solids, Academic Press, 1972.

[41] J. Monro, Pioneers of Electricity, Religious Tract Soc., 1890.

[42] A. Erdemir, Design criteria for superlubricity in carbon films and related microstructures, Tribology International 37 (7) (2004) 577–583.

[43] K. Ekinci, Electromechanical transducers at the nanoscale: actuation and sensing of motion in nanoelectromechanical systems (nems), Small 1 (8-9) (2005) 786–797.

[44] M.-W. Jang, C.-L. Chen, W. E. Partlo, S. R. Patil, D. Lee, Z. Ye, D. Lilja, T. A. Taton, T. Cui, S. A. Campbell, A pure single-walled carbon nanotube thin film based three-terminal microelectromechanical switch, Applied Physical Letters 98 (7) (2011) 073502–073502.

[45] B. Radisavljevic, A. Radenovic, J. Brivio, V. Giacometti, A. Kis, Single-layer mos2 transistors, Nature Nanotechnology 6 (3) (2011) 147–150.

[46] J. H. Seol, I. Jo, A. L. Moore, L. Lindsay, Z. H. Aitken, M. T. Pettes, X. Li, Z. Yao, R. Huang, D. Broido, et al., Two-dimensional phonon transport in supported graphene, Science 328 (5975) (2010) 213–216.

[47] W. Jang, Z. Chen, W. Bao, C. N. Lau, C. Dames, Thickness-dependent thermal conductivity of encased graphene and ultrathin graphite, Nano Letters 10 (10) (2010) 3909–3913.

[48] J. Hu, X. Ruan, Y. P. Chen, Thermal conductivity and thermal rectification in graphene nanoribbons: a molecular dynamics study, Nano Letters 9 (7) (2009) 2730–2735.

[49] W.-R. Zhong, M.-P. Zhang, B.-Q. Ai, D.-Q. Zheng, Chirality and thickness-dependent thermal conductivity of few-layer graphene: A molecular dynamics study, Applied Physics Letters 98 (11) (2011) 113107–113107.

[50] W. Cai, A. L. Moore, Y. Zhu, X. Li, S. Chen, L. Shi, R. S. Ruoff, Thermal transport in suspended and supported monolayer graphene grown by chemical vapor deposition, Nano Letters 10 (5) (2010) 1645–1651.

[51] S. Chen, A. L. Moore, W. Cai, J. W. Suk, J. An, C. Mishra, C. Amos, C. W. Magnuson, J. Kang, L. Shi, et al., Raman measurements of thermal transport in suspended monolayer graphene of variable sizes in vacuum and gaseous environments, ACS Nano 5 (1) (2010) 321–328.

[52] B. Kong, S. Paul, M. B. Nardelli, K. Kim, First-principles analysis of lattice thermal conductivity in monolayer and bilayer graphene, Physical Review B 80 (3) (2009) 033406.

[53] J. Haskins, A. Kinaci, C. Sevik, H. Sevincli, G. Cuniberti, T. Cagin, Control of thermal and electronic transport in defect-engineered graphene nanoribbons, ACS Nano 5 (5) (2011) 3779–3787.

[54] A. A. Balandin, S. Ghosh, W. Bao, I. Calizo, D. Teweldebrhan, F. Miao, C. N. Lau, Superior thermal conductivity of single-layer graphene, Nano Letters 8 (3) (2008) 902–907.

[55] S. Ghosh, I. Calizo, D. Teweldebrhan, E. Pokatilov, D. Nika, A. Balandin, W. Bao, F. Miao, C. N. Lau, Extremely high thermal conductivity of graphene: Prospects for thermal management applications in nanoelectronic circuits, Applied Physics Letters 92 (2008) 151911.

[56] S. Ghosh, W. Bao, D. L. Nika, S. Subrina, E. P. Pokatilov, C. N. Lau, A. A. Balandin, Dimensional crossover of thermal transport in few-layer graphene, Nature Materials 9 (7) (2010) 555–558.

[57] C. Faugeras, B. Faugeras, M. Orlita, M. Potemski, R. R. Nair, A. Geim, Thermal conductivity of graphene in corbino membrane geometry, ACS Nano 4 (4) (2010) 1889–1892.

[58] W. J. Evans, L. Hu, P. Keblinski, Thermal conductivity of graphene ribbons from equilibrium molecular dynamics: Effect of ribbon width, edge roughness, and hydrogen termination, Applied Physics Letters 96 (20) (2010) 203112–203112.

[59] C. Zhi, Y. Bando, C. Tang, H. Kuwahara, D. Golberg, Large-scale fabrication of boron nitride nanosheets and their utilization in polymeric composites with improved thermal and mechanical properties, Advanced Materials 21 (28) (2009) 2889–2893.

[60] C. Muratore, V. Varshney, J. Gengler, J. Hu, J. Bultman, T. Smith, P. Shamberger, B. Qiu, X. Ruan, A. Roy, et al., Cross-plane thermal properties of transition metal dichalcogenides, Applied Physics Letters 102 (8) (2013) 081604–081604.

[61] L. Duclaux, B. Nysten, J. Issi, A. Moore, Structure and low-temperature thermal conductivity of pyrolytic boron nitride, Physical Review B 46 (6) (1992) 3362.

[62] D.-Z. Guo, S.-M. Hou, G.-M. Zhang, Z.-Q. Xue, Conductance fluctuation and degeneracy in nanocontact between a conductive afm tip and a granular surface under small-load conditions, Applied Surface Science 252 (14) (2006) 5149–5157.

[63] G. Wexler, The size effect and the non-local boltzmann transport equation in orifice and disk geometry, Proceedings of the Physical Society 89 (4) (1966) 927.

[64] B. Weber, S. Mahapatra, H. Ryu, S. Lee, A. Fuhrer, T. Reusch, D. Thompson, W. Lee, G. Klimeck, L. C. Hollenberg, et al., Ohms law survives to the atomic scale, Science 335 (6064) (2012) 64–67.

[65] M. Nagase, H. Hibino, H. Kageshima, H. Yamaguchi, Local conductance measurements of double-layer graphene on sic substrate, Nanotechnology 20 (44) (2009) 445704.

[66] Y. Xue, Q. Liu, G. He, K. Xu, L. Jiang, X. Hu, J. Hu, Excellent electrical conductivity of the exfoliated and fluorinated hexagonal boron nitride nanosheets, Nanoscale Research Letters 8 (1) (2013) 1–7.

[67] A. Venugopal, A. Pirkle, R. M. Wallace, L. Colombo, E. M. Vogel, Contact resistance studies of metal on hopg and graphene stacks, in: AIP Conference Proceedings, Vol. 1173, 2009, p. 324.

[68] A. Venugopal, L. Colombo, E. Vogel, Contact resistance in few and multilayer graphene devices, Applied Physics Letters 96 (1) (2010) 013512–013512.

[69] P. N. Nirmalraj, T. Lutz, S. Kumar, G. S. Duesberg, J. J. Boland, Nanoscale mapping of electrical resistivity and connectivity in graphene strips and networks, Nano Letters 11 (1) (2010) 16–22.

[70] M. Ahmad, S. A. Han, D. H. Tien, J. Jung, Y. Seo, Local conductance measurement of graphene layer using conductive atomic force microscopy, Journal of Applied Physics 110 (2011) 054307.

[71] S. Banerjee, M. Sardar, N. Gayathri, A. Tyagi, B. Raj, Conductivity landscape of highly oriented pyrolytic graphite surfaces containing ribbons and edges, Physical Review B 72 (7) (2005) 075418.

[72] B. J. Alder, T. Wainwright, Studies in molecular dynamics. i. general method, The Journal of Chemical Physics 31 (1959) 459.

[73] S. G. Volz, G. Chen, Molecular dynamics simulation of thermal conductivity of silicon nanowires, Applied Physics Letters 75 (14) (1999) 2056–2058.

[74] S. G. Volz, G. Chen, Molecular-dynamics simulation of thermal conductivity of silicon crystals, Physical Review B 61 (4) (2000) 2651.

[75] X. Ma, P. Shrotriya, Molecular dynamics simulation of electrical field induced conformational transition and associated frictional performance of monomolecular films, Journal of Physics D: Applied Physics 45 (37) (2012) 375306.

[76] Z. Hu, J. Vatamanu, O. Borodin, D. Bedrov, A molecular dynamics simulation study of the electric double layer and capacitance of [bmim][pf 6] and [bmim][bf 4] room temperature ionic liquids near charged surfaces, Physical Chemistry Chemical Physics 15 (34) (2013) 14234–14247.

[77] T. Filleter, J. McChesney, A. Bostwick, E. Rotenberg, K. Emtsev, T. Seyller, K. Horn, R. Bennewitz, Friction and dissipation in epitaxial graphene films, Physical Review Letters 102 (8) (2009) 086102.

[78] T. Filleter, R. Bennewitz, Structural and frictional properties of graphene films on sic (0001) studied by atomic force microscopy, Physical Review B 81 (15) (2010) 155412.

[79] C. Lee, X. Wei, Q. Li, R. Carpick, J. W. Kysar, J. Hone, Elastic and frictional properties of graphene, Physica Status Solidi (b) 246 (11-12) (2009) 2562–2567.

[80] C. Lee, Q. Li, W. Kalb, X.-Z. Liu, H. Berger, R. W. Carpick, J. Hone, Frictional characteristics of atomically thin sheets, Science 328 (5974) (2010) 76–80.

[81] A. Smolyanitsky, J. Killgore, V. Tewary, Effect of elastic deformation on frictional properties of few-layer graphene, Physical Review B 85 (3) (2012) 035412.

[82] P. Liu, Y. Zhang, A theoretical analysis of frictional and defect characteristics of graphene probed by a capped single-walled carbon nanotube, Carbon 49 (11) (2011) 3687–3697.

[83] L. Xu, T.-B. Ma, Y.-Z. Hu, H. Wang, Vanishing stick–slip friction in few-layer graphenes: the thickness effect, Nanotechnology 22 (28) (2011) 285708.

[84] S. J. Stuart, A. B. Tutein, J. A. Harrison, A reactive potential for hydrocarbons with intermolecular interactions, The Journal of Chemical Physics 112 (2000) 6472.

[85] A. Fasolino, J. Los, M. I. Katsnelson, Intrinsic ripples in graphene, Nature Materials 6 (11) (2007) 858–861.

[86] C. Tang, L. Meng, L. Sun, K. Zhang, J. Zhong, Molecular dynamics study of ripples in graphene nanoribbons on 6h-sic (0001): Temperature and size effects, Journal of Applied Physics 104 (2008) 113536.

[87] T. Nakajima, K. Shintani, Molecular dynamics study of energetics of graphene flakes, Journal of Applied Physics 106 (11) (2009) 114305–114305.

[88] J. Whitehead, Surface deformation and friction of metals at light loads, Proceedings of the Royal Society of London. Series A (1950) 109–124.

[89] N. N. Gosvami, T. Filleter, P. Egberts, R. Bennewitz, Microscopic friction studies on metal surfaces, Tribology Letters 39 (1) (2010) 19–24.

[90] R. W. Carpick, D. Ogletree, M. Salmeron, Lateral stiffness: a new nanomechanical measurement for the determination of shear strengths with friction force microscopy, Applied Physics Letters 70 (12) (1997) 1548–1550.

[91] F. Bonelli, N. Manini, E. Cadelano, L. Colombo, Atomistic simulations of the sliding friction of graphene flakes, The European Physical Journal B 70 (4) (2009) 449–459.

[92] Y.-S. Pan, D.-S. Xiong, R.-Y. Ma, A study on the friction properties of poly (vinyl alcohol) hydrogel as articular cartilage against titanium alloy, Wear 262 (7) (2007) 1021–1025.

[93] B. V. Derjaguin, V. M. Muller, Y. P. Toporov, Effect of contact deformations on the adhesion of particles, Journal of Colloid and Interface Science 53 (2) (1975) 314–326.

[94] B. Luan, M. O. Robbins, The breakdown of continuum models for mechanical contacts, Nature 435 (7044) (2005) 929–932.

[95] U. D. Schwarz, O. Zwörner, P. Köster, R. Wiesendanger, Quantitative analysis of the frictional properties of solid materials at low loads. i. carbon compounds, Physical Review B 56 (11) (1997) 6987.

[96] R. W. Carpick, D. F. Ogletree, M. Salmeron, A general equation for fitting contact area and friction vs load measurements, Journal of Colloid and Interface Science 211 (2) (1999) 395–400.

[97] Y. Mo, K. T. Turner, I. Szlufarska, Friction laws at the nanoscale, Nature 457 (7233) (2009) 1116–1119.

[98] J. Gao, W. Luedtke, D. Gourdon, M. Ruths, J. Israelachvili, U. Landman, Frictional forces and amontons' law: from the molecular to the macroscopic scale, The Journal of Physical Chemistry B 108 (11) (2004) 3410–3425.

[99] O. Pietrement, M. Troyon, Study of the interfacial shear strength pressure dependence by modulated lateral force microscopy, Langmuir 17 (21) (2001) 6540–6546.

[100] L. Wenning, M. Müser, Friction laws for elastic nanoscale contacts, Europhysics Letters 54 (5) (2001) 693.

[101] Z. Deng, A. Smolyanitsky, Q. Li, X.-Q. Feng, R. J. Cannara, Adhesion-dependent negative friction coefficient on chemically modified graphite at the nanoscale, Nature Materials 11 (12) (2012) 1032–1037.

[102] A. Smolyanitsky, J. Killgore, Anomalous friction in suspended graphene, Physical Review B 86 (12) (2012) 125432.

[103] A. Smolyanitsky, S. Zhu, Z. Deng, T. Li, R. J. Cannara, Effects of surface compliance and relaxation on the frictional properties of lamellar materials, RSC Advances 4 (2014) 26721–26728.

[104] Z. Ye, C. Tang, Y. Dong, A. Martini, Role of wrinkle height in friction variation with number of graphene layers, Journal of Applied Physics 112 (11) (2012) 116102.

[105] S. Plimpton, Fast parallel algorithms for short-range molecular dynamics, Journal of Computational Physics 117 (1) (1995) 1–19.

[106] S. Kwon, S. Choi, H. Chung, H. Yang, S. Seo, S.-H. Jhi, J. Y. Park, Probing nanoscale conductance of monolayer graphene under pressure, Applied Physics Letters 99 (1) (2011) 013110.

[107] Z. Ye, H. Moon, M. H. Lee, A. Martini, Size and load dependence of nanoscale electric contact resistance, Tribology International 71 (2014) 109–113.

[108] Z. Liu, J. Yang, F. Grey, J. Z. Liu, Y. Liu, Y. Wang, Y. Yang, Y. Cheng, Q. Zheng, Observation of microscale superlubricity in graphite, Physical Review Letters 108 (20) (2012) 205503.

[109] Q. Zheng, B. Jiang, S. Liu, Y. Weng, L. Lu, Q. Xue, J. Zhu, Q. Jiang, S. Wang, L. Peng, Self-retracting motion of graphite microflakes, Physical Review Letters 100 (6) (2008) 067205.

[110] T. W. Ng, C. Y. Lau, E. Bernados-Chamagne, J. Z. Liu, J. Sheridan, N. Tan, Graphite flake self-retraction response based on potential seeking, Nanoscale Resserach Letters 7 (1) (2012) 1–9.

[111] I. V. Lebedeva, A. A. Knizhnik, A. M. Popov, Y. E. Lozovik, B. V. Potapkin, Interlayer interaction and relative vibrations of bilayer graphene, Physical Chemistry Chemical Physics 13 (13) (2011) 5687–5695.

[112] Z. Liu, J. Z. Liu, Y. Cheng, Z. Li, L. Wang, Q. Zheng, Interlayer binding energy of graphite: A mesoscopic determination from deformation, Physical Review B 85 (20) (2012) 205418.

[113] F. Ding, Z. Xu, B. I. Yakobson, Interaction between graphene layers and the mechanisms of graphites superlubricity and self-retraction, Nanoscale 5 (2013) 6736–6741.

[114] A. M. Popov, I. V. Lebedeva, A. A. Knizhnik, Y. E. Lozovik, B. V. Potapkin, Molecular dynamics simulation of the self-retracting motion of a graphene flake, Physical Review B 84 (24) (2011) 245437.

[115] A. M. Popov, I. V. Lebedeva, A. A. Knizhnik, Y. E. Lozovik, B. V. Potapkin, Commensurate-incommensurate phase transition in bilayer graphene, Physical Review B 84 (2011) 045404.

[116] Z. Ye, A. Otero-de-la Roza, E. R. Johnson, A. Martini, The role of roughness-induced damping in the oscillatory motion of bilayer graphene, Nanotechnology 25 (42) (2014) 425703.

[117] R. Decker, Y. Wang, V. W. Brar, W. Regan, H.-Z. Tsai, Q. Wu, W. Gannett, A. Zettl, M. F. Crommie, Local electronic properties of graphene on a bn substrate via scanning tunneling microscopy, Nano Letters 11 (6) (2011) 2291–2295.

[118] Y. Zhang, V. W. Brar, F. Wang, C. Girit, Y. Yayon, M. Panlasigui, A. Zettl, M. F. Crommie, Giant phonon-induced conductance in scanning tunnelling spectroscopy of gate-tunable graphene, Nature Physics 4 (2008) 627–630.

[119] V. Geringer, M. Liebmann, T. Echtermeyer, S. Runte, M. Schmidt, R. Rückamp, M. C. Lemme, M. Morgenstern, Intrinsic and extrinsic corrugation of monolayer graphene deposited on sio_2, Physical Review Letters 102 (7) (2009) 076102.

[120] C. Li, T. Wang, Y. Wu, F. Ma, G. Zhao, X. Hao, Fabrication of two-dimensional nanosheets via water freezing expansion exfoliation, Nanotechnology 25 (49) (2014) 495302.

[121] K. Novoselov, D. Jiang, F. Schedin, T. Booth, V. Khotkevich, S. Morozov, A. Geim, Two-dimensional atomic crystals, Proceedings of the National Academy of Sciences 102 (30) (2005) 10451–10453.

[122] C. Sevik, A. Kinaci, J. B. Haskins, T. Çağın, Characterization of thermal transport in low-dimensional boron nitride nanostructures, Physical Review B 84 (8) (2011) 085409.

[123] T. Liang, S. R. Phillpot, S. B. Sinnott, Parametrization of a reactive many-body potential for mo–s systems, Physical Review B 79 (24) (2009) 245110.

[124] T. Liang, S. R. Phillpot, S. B. Sinnott, Erratum: Parametrization of a reactive many-body potential for mo–s systems [phys. rev. b 79, 245110 (2009)], Physical Review B 85 (19) (2012) 199903.

[125] D. Baowan, J. M. Hill, Nested boron nitride and carbon-boron nitride nanocones, Micro Nano Letters 2 (2) (2007) 46–49.

[126] Z. Ye, A. Otero-de-la Roza, E. R. Johnson, A. Martini, Oscillatory motion in layered materials: graphene, boron nitride, and molybdenum disulfide, Nanotechnology 26 (16) (2015) 165701.

[127] T. Sugino, C. Kimura, T. Yamamoto, Electron field emission from boron-nitride nanofilms, Applied Physics Letters 80 (19) (2002) 3602–3604.

[128] D. Rabson, Toward theories of friction and adhesion on quasicrystals, Progress in Surface Science 87 (2012) 253–271.

[129] J.-M. Dubois, P. Weinland, Matériaux de revêtement pour alliages métalliques et métaux, Organisation Mondiale de la Propriété Intellectuelle brevet no. WO 90/01567, European patent registry number EP0356287 (1990); original French patent application number 8810559 from 1988 (1990).

[130] J. M. Dubois, A. Proner, B. Bucaille, P. Cathonnet, C. Dong, V. Richard, A. Pianelli, Y. Massiani, S. Aityaazza, E. Belinferre, Quasi-crystalline coatings with reduced adhesion for cookware, Annales de Chimie—Science des Matériaux 19 (1994) 3–25.

[131] O. G. Symko, T. Klein, D. Kieda, Formation and applications of AlCuFe quasicrystalline thin films, United-States Patent number 6,294,030 B1 (September 2001).

[132] J.-M. Dubois, New prospects from potential applications of quasicrystalline materials, Materials Science and Engineering: A 294 (2000) 4–9.

[133] J. M. Dubois, So useful, those quasicrystals, Israel Journal of Chemistry 51 (2011) 1168–1175.

[134] J. Y. Park, P. A. Thiel, Atomic scale friction and adhesion properties of quasicrystal surfaces, Journal of Physics: Condensed Matter 20 (2008) 314012.

[135] C. Mancinelli, C. Jenks, P. Thiel, A. Gellman, Tribological properties of a B2-type Al-Pd-Mn quasicrystal approximant, Journal of Materials Research 18 (2003) 1447–1456.

[136] J. Y. Park, P. A. Thiel, Atomic scale friction and adhesion properties of quasicrystal su rfaces, J. Phys.: Cond. Mat. 20 (2008) 314012.

[137] K. Urban, M. Wollgarten, R. Wittmann, Dislocations and plasticity of quasicrystals, Physica Scripta T49 (1993) 360–363.

[138] K. Urban, M. Feuerbacher, M. Wollgarten, M. Bartsch, U. Messerschmidt, Mechanical properties of quasicrystals, in: Z. Stadnik (Ed.), Physical Properties of Quasicrystals, Springer, Berlin, 1999, Ch. 11, pp. 361–401.

[139] L.-M. Zhang, D. J. Sordelet, M. Besser, J.-M. Dubois, Comparative study of microstructural and tribological properties of sintered, bulk icosahedral samples, Materials Science and Engineering 294–296 (2000) 74–78.

[140] J.-M. Dubois, New prospects from potential applications of quasicrystalline materials, Materials Science and Engineering 294–296 (2000) 4–9.

[141] J. Y. Park, D. Ogletree, M. Salmeron, R. Ribeiro, P. Canfield, C. Jenks, P. Thiel, High frictional anisotropy of periodic and aperiodic directions on a quasicrystal surface, Science 309 (5739) (2005) 1354–1356.

[142] A. E. Filippov, A. Vanossi, M. Urbakh, Origin of friction anisotropy on a quasicrystal surface, Physical Review Letters 104 (7) (2010) 074302.

[143] A. E. Filippov, A. Vanossi, M. Urbakh, Erratum: Origin of friction anisotropy on a quasicrystal surface, Physical Review Letters 104 (2010) 149901.

[144] A. E. Filippov, A. Vanossi, M. Urbakh, Filippov, Vanossi, and Urbakh Reply, Physical Review Letters 107 (2011) 209402.

[145] K. McLaughlin, D. Rabson, P. Thiel, Comment on origin of friction anisotropy on a quasicrystal surface, Physical Review Letters 107 (2011) 209401.

[146] R. G. Tobin, Comment on ‘‘surface resistivity and vibrational damping in adsorbed layers’’, Physical Review B 48 (1993) 15468–15470.

[147] J. B. Sokoloff, Theory of the contribution to sliding friction from electronic excitations in the microbalance experiment, Physical Review B 52 (1995) 5318–5322.

[148] J. Krim, C. Daly, A. Dayo, Electronic contributions to sliding friction, Tribology Letters 1 (1995) 211–218.

[149] A. Dayo, W. Alnasrallah, J. Krim, Superconductivity-dependent sliding friction, Physical Review Letters 80 (1998) 1690–1693.

[150] Y. Dong, Q. Li, A. Martini, Molecular dynamics simulation of atomic friction: A review and guide, Journal of Vacuum Science and Technology A 31 (2013) 030801.

[151] R. McGrath, J. A. Smerdon, H. R. Sharma, W. Theis, J. Ledieu, The surface science of quasicrystals, Journal Physics: Condensed Matter 22 (2010) 084022.1–084022.14.

[152] S. W. Kycia, A. I. Goldman, T. A. Lograsso, D. W. Delaney, D. Black, M. Sutton, E. Dufresne, R. Brüning, B. Rodricks, Dynamical x-ray diffraction from an icosahedral quasicrystal, Physical Review B 48 (5) (1993) 3544–3547.

[153] H. Takakura, C. P. Gómez, A. Yamamoto, M. de Boissieu, A.-P. Tsai, Atomic structure of the binary icosahedral Yb-Cd quasicrystal, Nature Materials 6 (2007) 58–63.

[154] C. L. Henley, Cell geometry for cluster-based quasicrystal models, Physical Review B 43 (1) (1991) 993.

[155] M. Widom, private communication.

[156] S. Foiles, M. Baskes, M. Daw, Embedded-atom-method functions for the fcc metals cu, ag, au, ni, pd, pt, and their alloys, Physical Review B 33 (12) (1986) 7983.

[157] G. P. Pun, V. Yamakov, Y. Mishin, Interatomic potential for the ternary ni–al–co system and application to atomistic modeling of the b2–l10 martensitic transformation, Modelling and Simulation in Materials Science and Engineering 23 (6) (2015) 065006.

[158] G. P. P. Pun, Y. Mishin, Development of an interatomic potential for the ni-al system, Philosophical Magazin 89 (2009) 3245.

[159] G. P. P. Pun, Y. Mishin, Embedded-atom potential for hcp and fcc cobalt, Physical Review B 86 (2012) 134116.

[160] J. Y. Park, D. Ogletree, M. Salmeron, R. Ribeiro, P. C. Canfield, C. J. Jenks, P. A. Thiel, Tribological properties of quasicrystals: Effect of aperiodic versus periodic surface order, Physical Review B 74 (2) (2006) 024203.

[161] J. Y. Park, D. Ogletree, M. Salmeron, C. J. Jenks, P. A. Thiel, J. Brenner, J. Dubois, Friction anisotropy: A unique and intrinsic property of decagonal quasicrystals, Journal of Materials Research 23 (05) (2008) 1488–1493.

[162] J. Y. Park, D. Ogletree, M. Salmeron, R. Ribeiro, P. C. Canfield, C. J. Jenks, P. A. Thiel, Elastic and inelastic deformations of ethylene-passivated tenfold decagonal al- ni- co quasicrystal surfaces, Physical Review B 71 (14) (2005) 144203.

[163] J. Park, D. Ogletree, M. Salmeron, C. Jenks, P. Thiel, Friction and adhesion properties of clean and oxidized Al-Ni-Co decagonal quasicrystals: a UHV atomic force microscopy/scanning tunneling microscopy study, Tribology Lett. 17 (2004) 629–636.

[164] J. Y. Park, D. F. Ogletree, M. Salmeron, R. A. Ribeiro, P. C. Canfield, C. J. Jenks, P. A. Thiel, Elastic and inelastic deformations of ethylene-passivated tenfold decagonal Al-Ni-Co quasicrystal surfaces, Physical Review B 71 (2005) 144203.

[165] J. Park, D. Ogletree, M. Salmeron, R. Ribeiro, P. Canfield, C. Jenks, P. Thiel, Adhesion properties of decagonal quasicrystals in ultrahigh vacuum, Philosophical Magazine 86 (6-8) (2006) 945–950.

[166] H. Böttger, G. Kasner, Self-similarity of the density of states of electron and phonon models in fibonacci chains, Physical Status Solidi B 158 (1990) 143–151.

[167] J. Hafner, M. Krajči, M. Mihalkovič, Propagating and localized elementary excitations in decagonal quasicrystals, Physical Review Letters 76 (1996) 2738–2741.

[168] M. A. Chernikov, H. R. Ott, A. Bianchi, T. W. Migliori, A. an d Darling, Elastic moduli of a single quasicrystal of decagonal Al-Ni-Co: Evidence for transverse elastic isotropy, Physical Review Letters 80 (1998) 321–324.

[169] F. Dugain, M. de Boissieu, K. Shibata, R. Currat, T. Sato, A. Kortan, J.-B. Suck, K. Hradil, F. Frey, A. Tsai, Inelastic neutron scattering study of the dynamics of the AlNiCo decagonal phase, The European Physical Journal B 7 (1999) 513–516.

[170] C. Dong, L. Zhang, Q. Zhou, H. Zhang, J. Dubois, Q. Zhang, Y. Fu, F. He, F. Ge, Structure and tribological property of b2-based approximants, Bulletin of Materials Science 22 (1999) 465–472.

[171] P. Egberts, G. H. Han, X. Z. Liu, A. C. Johnson, R. W. Carpick, Frictional behavior of atomically thin sheets: hexagonal-shaped graphene islands grown on copper by chemical vapor deposition, ACS Nano 8 (5) (2014) 5010–5021.

[172] N. N. Gosvami, P. Egberts, R. Bennewitz, Molecular order and disorder in the frictional response of alkanethiol self-assembled monolayers, The Journal of Physical Chemistry A 115 (25) (2011) 6942–6947.

[173] S. Rubinstein, G. Cohen, J. Fineberg, Contact area measurements reveal loading-history dependence of static friction, Physical Review Letters 96 (25) (2006) 256103.

[174] A. Dedinaite, E. Thormann, G. Olanya, P. M. Claesson, B. Nyström, A.-L. Kjøniksen, K. Zhu, Friction in aqueous media tuned by temperature-responsive polymer layers, Soft Matter 6 (11) (2010) 2489–2498.

[175] E. Thormann, Negative friction coefficients, Nature Materials 12 (6) (2013) 468–468.

[176] A. A. Feiler, J. Stiernstedt, K. Theander, P. Jenkins, M. W. Rutland, Effect of capillary condensation on friction force and adhesion, Langmuir 23 (2) (2007) 517–522.

[177] R. Bodvik, E. Thormann, L. Karlson, P. M. Claesson, Temperature responsive surface layers of modified celluloses, Physical Chemistry Chemical Physics 13 (10) (2011) 4260–4268.

[178] K. Wahl, S. Stepnowski, W. Unertl, Viscoelastic effects in nanometer-scale contacts under shear, Tribology Letters 5 (1) (1998) 103–107.

[179] K. Wahl, S. Asif, J. Greenwood, K. Johnson, Oscillating adhesive contacts between micron-scale tips and compliant polymers, Journal of colloid and interface science 296 (1) (2006) 178–188.

[180] P. C. Nalam, N. N. Gosvami, M. A. Caporizzo, R. J. Composto, R. W. Carpick, Nano-rheology of hydrogels using direct drive force modulation atomic force microscopy, Soft Matter 11 (41) (2015) 8165–8178.

[181] J. Tersoff, Empirical interatomic potential for silicon with improved elastic properties, Physical Review B 38 (14) (1988) 9902.

[182] W. L. Jorgensen, J. Chandrasekhar, J. D. Madura, R. W. Impey, M. L. Klein, Comparison of simple potential functions for simulating liquid water, The Journal of Chemical Physics 79 (2) (1983) 926–935.

[183] R. Williams, A. M. Goodman, Wetting of thin layers of sio2 by water, Applied Physics Letters 25 (10) (1974) 531–532.

[184] R. R. Thomas, F. B. Kaufman, J. T. Kirleis, R. A. Belsky, Wettability of polished silicon oxide surfaces, Journal of The Electrochemical Society 143 (2) (1996) 643–648.

[185] F. Taherian, V. Marcon, N. F. van der Vegt, F. Leroy, What is the contact angle of water on graphene?, Langmuir 29 (5) (2013) 1457–1465.

[186] Z. Li, Y. Wang, A. Kozbial, G. Shenoy, F. Zhou, R. McGinley, P. Ireland, B. Morganstein, A. Kunkel, S. P. Surwade, et al., Effect of airborne contaminants on the wettability of supported graphene and graphite, Nature Materials 12 (10) (2013) 925–931.

[187] C.-J. Shih, M. S. Strano, D. Blankschtein, Wetting translucency of graphene, Nature Materials 12 (10) (2013) 866–869.

[188] C.-J. Shih, Q. H. Wang, S. Lin, K.-C. Park, Z. Jin, M. S. Strano, D. Blankschtein, Breakdown in the wetting transparency of graphene, Physical Review Letters 109 (17) (2012) 176101.

[189] G. He, M. H. Müser, M. O. Robbins, Adsorbed layers and the origin of static friction, Science 284 (5420) (1999) 1650–1652.

[190] S. Cheng, B. Luan, M. O. Robbins, Contact and friction of nanoasperities: Effects of adsorbed monolayers, Physical Review E 81 (1) (2010) 016102.

[191] W. H. Briscoe, J. Klein, Friction and adhesion hysteresis between surfactant monolayers in water, The Journal of Adhesion 83 (7) (2007) 705–722.

[192] A. Soper, The radial distribution functions of water and ice from 220 to 673 k and at pressures up to 400 mpa, Chemical Physics 258 (2) (2000) 121–137.

[193] H. B. Eral, D. J. C. M. 't Mannetje, J. M. Oh, Contact angle hysteresis: A review of fundamentals and applications, Colloid and Polymer Science 291 (2) (2013) 247–260.

[194] G. Meyer, N. M. Amer, Simultaneous measurement of lateral and normal forces with an optical-beam-deflection atomic force microscope, Applied Physics letters 57 (1990) 2089.

[195] J. A. Ruan, B. Bhushan, Frictional behavior of highly oriented pyrolytic graphite, Journal of Applied Physics 76 (1994) 8117.

[196] Y. Dong, X. Z. Liu, P. Egbert, Z. Ye, C. R. W., A. Martini, Correlation between probe shape and atomic friction peaks at graphite step edges, Tribology Letters Online First.

[197] R. L. Schwoebel, Step motion on crystal surfaces, Journal of Applied Physics 37 (1966) 3682–3686.

[198] R. L. Schwoebel, Step motion on crystal surfaces ii, Journal of Applied Physics 40 (1969) 614–618.

[199] Q. Li, Y. Dong, D. Perez, A. Martini, R. W. Carpick, Speed Dependence of Atomic Stick-Slip Friction in Optimally Matched Experiments and Molecular Dynamics Simulations, Physical Review Letters 106 (12) (2011) 126101.

[200] S. J. Stuart, A. B. Tutein, J. A. Harrison, A reactive potential for hydrocarbons with intermolecular interactions, The Journal of chemical physics 112 (14) (2000) 6472–6486.

[201] D. G. Teer, New solid lubricant coatings, Wear 251 (2001) 1068–1074.

[202] Z. Ye, A. Otero-de-la Roza, E. R. Johnson, A. Martini, Effect of tip shape on atomic-friction at graphite step edges, Applied Physics Letters 103 (8) (2013) 081601.

[203] D. P. Hunley, T. J. Flynn, T. Dodson, A. Sundararajan, M. J. Boland, D. R. Strachan, Friction, adhesion, and elasticity of graphene edges, Physical Review B 87 (3) (2013) 035417.

[204] Y. Dong, X. Z. Liu, P. Egberts, Z. Ye, R. W. Carpick, A. Martini, Correlation between probe shape and atomic friction peaks at graphite step edges, Tribology Letters 50 (1) (2013) 49–57.

[205] H. Lee, H.-B.-R. Lee, S. Kwon, M. Salmeron, J. Y. Park, Internal and external atomic steps in graphite exhibit dramatically different physical and chemical properties, ACS Nano 9 (4) (2015) 3814–3819.

[206] J. E. Sader, J. W. Chon, P. Mulvaney, Calibration of rectangular atomic force microscope cantilevers, Review of Scientific Instruments 70 (10) (1999) 3967–3969.

[207] C. P. Green, H. Lioe, J. P. Cleveland, R. Proksch, P. Mulvaney, J. E. Sader, Normal and torsional spring constants of atomic force microscope cantilevers, Review of Scientific Instruments 75 (6) (2004) 1988–1996.

[208] E. Meyer, H. J. Hug, R. Bennewitz, Scanning probe microscopy: the lab on a tip, Springer Science & Business Media, 2004.

[209] K. Johnson, K. Kendall, A. Roberts, Surface energy and the contact of elastic solids, in: Proceedings of the Royal Society of London A: Mathematical, Physical and Engineering Sciences, Vol. 324, The Royal Society, 1971, pp. 301–313.

[210] I. Szlufarska, M. Chandross, R. W. Carpick, Recent advances in single-asperity nanotribology, Journal of Physics D: Applied Physics 41 (12) (2008) 123001.

[211] N. N. Gosvami, M. Feldmann, J. Peguiron, M. Moseler, A. Schirmeisen, R. Bennewitz, Ageing of a Microscopic Sliding Gold Contact at Low Temperatures, Physical Review Letters 107 (14) (2011) 144303.

[212] D. R. Baselt, J. D. Baldeschwieler, Lateral forces during atomic force microscopy of graphite in air, Journal of Vacuum Science & Technology B 10 (5) (1992) 2316–2322.

[213] H. Shindo, M. Ohashi, O. Tateishi, A. Seo, Atomic force microscopic observation of step movements on NaCl (001) and NaF (001) with the help of adsorbed water, Journal of the Chemical Society, Faraday Transactions 93 (6) (1997) 1169–1174.

[214] C. Sommerhalter, T. W. Matthes, T. Glatzel, A. Jager-Waldau, M. C. Lux-Steiner, High-sensitivity quantitative Kelvin probe microscopy by noncontact ultra-high-vacuum atomic force microscopy, Applied Physics Letters 75 (2) (1999) 286.

[215] C. Greiner, J. R. Felts, Z. Dai, W. P. King, R. W. Carpick, Local nanoscale heating modulates single-asperity friction., Nano Letters 10 (11) (2010) 4640–4645.

[216] R. H. Savage, Graphite Lubrication, Journal of Applied Physics 19 (1) (1948) 1.

[217] Y. Niimi, T. Matsui, H. Kambara, K. Tagami, M. Tsukada, H. Fukuyama, Scanning tunneling microscopy and spectroscopy of the electronic local density of states of graphite surfaces near monoatomic step edges, Physical Review B 73 (8) (2006) 085421.

[218] W. L. Jorgensen, J. Chandrasekhar, J. D. Madura, R. W. Impey, M. L. Klein, Comparison of simple potential functions for simulating liquid water, The Journal of Chemical Physics 79 (2) (1983) 926.

[219] T. D. B. Jacobs, B. Gotsmann, M. A. Lantz, R. W. Carpick, On the Application of Transition State Theory to Atomic-Scale Wear, Tribology Letters 39 (3) (2010) 257–271.

[220] J. Liu, D. S. Grierson, N. Moldovan, J. Notbohm, S. Li, P. Jaroenapibal, S. D. O'Connor, A. V. Sumant, N. Neelakantan, J. A. Carlisle, K. T. Turner, R. W. Carpick, Preventing nanoscale wear of atomic force microscopy tips through the use of monolithic ultrananocrystalline diamond probes., Small 6 (10) (2010) 1140–1149.

[221] A. Socoliuc, E. Gnecco, S. Maier, O. Pfeiffer, A. Baratoff, R. Bennewitz, E. Meyer, Atomic-scale control of friction by actuation of nanometer-sized contacts, Science 313 (5784) (2006) 207–210.

[222] S. Y. Krylov, J. W. Frenken, The physics of atomic-scale friction: Basic considerations and open questions, Physica Status Solidi (b) 251 (4) (2014) 711–736.

[223] S. Morita, S. Fujisawa, Y. Sugawara, Spatially quantized friction with a lattice periodicity, Surface Science Reports 23 (1) (1996) 1–41.

[224] C. M. Mate, G. M. McClelland, R. Erlandsson, S. Chiang, Atomic-scale friction of a tungsten tip on a graphite surface, in: Scanning Tunneling Microscopy, Springer, 1987, pp. 226–229.

[225] L. Prandtl, Ein gedankenmodell zur kinetischen theorie der festen körper, ZAMM-Journal of Applied Mathematics and Mechanics/Zeitschrift für Angewandte Mathematik und Mechanik 8 (2) (1928) 85–106.

[226] G. Tomlinson, Cvi. a molecular theory of friction, The London, Edinburgh, and Dublin philosophical magazine and journal of science 7 (46) (1929) 905–939.

[227] S. N. Medyanik, W. K. Liu, I.-H. Sung, R. W. Carpick, Predictions and observations of multiple slip modes in atomic-scale friction, Physical Review Letters 97 (13) (2006) 136106.

[228] I. Szlufarska, M. Chandross, R. W. Carpick, Recent advances in single-asperity nanotribology, Journal of Physics D: Applied Physics 41 (12) (2008) 123001.

[229] C. Nogues, M. Wanunu, A rapid approach to reproducible, atomically flat gold films on mica, Surface Science 573 (3) (2004) L383–L389.

[230] E. Meyer, H. J. Hug, R. Bennewitz, Introduction to scanning probe microscopy, in: Scanning Probe Microscopy, Springer, 2004, pp. 1–13.

[231] M. S. Daw, M. I. Baskes, Embedded-atom method: Derivation and application to impurities, surfaces, and other defects in metals, Physical Review B 29 (12) (1984) 6443.

[232] S. Plimpton, Fast parallel algorithms for short-range molecular dynamics, Journal of Computational Physics 117 (1995) 1–19.

[233] E. Riedo, E. Gnecco, R. Bennewitz, E. Meyer, H. Brune, Interaction potential and hopping dynamics governing sliding friction, Physical Review Letters 91 (8) (2003) 084502.

[234] Y. Sang, M. Dubé, M. Grant, Thermal effects on atomic friction, Physical Review Letters 87 (17) (2001) 174301.

[235] A. F. Voter, Parallel replica method for dynamics of infrequent events, Physical Review B 57 (22) (1998) R13985.

[236] B. P. Uberuaga, S. J. Stuart, A. F. Voter, Parallel replica dynamics for driven systems: derivation and application to strained nanotubes, Physical Review B 75 (1) (2007) 014301.

[237] M. Enachescu, R. Van Den Oetelaar, R. Carpick, D. Ogletree, C. Flipse, M. Salmeron, Observation of proportionality between friction and contact area at the nanometer scale, Tribology Letters 7 (2-3) (1999) 73–78.

[238] M. Lantz, S. O'shea, M. Welland, K. Johnson, Atomic-force-microscope study of contact area and friction on nbse 2, Physical Review B 55 (16) (1997) 10776.

[239] D. R. Lide, Crc handbook of physics and chemistry (2001).

[240] A. Labuda, M. Lysy, W. Paul, Y. Miyahara, P. Grütter, R. Bennewitz, M. Sutton, Stochastic noise in atomic force microscopy, Physical Review E 86 (3) (2012) 031104.

[241] Y. Dong, H. Gao, A. Martini, P. Egberts, Reinterpretation of velocity-dependent atomic friction: Influence of the inherent instrumental noise in friction force microscopes, Physical Review E 90 (1) (2014) 012125.

[242] J. L. Hutter, J. Bechhoefer, Calibration of atomic-force microscope tips, Review of Scientific Instruments 64 (7) (1993) 1868–1873.

[243] D. B. Asay, M. T. Dugger, J. A. Ohlhausen, S. H. Kim, Macro-to nanoscale wear prevention via molecular adsorption, Langmuir 24 (1) (2008) 155–159.

[244] D. B. Asay, M. T. Dugger, S. H. Kim, In-situ vapor-phase lubrication of mems, Tribology Letters 29 (1) (2008) 67–74.

[245] M. Mehregany, T.-H. Lee, Silicon carbide nems logic for high-temperature applications, in: SPIE Defense, Security, and Sensing, International Society for Optics and Photonics, 2010, pp. 76791J–76791J.

[246] M. H. Kryder, E. C. Gage, T. W. McDaniel, W. A. Challener, R. E. Rottmayer, G. Ju, Y.-T. Hsia, M. F. Erden, Heat assisted magnetic recording, Proceedings of the IEEE 96 (11) (2008) 1810–1835.

[247] P. C. Fletcher, J. R. Felts, Z. Dai, T. D. Jacobs, H. Zeng, W. Lee, P. E. Sheehan, J. A. Carlisle, R. W. Carpick, W. P. King, Wear-resistant diamond nanoprobe tips with integrated silicon heater for tip-based nanomanufacturing, ACS Nano 4 (6) (2010) 3338–3344.

[248] S. C. Tung, M. L. McMillan, Automotive tribology overview of current advances and challenges for the future, Tribology International 37 (7) (2004) 517–536.

[249] N. Nagel, M. Sanchez-Nagel, F. Zhang, X. Garcia, B. Lee, Coupled numerical evaluations of the geomechanical interactions between a hydraulic fracture stimulation and a natural fracture system in shale formations, Rock Mechanics and Rock Engineering 46 (3) (2013) 581–609.

[250] M. D. Zoback, A. Kohli, I. Das, M. W. Mcclure, et al., The importance of slow slip on faults during hydraulic fracturing stimulation of shale gas reservoirs, in: SPE Americas Unconventional Resources Conference, Society of Petroleum Engineers, 2012.

[251] J. I. Adachi, E. Detournay, Plane strain propagation of a hydraulic fracture in a permeable rock, Engineering Fracture Mechanics 75 (16) (2008) 4666–4694.

[252] K. Jinesh, S. Y. Krylov, H. Valk, M. Dienwiebel, J. Frenken, Thermolubricity in atomic-scale friction, Physical Review B 78 (15) (2008) 155440.

[253] S. Y. Krylov, K. Jinesh, H. Valk, M. Dienwiebel, J. Frenken, Thermally induced suppression of friction at the atomic scale, Physical Review E 71 (6) (2005) 065101.

[254] E. Gnecco, S. Maier, E. Meyer, Superlubricity of dry nanocontacts, Journal of Physics: Condensed Matter 20 (35) (2008) 354004.

[255] J.-W. Jiang, J. Lan, J.-S. Wang, B. Li, Isotopic effects on the thermal conductivity of graphene nanoribbons: Localization mechanism, Journal of Applied Physics 107 (5) (2010) 054314–054314.

[256] L. Britnell, R. V. Gorbachev, R. Jalil, B. D. Belle, F. Schedin, M. I. Katsnelson, L. Eaves, S. V. Morozov, A. S. Mayorov, N. M. Peres, et al., Electron tunneling through ultrathin boron nitride crystalline barriers, Nano Letters 12 (3) (2012) 1707–1710.

[257] A. Perucchi, L. Baldassarre, C. Marini, P. Postorino, F. Bernardini, S. Massidda, S. Lupi, Universal conductivity and the electrodynamics of graphite at high pressures, Phys. Rev. B 86 (3) (2012) 035114.

[258] Y. Zhang, Y.-W. Tan, H. L. Stormer, P. Kim, Experimental observation of the quantum hall effect and berry's phase in graphene, Nature 438 (7065) (2005) 201–204.

[259] G. Li, E. Y. Andrei, Observation of landau levels of dirac fermions in graphite, Nat. Phys. 3 (9) (2007) 623–627.

[260] X. Huang, Z. Yin, S. Wu, X. Qi, Q. He, Q. Zhang, Q. Yan, F. Boey, H. Zhang, Graphene-based materials: Synthesis, characterization, properties, and applications, Small 7 (14) (2011) 1876–1902.

[261] K. P. Loh, Q. Bao, G. Eda, M. Chhowalla, Graphene oxide as a chemically tunable platform for optical applications, Nature Chemistry 2 (12) (2010) 1015–1024.

[262] Y. Zhu, S. Murali, W. Cai, X. Li, J. W. Suk, J. R. Potts, R. S. Ruoff, Graphene and graphene oxide: synthesis, properties, and applications, Advanced Materials 22 (35) (2010) 3906–3924.

[263] J. S. Bunch, A. M. Van Der Zande, S. S. Verbridge, I. W. Frank, D. M. Tanenbaum, J. M. Parpia, H. G. Craighead, P. L. McEuen, Electromechanical resonators from graphene sheets, Science 315 (5811) (2007) 490–493.

[264] G. Jo, M. Choe, S. Lee, W. Park, Y. H. Kahng, T. Lee, The application of graphene as electrodes in electrical and optical devices, Nanotechnology 23 (11) (2012) 112001.

[265] T. S. Mentzel, K. MacLean, M. A. Kastner, Contact-independent measurement of electrical conductance of a thin film with a nanoscale sensor, Nano Letters 11 (10) (2011) 4102–4106.

[266] B. Downey, S. Datta, S. Mohney, Numerical study of reduced contact resistance via nanoscale topography at metal/semiconductor interfaces, Semiconductor Science and Technology 25 (1) (2010) 015010.

[267] F. Xia, V. Perebeinos, Y.-m. Lin, Y. Wu, P. Avouris, The origins and limits of metal-graphene junction resistance, Nature Nanotechnology 6 (3) (2011) 179–184.

[268] K. L. Grosse, M.-H. Bae, F. Lian, E. Pop, W. P. King, Nanoscale joule heating, peltier cooling and current crowding at graphene-metal contacts, Nature Nanotechnology 6 (5) (2011) 287–290.

[269] R. Golizadeh-Mojarad, S. Datta, Effect of contact induced states on minimum conductivity in graphene, Physical Review B 79 (8) (2009) 085410.

[270] P. Blake, R. Yang, S. Morozov, F. Schedin, L. Ponomarenko, A. Zhukov, R. Nair, I. Grigorieva, K. Novoselov, A. Geim, Influence of metal contacts and charge inhomogeneity on transport properties of graphene near the neutrality point, Solid State Communications 149 (27) (2009) 1068–1071.

[271] Y. Matsuda, W.-Q. Deng, W. A. Goddard III, Contact resistance for end-contacted metal- graphene and metal- nanotube interfaces from quantum mechanics, The Journal of Physical Chemistry C 114 (41) (2010) 17845–17850.

[272] Y. Khatami, H. Li, C. Xu, K. Banerjee, Metal-to-multilayer-graphene contact.part i: Contact resistance modeling, Electron Devices, IEEE Transactions on 59 (9) (2012) 2444–2452.

[273] R. A. Serway, J. W. Jewett, Serway's principles of physics: a calculus-based text, Vol. 1, Cengage Learning, 2006.

[274] D. K. Schroder, Semiconductor Material and Device Characterization, Wiley New York, NY, 2006.

[275] C. Uher, L. Sander, Unusual temperature dependence of the resistivity of exfoliated graphites, Physical Review B 27 (2) (1983) 1326.

[276] H. Berger, Contact resistance and contact resistivity, Journal of the Electrochemical Society 119 (4) (1972) 507–514.

[277] J. Greenwood, J. Williamson, Contact of nominally flat surfaces, Proc. R. Soc. A 295 (1442) (1966) 300–319.

[278] B. Luan, M. O. Robbins, Contact of single asperities with varying adhesion: comparing continuum mechanics to atomistic simulations, Physical Review E 74 (2) (2006) 026111.

[279] L. Falkovsky, A. Varlamov, Space-time dispersion of graphene conductivity, The European Physical Journal B 56 (4) (2007) 281–284.

[280] M. Nogi, S. Iwamoto, A. N. Nakagaito, H. Yano, Optically transparent nanofiber paper, Advanced Materials 21 (16) (2009) 1595–1598.

[281] Y. Shimazaki, Y. Miyazaki, Y. Takezawa, M. Nogi, K. Abe, S. Ifuku, H. Yano, Excellent thermal conductivity of transparent cellulose nanofiber/epoxy resin nanocomposites, Biomacromolecules 8 (9) (2007) 2976–2978.

[282] M. Nogi, H. Yano, Transparent nanocomposites based on cellulose produced by bacteria offer potential innovation in the electronics device industry, Advanced Materials 20 (10) (2008) 1849–1852.

[283] L.-F. Chen, Z.-H. Huang, H.-W. Liang, Q.-F. Guan, S.-H. Yu, Bacterial-cellulose-derived carbon nanofiber@ mno2 and nitrogen-doped carbon nanofiber electrode materials: An asymmetric supercapacitor with high energy and power density, Advanced Materials 25 (34) (2013) 4746–4752.

[284] J. Kuczynski, D. Boday, Bio-based materials for high-end electronics applications, International Journal of Sustainable Development & World Ecology 19 (6) (2012) 557–563.

[285] R. J. Moon, A. Martini, J. Nairn, J. Simonsen, J. Youngblood, Cellulose nanomaterials review: structure, properties and nanocomposites, Chemical Society Reviews 40 (7) (2011) 3941–3994.

[286] Y. Zhou, C. Fuentes-Hernandez, T. M. Khan, J.-C. Liu, J. Hsu, J. W. Shim, A. Dindar, J. P. Youngblood, R. J. Moon, B. Kippelen, Recyclable organic solar cells on cellulose nanocrystal substrates, Scientific Reports 3.

[287] Y. Habibi, L. A. Lucia, O. J. Rojas, Cellulose nanocrystals: chemistry, self-assembly, and applications, Chemical Reviews 110 (6) (2010) 3479–3500.

[288] S. Vignolini, P. J. Rudall, A. V. Rowland, A. Reed, E. Moyroud, R. B. Faden, J. J. Baumberg, B. J. Glover, U. Steiner, Pointillist structural color in pollia fruit, Proceedings of the National Academy of Sciences 109 (39) (2012) 15712–15715.

[289] J. Majoinen, E. Kontturi, O. Ikkala, D. G. Gray, Sem imaging of chiral nematic films cast from cellulose nanocrystal suspensions, Cellulose 19 (5) (2012) 1599–1605.

[290] J. A. Diaz, X. Wu, A. Martini, J. P. Youngblood, R. J. Moon, Thermal expansion of self-organized and shear-oriented cellulose nanocrystal films, Biomacromolecules 14 (8) (2013) 2900–2908.

[291] R. Zentel, M. Müiller, H. Keller, Solid opalescent films originating from urethanes of cellulose, Advanced Materials 9 (2) (1997) 159–162.

[292] R. Caruso, J. Schattka, Cellulose acetate templates for porous inorganic network fabrication, Advanced Materials 12 (24) (2000) 1921–1923.

[293] K. E. Shopsowitz, H. Qi, W. Y. Hamad, M. J. MacLachlan, Free-standing mesoporous silica films with tunable chiral nematic structures, Nature 468 (7322) (2010) 422–425.

[294] G. Pernot, M. Stoffel, I. Savic, F. Pezzoli, P. Chen, G. Savelli, A. Jacquot, J. Schumann, U. Denker, I. Mönch, et al., Precise control of thermal conductivity at the nanoscale through individual phonon-scattering barriers, Nature Materials 9 (6) (2010) 491–495.

[295] D. G. Cahill, W. K. Ford, K. E. Goodson, G. D. Mahan, A. Majumdar, H. J. Maris, R. Merlin, S. R. Phillpot, Nanoscale thermal transport, Journal of Applied Physics 93 (2) (2003) 793–818.

[296] Y. Nishiyama, P. Langan, H. Chanzy, Crystal structure and hydrogen-bonding system in cellulose iβ from synchrotron x-ray and neutron fiber diffraction, Journal of the American Chemical Society 124 (31) (2002) 9074–9082.

[297] T. R. Mattsson, J. M. D. Lane, K. R. Cochrane, M. P. Desjarlais, A. P. Thompson, F. Pierce, G. S. Grest, First-principles and classical molecular dynamics simulation of shocked polymers, Physical Review B 81 (5) (2010) 054103.

[298] V. Privalko, V. Novikov, Model treatments of the heat conductivity of heterogeneous polymers, in: Thermal and Electrical Conductivity of Polymer Materials, Springer, 1995, pp. 31–77.

[299] M. Pietralla, High thermal conductivity of polymers: Possibility or dream?, Journal of Computer-Aided Materials Design 3 (1-3) (1996) 273–280.

[300] B. Suleiman, J. Larfeldt, B. Leckner, M. Gustavsson, Thermal conductivity and diffusivity of wood, Wood Science and Technology 33 (6) (1999) 465–473.

[301] C. Choy, Thermal conductivity of polymers, Polymer 18 (10) (1977) 984–1004.

[302] M. Akatsuka, Y. Takezawa, Study of high thermal conductive epoxy resins containing controlled high-order structures, Journal of Applied Polymer Science 89 (9) (2003) 2464–2467.

[303] X. Wu, R. J. Moon, A. Martini, Atomistic simulation of frictional sliding between cellulose iβ nanocrystals, Tribology Letters 52 (3) (2013) 395–405.

[304] S. T. Huxtable, D. G. Cahill, S. Shenogin, L. Xue, R. Ozisik, P. Barone, M. Usrey, M. S. Strano, G. Siddons, M. Shim, et al., Interfacial heat flow in carbon nanotube suspensions, Nature materials 2 (11) (2003) 731–734.

[305] S. Berber, Y.-K. Kwon, D. Tománek, Unusually high thermal conductivity of carbon nanotubes, Physical Review Letters 84 (20) (2000) 4613.

[306] M. Hu, S. Shenogin, P. Keblinski, Molecular dynamics simulation of interfacial thermal conductance between silicon and amorphous polyethylene, Applied Physics Letters 91 (24) (2007) 241910.

[307] M. Hu, P. Keblinski, P. K. Schelling, Kapitza conductance of silicon–amorphous polyethylene interfaces by molecular dynamics simulations, Physical Review B 79 (10) (2009) 104305.

[308] M. D. Losego, L. Moh, K. A. Arpin, D. G. Cahill, P. V. Braun, Interfacial thermal conductance in spun-cast polymer films and polymer brushes, Applied Physics Letters 97 (1) (2010) 011908.

[309] C. McFadden, A. Gellman, Metallic friction: the effect of molecular adsorbates, Surface Science 409 (2) (1998) 171–182.

[310] D. B. Asay, E. Hsiao, S. H. Kim, Effects of adsorbate coverage and capillary on nano-asperity friction in atmosphere containing organic vapor, Journal of Applied Physics 110 (6) (2011) 064326.

[311] C. Greiner, J. R. Felts, Z. Dai, W. P. King, R. W. Carpick, Controlling Nanoscale Friction through the Competition between Capillary Adsorption and Thermally Activated Sliding., ACS Nano 6 (5) (2012) 4305–4313.